## Title

Surface Structures and Surface-Atom Vibrations Determined Using Photoelectron Diffraction



## Author

Wang, L.-Q.

## Publication Date

1991-07-01

LBL-31081

Lawrence Berkeley Laboratory
UNIVERSITY OF CALIFORNIA

Materials & Chemical
Sciences Division

# Surface Structures and Surface-Atom Vibrations Determined Using Photoelectron Diffraction

L.-Q. Wang
(Ph.D. Thesis)

July 1991



Prepared for the U.S. Department of Energy under Contract Number DE-AC03-76SF00098

## DISCLAIMER

LBL-31081

# Surface Structures and Surface-Atom Vibrations Determined Using Photoelectron Diffraction

Li-Qiong Wang
Ph.D. Thesis

Department of Chemistry
University of California at Berkeley

and

Materials and Chemical Sciences Division
Lawrence Berkeley Laboratory
University of California
Berkeley, CA 94720

July 1991

This work was supported by the Director, Office of Energy Research, Office of Basic Energy Sciences, Chemical Sciences Division of the U.S Department of Energy under the Contract No. DE-AC03-76SF00098.

# Contents

# Surface Structures and Surface-Atom Vibrations Determined Using Photoelectron Diffraction

By

Li-Qiong Wang

Abstract

Surface structures of $\sqrt{3}\times\sqrt{3}$ R30° Cl/Ni(111) and c(2×2)Cl/Cu(001) were determined using low-temperature angle-resolved photoemission extended fine structure (ARPEFS), which yields both more accurate surface and near-surface structural information for deeper substrate layers. For the study of c(2×2)Cl/Cu(001), the Cl atoms were found to adsorb in the four-fold hollow site, 1.604(5) Å above the first copper layer, with a Cl-Cu bond length of 2.416(3) Å. The c(2×2)Cl-covered first copper layer showed no relaxation with respect to the bulk position. However, there is a 2% expansion of the separation between the first copper layer and the second atopped-site copper layer, and a small corrugation of the second copper layer where the atopped-site copper atoms are further away from the Cl atom. The distances from the Cl atoms to the third and fourth copper layers were found to be 5.222(25) Å and 7.023(22) Å, respectively, yielding a bulk-like interlayer spacing. Thus the depth sensitivity of low-temperature ARPEFS facilitated definitive referencing of near-surface atomic positions to the underlying lattice. A structural analysis of $\sqrt{3}\times\sqrt{3}$ R30° Cl/Ni(111) determined that the Cl atom adsorbs in the fcc three-fold hollow site, 1.837(8) Å above the first nickel layer, with a Cl-Ni bond

length of 2.332(6) Å, and an approximate 5% contraction between the first and the second nickel layers.

A study of surface-atom vibrations for $\sqrt{3}\times\sqrt{3}$ R30° Cl/Ni(111) and c(2×2)Cl/Cu(001) was made using temperature-dependent ARPEFS. The adsorbate mean-square displacements in the direction parallel to the surface were found to be larger than those perpendicular for both systems. However, the relative magnitude of the vibrational anisotropy in the parallel to the perpendicular directions was found to be larger for the $\sqrt{3}\times\sqrt{3}$ R30° Cl/Ni(111) than for the c(2×2)Cl/Cu(001). A model for predicting the adsorbate vibrational anisotropy from surface structures was proposed and also successfully applied to several adsorbate systems. This model offered a simple and straightforward physical picture for understanding different types of vibrational anisotropy. For example, the c(2×2) overlayers of S and O on Ni(100) have the opposite vibrational anisotropy for S and O atoms.

# Chapter 1

# Introduction

Surface Science studies using well-characterized single crystal surfaces have been exploring surface properties, such as geometric structures, electronic structures, surface chemical bonding and dynamic phenomena, on the molecular level with a combination of electron, ion, photon, and molecular beam scattering techniques. A knowledge of detailed surface structures including adsorption geometries and adsorbate-induced relaxations is essential to any quantitative microscopic understanding of surface phenomena. Angle-resolved photoemission extended fine structure (ARPEFS)[1-5] is well known as one of the techniques which provide the most quantitative surface structural information. This thesis focuses on using the ARPEFS technique with the temperature dependence to determine accurate structural information and dynamic information such as surface-atom vibrations. To demonstrate these capabilities of ARPEFS, two adsorbate systems, c(2×2)Cl/Cu(001) and $\sqrt{3}\times\sqrt{3}$ R30° Cl/Ni(111) were studied using temperature-dependent ARPEFS. We hope to contribute to the understanding of the mechanism of the adsorbate-induced relaxations, the anisotropic surface-atom vibrations, and the relation between the static structural information and dynamic information.

Section 1.1 reviews several techniques based on electron diffraction, and compares them with ARPEFS. Section 1.2 gives a brief introduction to temperature-dependent ARPEFS for obtaining accurate surface and near surface structures, as well as the vibrational amplitudes of surface-atoms.

## 1.1 Electron/Photoelectron Diffraction

Electron diffraction is the interference of electron waves. In Quantum Mechanics, the "two-slits problem" is an example of the interference phenomenon.[6] Electrons in the energy range of 100 - 1000 eV can be used to probe surface structures, due to their limited mean-free-paths caused by inelastic scattering. For example, in low-energy electron-diffraction (LEED), a primary low-energy electron beam hits on a long-range ordered surface, then the reflected electrons are collected. The observed LEED pattern provides direct information on the periodicity or translational symmetry of a surface structure. However, it does not give a clear picture of the actual location of the surface atoms within the unit mesh. To extract this information, the diffracted beam intensities must be studied in a way similar to x-ray crystallography of bulk structures, with a complicated LEED theory.[7]

As with electron diffraction, photoelectron diffraction is the final-state interference of photoelectron waves or Auger electron waves. Based on photoelectron diffraction, techniques such as x-ray photoelectron diffraction (XPD),[8] surface extended x-ray-absorption fine structure (SEXAFS), [9] and ARPEFS [1] have been used to study surface structures.

The first observation of strong diffraction effects in photoemission from single-crystal substrates was made by Siegbahn et al.[10] and by Fadley and Bergstrom.[11] Using

the phenomenon of photoelectron diffraction as a probe of surface structure was originally proposed by Liebsch.[12,13] He suggested that photoelectron diffraction could be observed from adsorbates on surfaces and that the interference pattern could contain information about the geometry of atoms surrounding the photoemitting adsorbate. This theoretical prediction was later confirmed experimentally by Kono et al.,[14] Woodruff et al.,[15] and Kevan et al.[16] independently. Their experiments involved exciting a core photoelectron or a relatively simple "core-like" Auger transition from an adsorbate on a single crystal, and then observing modulations in the resulting photoemission intensities that are due to the final-state interferences between the direct and the scattered waves by neighboring atoms. The peak intensities can be monitored as a function of either the emission directions or the photoelectron kinetic energy. In theory, a complete picture of photoelectron diffraction could be obtained by measuring photoemission intensities as a function of the two-dimensional emission angle and the one-dimensional photoelectron energy, giving a three-dimensional abscissa. However, experimental limitations constrain the measurement to smaller dimensions. Thus, there are several forms of photoelectron diffraction: scanned-angle, scanned-energy, and scanned two-angle photoelectron diffraction. With soft x-ray excitation at about 1.2-1.5 keV in the typical x-ray photoelectron spectroscopy (XPS) limit, scanned-angle measurements have been termed x-ray photoelectron diffraction (XPD) and its close relative Auger electron diffraction (AED), both including the azimuthal- photoelectron diffraction (APD) and the polar- photoelectron diffraction (PPD). In comparison with XPD, scanned-energy photoelectron measurements require a tunable photon source - synchrotron radiation, and consist of performing a series of constant-initial-state scans for a core level, with the electron emission direction held fixed. Originally, this scanned-energy method was called normal photoelectron diffraction (NPD),[17,18] in which oscillations over a limited low energy range were fitted with a

LEED-like theory to derive structures. Later, ARPEFS was employed to emphasize the similarity to surface extended x-ray-absorption fine structure (SEXAFS) and the advantages of non-normal emission directions. More recently, a photoelectron hologram proposed by Barton[19] is a scanned two-angle photoelectron diffraction pattern. A complete three- dimensional image of the surface structure surrounding the emitter can be reconstructed by Fourier transformation. Photoelectron holography is a new way to use photoelectron diffraction to study the structure of solid surfaces: complete three-dimensional images of adsorption sites are now within reach. It promises to be a powerful tool complementary to atomic resolution microscopy - scanning tunneling microscopy (STM).

We will here emphasize the ARPEFS technique and compare it with LEED, XPD, and SEXAFS. ARPEFS is a particular form of angle-resolved and energy-dependent photoelectron diffraction. Figure 1 illustrates the important aspects of the scattering leading to ARPEFS. The incident polarized photon from monochromatized synchrotron radiation excites an adsorbate 1s core-level. The outgoing photoelectron waves can directly propagate to the angular resolving detector, and at the same time, part of them can also be elastically scattered by the surrounding substrate atoms, then propagate to the detector. The direct and scattered waves interfere at the detector constructively or destructively depending on their path-length differences. This interference gives rise to the ARPEFS and can be represented by an oscillatory function $\chi(k)$, as a function of electron wave number k. Using a single-scattering model, $\chi(k)$ can be described as:

$$\chi(k) \propto \sum_j A_j(k) \cos[k\, r_j\, (1-\cos\theta_j) + \phi_j] \,, \qquad (1)$$

where the summation is over all atoms near the adsorbate (source) atom from which the core-level photoemission is being measured, $A_j(k)$ contains the elastic scattering amplitude

modified by the inelastic losses and aperture integration, $r_j$ is the distance between the photoemitter and j th scattering atom , $\theta_j$ is the scattering angle at the j th atom, and $\phi_j$ is the scattering phase shift. The oscillatory nature of $\chi(k)$ allows Fourier transform, giving rather direct access to the structural information. In Fourier transformation, ARPEFS yields path-length differences $\Delta R_j = r_j (1-\cos\theta_j)$, while SEXAFS gives interatomic distances between the adsorbate (source) and substrate (scattering) atoms.

Experimentally, in ARPEFS, one measures the angle-resolved photoemission intensity I(E) as a function of the photoelectron kinetic energy E over a wide energy range (typically ≈ 50 - 550 eV), with equal increments $\Delta k \approx 0.05$ - 0.1 $Å^{-1}$. In analogy to EXAFS, the total photoemission intensity I(E) consists of a slowly varying atomic-like function and an oscillating contribution caused by the interference effects. The oscillating function $\chi(E)$ can be determined by removing the slowly varying atomic-like function $I_0(E)$ from the total photoemission intensity I(E):

$$\chi(E) = \frac{I(E) - I_0(E)}{I_0(E)} \quad . \qquad (2)$$

Thus, $\chi(k)$ curves can be obtained from $\chi(E)$ by converting E to k, using the De Broglie relation:

$$k = \hbar^{-1} \sqrt{2m_e (E + V_0)} \quad , \qquad (3)$$

where $m_e$ is the electron rest mass and $V_0$ is the inner potential of the solid.

A general scheme for ARPEFS date analysis is shown in Fig. 2. Experimental $\chi(k)$ curves are normally analyzed in two ways: fast Fourier-transform (FFT) analysis, and multiple-scattering spherical-wave (MSSW) analysis. We first Fourier-transform the experimental $\chi(k)$ curves, obtaining the qualitative structure information: the adsorption-site identification and approximate geometrical parameters. Based on the qualitative structural information from the Fourier-transform, MSSW calculations are then applied to

simulate the experimental $\chi(k)$ curves using an R-factor (reliability-factor) as a quantitative measure of the fits. With a MSSW level analysis, more precise structural information including small corrugations and relaxations on and near the surface can be obtained. A quantitative structural analysis by ARPEFS requires multiple-scattering spherical-wave theory,[1] while single-scattering is usually applied in SEXAFS and XPD. However, ARPEFS theory is simpler than the LEED theory because in LEED, the incident electron beam excites every atom in the surface region (no chemical specificity), leading to a complex scattering problem. Furthermore, in ARPEFS, the Taylor-series magnetic-quantum-number expansion (TS-MQNE) approximation permits economical MSSW calculations. From Fig. 2, we can see that there is a long journey from MSSW theoretical simulations to the quantitative results because this process involves many detailed data analysis procedures and raises some interesting questions such as how we optimize a large parameter space and what the error is associated with each derived parameter. The answers to these questions will be given in the following chapters. Accurately determining the error associated with each derived parameter is as important as obtaining the parameter itself. Chapter 2 describes detailed procedures for a semi-quantitative estimation of statistical errors instead of quoting all errors as ca. $\pm$ .02 Å, in hopes of advancing a quantitative way of estimating errors.

ARPEFS has large oscillation amplitudes compared with SEXAFS. Since SEXAFS oscillation occurs in the total x-ray absorption cross section, they are an integral of the ARPEFS oscillations over all emission angles[20] and all final states excited at a particular x-ray energy.[21] It is not surprising that this integration averages over various phases and leads to considerably lower percent effect. Therefore, ARPEFS $\chi(k)$ curves with larger oscillating amplitudes can be used to extract the structural information more accurately. Additionally, because of the directional sensitivity of ARPEFS, the different

views of surface structure can be obtained by choosing different emission directions, giving different emphasis to the scattering atoms. Since, in ARPEFS, backward-scattering ($\theta_j = 180^o$) and forward-scattering ($\theta_j = 0^o$) are dominate processes, the emission direction is always chosen to highlight nearby backscattering atoms. Taking advantage of the directional sensitivity of ARPEFS, the normal emission is selected to highlight the perpendicular interlayer spacing, while an offnormal emission direction is chosen to determine the bond length and bond angle. Thus, ARPEFS can determine the deeper interlayer spacings than does SEXAFS. Similarly, XPD or AED has a predominant forward-scattering, giving enhanced peak intensities along major crystal axes. Hence, the "forward scattering" or "search light" effect was applied to epitaxial growth.[22-24]

Photoelectron diffraction is only sensitive to the local environment of a particular species of atom, while LEED needs a long-range ordered system. However, a newly developed technique, diffuse LEED (DLEED) can be used to study disordered surfaces by analyzing the background of the normal LEED intensity.[25, 26] This will make a great contribution for studying imperfect systems such as stepped-surfaces. In principle, ARPEFS could also be used to study disordered systems if there were enough photoemission intensities from the adsorbate atoms.

Since the photoemission final-state interference takes place on the adsorbate (source) atom in SEXAFS, rather than on the detector in ARPEFS, SEXAFS is sensitive to the central (source) atom phase shift. Errors might be brought into the SEXAFS analysis because of uncertainties associated with accurately describing the central atom phase shift.

In summary, each of the techniques we have discused has certain unique advantages and disadvantages, and they often complement one another. In general, ARPEFS is the more precise technique for analyzing detailed structures such as small

relaxations or reconstructions on and near surfaces than SEXAFS, and simpler than LEED in theoretical modelling, but more complicated in experimental details. In this thesis, we use the advantages of ARPEFS. A scientific approach using multiple techniques is required to understand more complicated real systems.

## 1.2 Temperature-Dependent ARPEFS

Atoms are not static in the crystal lattice, but oscillate around their equilibrium positions. This thermally excited vibrational motion of atoms is greatly dependent on the temperature. ARPEFS observes the thermal averaging of the interference effects, where the vibrational motions of surface-atoms attenuate the oscillation amplitude of the $\chi(k)$ function. Thus, $\chi(k)$ is also a function of temperature T. To include the temperature effect, each term of the $\chi(k)$ function given in Eq. (1) must be multiplied by a vibrational attenuation factor. Here we use a temperature-dependent Debye-Waller factor, D(T), which can be simply represented as:

$$D(T) = \exp\ [- \sigma_j^2(T) ( 1 - \cos\theta_j ) k^2], \qquad (4)$$

where $\sigma_j^2(T)$ is the temperature-dependent mean-square relative displacement (MSRD) between the photoemitter and the j th scattering atom, projected on the photoelectron momentum change direction K. Thus,

$$\sigma_j^2(T) = < [ ( u_o - u_j )\cdot K]^2 > , \qquad (5)$$

where $u_o$ and $u_j$ are the displacements of the photoemitter o and the j th scattering atom from their equilibrium positions. We can expand the MSRD, $\sigma_j^2(T)$ into the sum of the mean-square displacements (MSD) of atoms o and j projected on K, minus twice their displacement correlation function (DCF):

$$< [ ( u_o - u_j ) \cdot K]^2 > = < ( u_o \cdot K ) ^2 > + < ( u_j \cdot K ) ^2 > - 2 [ < ( u_o \cdot K ) ( u_j \cdot K) > ] , \quad (6)$$

where each term can be calculated mainly from the individual atomic mass ($m_j$), the anisotropic and surface-layer dependent Debye temperature ($\theta_D$) and the experimental temperature(T).[1] Hence, surface-atom vibrations, described by the mean-square displacement ( MSD ) of the individual atom, depends on the above factors. Softer substrate surface ( lower $\theta_D$ ), higher temperature, and smaller atomic adsorbate mass give the larger attenuation of ARPEFS oscillating amplitudes. In this thesis, we greatly emphasize the temperature effect of ARPEFS. The low-temperature ARPEFS improves the signal-to-noise ratio of $\chi(k,T)$ curves for the softer surfaces and the temperature-dependent ARPEFS allows us to study surface-atom vibrations.

Since all structural information is included in $\chi(k,T)$ curves, $\chi(k,T)$ curves with good quality are required for extracting accurate and detailed surface structures, including surface reconstructions or relaxations. Therefore, it is important to reduce the thermal vibrations of surface atoms to improve the signal-to-noise ratio of $\chi(k,T)$. By choosing the stiff substrate chromium (bulk $\theta_D \approx 460$ K), the large oscillation amplitude ~ 50-70 % was observed in a previous study of S/Cr(001),[3] where path-length differences greater than 10 Å were discernable and successfully modelled by the MSSW calculations. By performing ARPEFS measurements at low temperatures, similar advantages would be expected with a softer lattice. Figure 3 illustrates the temperature effect of ARPEFS. Because copper (bulk $\theta_D \approx 343$ K) is a relatively soft surface, a room-temperature $\chi(E)$ curve has lower oscillation amplitude and bad signal-to noise ratio, especially at higher E, while the low temperature data shows drastically enhanced oscillation amplitudes, and a good signal-to noise ratio even at high E. Furthermore, the Fourier spectra also shown in

this figure clearly demonstrate the value of low-temperature ARPEFS for probing deeper substrate layers.

Adsorbate atoms cause restructuring of single-crystal surfaces, ranging from small atomic relaxations and reconstructions to macroscopic shape modifications. It is important to understand the mechanism of relaxations or reconstructions. However, a complete knowledge of adsorbate-induced relaxations requires a reliable and accurate determination of both surface and near-surface structures including deeper substrate layers. Chapter 2 presents a low-temperature study of the c(2×2)Cl/Cu(001) system, providing a complete picture of surface relaxations. Cooling the lattice effectively extends the range of ARPEFS to the fourth copper layer, thereby firmly referencing atomic positions on and near surface layers to the bulk crystal lattice. We chose the atomic adsorbate systems in our studies because the chances of understanding relaxation phenomena and dynamic information on this type of system are significantly higher. Furthermore, thorough studies on these relatively simple systems will certainly help us to understand more complicated systems, such as catalytic reaction, polymer coating, and other interfacial problems. The interesting questions are : Can a universal picture be proposed to explain the relaxation phenomena for all the systems? Do other Cl adsorbate systems have similar relaxations as does the c(2×2)Cl/Cu(001) system? Chapter 3 presents a low-temperature study of the $\sqrt{3}\times\sqrt{3}$ R30° Cl/Ni(111) system for further exploring the relaxation phenomena.

During recent years, there have been remarkable advances in our understanding of lattice vibrations on both clean and adsorbate-covered surfaces. Techniques such as optical spectroscopies (infrared adsorption[27] and Raman scattering), electron energy loss spectroscopy (EELS),[28] and inelastic scattering of low energy atom beams from the surface such as He-atom scattering[29] are powerful means of probing the vibrational motions of atoms or molecules on surfaces through the dispersion relations of surface

phonons and surface resonances. In EELS, an electron incident on the crystal with energy $E_i$ may excite a quantized vibrational mode with energy $h\omega$ before backscattering into the vacuum. It thus emerges with energy $E_s = E_i - h\omega$, so an analysis of energy spectrum of the backscattered electrons provides direct information on the vibrational frequencies of surface atoms. Instead of electron beams, He scattering uses low-energy He-atom beams. The basic principle of He scattering is very similar to that of EELS. However, in He scattering, time- of-flight spectroscopy and sophisticated detection schemes are required. In general, the resolution offered by optical spectroscopy is superior to EELS. However, when optical methods are applied to the study of adsorbates on surface, the signals are weak and sometimes difficult to detect against the background. Therefore, EELS and He scattering are the most useful tools for surface studies. However, there are some drawbacks to these techniques. In EELS, it is sometimes difficult to detect very low vibrational frequencies for systems. For example, it is for heavy atomic adsorbates on heavy metal surfaces, due to the limited resolution of electron spectrometer. Furthermore, the analysis of phonon spectra can be very complicated if there is an overlapping between bulk and surface phonons. The vibrational spectroscopies we have discused may also be used to infer the nature of an entity adsorbed on the surface and the adsorption site from qualitative features in the spectrum. In comparison with vibrational spectroscopy, electron diffraction is a more powerful tool for obtaining quantitative structural information, but less direct about lattice vibrations. However, from recent temperature-dependent SEXAFS experiments[30,31] we conclude that photoelectron diffraction can be used to study surface-atom vibrations through the mean-square relative displacements inferred from the Debye-Waller factors. Different kinds of anisotropic surface-atom vibrations were observed in these studies. Since ARPEFS has directional sensitivity, the vibrational anisotropy may be more prominent as compared with SEXAFS. In SEXAFS, the anisotropy of surface-atom

vibrational amplitudes is directly obtained from experimental data by comparing the differences of MSRD values at two different temperatures in parallel and perpendicular to the surface. However , because of multiple scattering involved in ARPEFS, it is difficult for ARPEFS to get this information by using a SEXAFS-like method. Therefore, a different approach must be taken to study surface-atom vibrations in ARPEFS analysis. Chapter 4 presents the results of surface-atom vibrational amplitudes and anisotropic vibrations using temperature-dependent ARPEFS studies. Although photoelectron diffraction is more sensitive to the structures than vibrations of surface-atoms, it is a valid approach for obtaining the direct information about surface atom vibrational amplitudes, rather than analyzing complicated phonon spectra in vibrational spectroscopy. Photoelectron diffraction provides information on certain averages over the phonon spectrum of the crystal, and thus is not sensitive to its detailed nature.

Surface properties such as geometric structures, electronic structures, and dynamic phenomena are often related to each other. In surface science, it is important to know the relation between the static structures and the surface dynamics. The conventional view for clean surfaces is that perpendicular surface-atom vibrational amplitudes should be larger because of the increased degrees of freedom at the surface. A study on the c(2×2)O/Ni(001) system[32] showed the similar trend, while a recent SEXAFS study on the c(2×2)Cl/Cu(001) system[30] showed the opposite trend where surface-atom vibrational motions within the plane are larger than those along the normal to the plane. More interestingly, it was found that the adsorbate vibrates nearly isotropically on the surface in the p(2×2)S/Cu(001) system.[5] An interesting question is: Can a universal model be proposed to predict the direction of anisotropic surface-atom vibrations from static surface structural information? Chapter 4 presents a model to predict the anisotropic direction from the structures and to link the structural and dynamic information. This model is

tested by using structural results from the temperature-dependent measurements of both the c(2×2)Cl/Cu(001) and $\sqrt{3}\times\sqrt{3}$ R30° Cl/Ni(111) systems. The remainder of this thesis is organized as follows. Chapters 2 and 3 present detailed studies of adsorbate geometry and substrate surface relaxations using low temperature ARPEFS for the c(2×2)Cl/Cu(001) and $\sqrt{3}\times\sqrt{3}$ R30° Cl/Ni(111) systems, respectively. Chapter 2 also describes the procedures of semi-quantitative error analysis. Chapter 4 presents the results of surface-atom vibrations using temperature-dependent ARPEFS studies on the above systems and predicts the direction of surface -atom vibrational anisotropy. A summary and conclusions are given in chapter 5.

# References


1. J.J. Barton, S.W. Robey, and D.A. Shirley, *Phys. Rev.* **B 34**, 778 (1986).
2. S.W. Robey, J.J. Barton, C.C. Bahr, G. Liu and D.A. Shirley, *Phys.Rev.* **B 35**, 1108 (1987).
3. L.J. Terminnello, X.S. Zhang, S. Kim, A.E. Schach van Wittenau, K.T. Leung and D.A. Shirley, *Phys. Rev.* **B 38**, 3879 (1988).
4. L.Q. Wang, A.E. Schach von Wittenau, Z.G. Ji, L.S. Wang, Z.Q. Huang, and D.A. Shirley, Submitted to *Phys. Rev.* **B**, Dec.,1990
5. A.E. Schach, L.Q. Wang, Z.Q. Huang, Z.G. Ji, and D.A. Shirley, in preparation.
6. R.P. Feynman, R.B. Leightan and M. Sands, Lectures On Physics (Addison-Wesley, London, 1966), Volume III.
7. J.B. Pendry, Low Energy Electron Diffraction (Academic, London, 1974).
8. C.S. Fadley, Prog. in *Surf. Sci.* **16**, 275 (1984).
9. S. Brennan, J. Stohr, and R. Jaeger, *Phys. Rev.* **B 24**, 4871 (1981).
10. K. Siegbahn, U. Gelius, H. Siegbahn and E. Olsen, *Phys. Lett.* **32 A**, 221 (1970).
11. C.S. Fadley and S.A.L. Bergstrom, *Phys. Lett.* **35 A**, 375 (1971).
12. A. Liebsch, *Phys. Rev. Lett.* **32**, 1203 (1974).
13. A. Liebsch, *Phys. Rev.* **B 13**, 544 (1976).
14. S. Kono, C.S. Fadley, N.F.T. Hall and Z. Hussain, *Phys. Rev. Lett.* **41**, 117 (1978).
15. D.P. Woodruff, D. Norman, B.W. Holland, N.V. Smith, H.H. Farrell and M.M Traum, *Phys. Rev. Lett.* **41**, 1130 (1978).
16. S.D. Kevan, D.H. Rosenblatt, D.R. Denley, B.-C. Lu and D.A. Shirley, *Phys. Rev. Lett.* **41**, 1505 (1978).

17. S.D. Kevan, D.H. Rosenblatt, D.R. Denley, B.-C. Lu and D.A. Shirley, *Phys. Rev.* **B 20**, 4133 (1979).

18. D. H. Rosenblatt, J.G. Tobin, M.G. Mason, R.F. Davis, S.D. Kevan, D.A. Shirley, C.H. Li and S.Y. Tong, *Phys. Rev.* **B 23**, 3828 (1981).

19. J.J Barton, *Phys. Rev. Lett.* **61**, 1356 (1988).

20. P.A. Lee, *Phys. Rev.* **B 13**, 5261 (1976).

21. J.J Rehr, E.A. Stern, R.L. Martin, and E.R. Davidson, *Phys. Rev.* **B 17**, 560 (1978).

22. W.F. Egelhoff, *Phys. Rev.* **B 30**, 1052 (1984).

23. E.L. Bullock and C.S. Fadley, *Phys. Rev.* **B 31**, 1212 (1985).

24. C.M. Wei, T.C. Zhao, and S.Y. Tong, *Phys. Rev. Lett.* **65**, 2278 (1990).

25. J.B. Pendry and D.K. Saldin, *Surf. Sci.* **33**, 145 (1984).

26. U. Starke, P.L. de Andres, D.K. Saldin, K. Heinz and J.B. Pendry, *Phys. Rev.* **B 38**, 12277 (1988).

27. R.B. Bailey, and P.L. Richards, *Surf. Sci.* **100**, 8626 (1980).

28. H. Ibach, and D.A. Mills, Electron Energy Loss Spectroscopy (Academic Press, London, 1982).

29. G. Brusdeylins, R.B. Doak, and J.P. Toennis, *Phys. Rev. Lett.* **44**, 1417 (1980).

30. F. Sette, C.T. Chen, J.E. Rowe, and P.H. Citrin, *Phys. Rev. Lett.* **59**, 311 (1987).

31. P. Roubin, D. Chandesris, G. Rossi, J. Lecante, M.C. Desjonqueres, and G. Treglia, *Phys. Rev. Lett.* **56**, 1272 (1986).

32. L. Yang, T.S. Rahman, and D.L. Mills, *Phys. Rev.* **B 42**, 2864 (1990).

# Figure Captions

FIG. 1. An illustration of the basic principle of ARPEFS. ARPEFS is the final-state interference between the direct wave and the scattered wave at the angle-resolving detector. The adsorbate and the substrate atoms are represented by A and B, respectively. The interatomic distance $r_j$, scattering angle $\theta_j$, and photon polarization vector $\varepsilon$ are indicated. The highlighted vectors represent the path-length difference: $r_j (1-\cos\theta_j)$.

FIG. 2. A general scheme for ARPEFS data analysis. The experimental raw data $\chi(E)$ can be analyzed by fast Fourier transform (FFT) to get qualitative results, and also can be simulated by multiple-scattering spherical wave (MSSW) calculations to obtain quantitative results.

FIG. 3. The experimental $\chi(E)$ curves and the Fourier spectra for the [001] geometry at two temperatures, 110 K and 300 K. In the upper portion, the solid curve is $\chi(E)$ at 110 K, while the curve with solid dots is at 300 K. In the lower portion, the heavier curve is the Fourier spectrum at 110 K, while the light one is at 300 K. Each numbered peak is associated with a scattering path-length difference for a numbered atom in the inset.

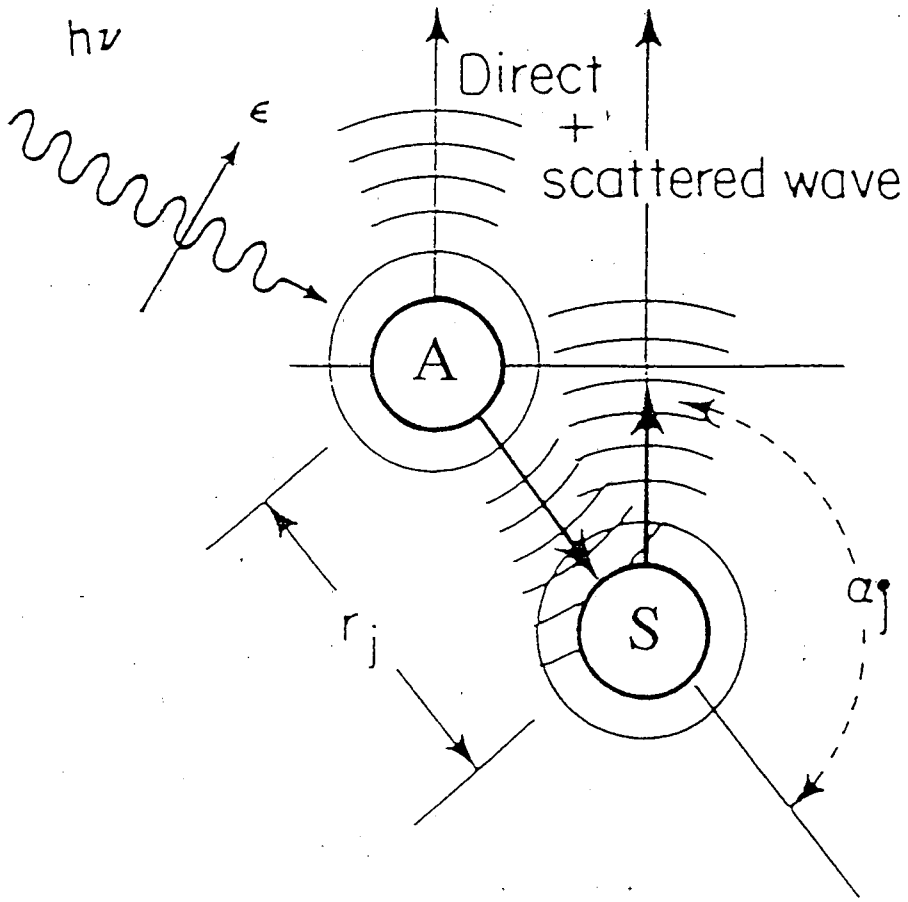


Figure 1

# ARPEFS Data Analysis Scheme

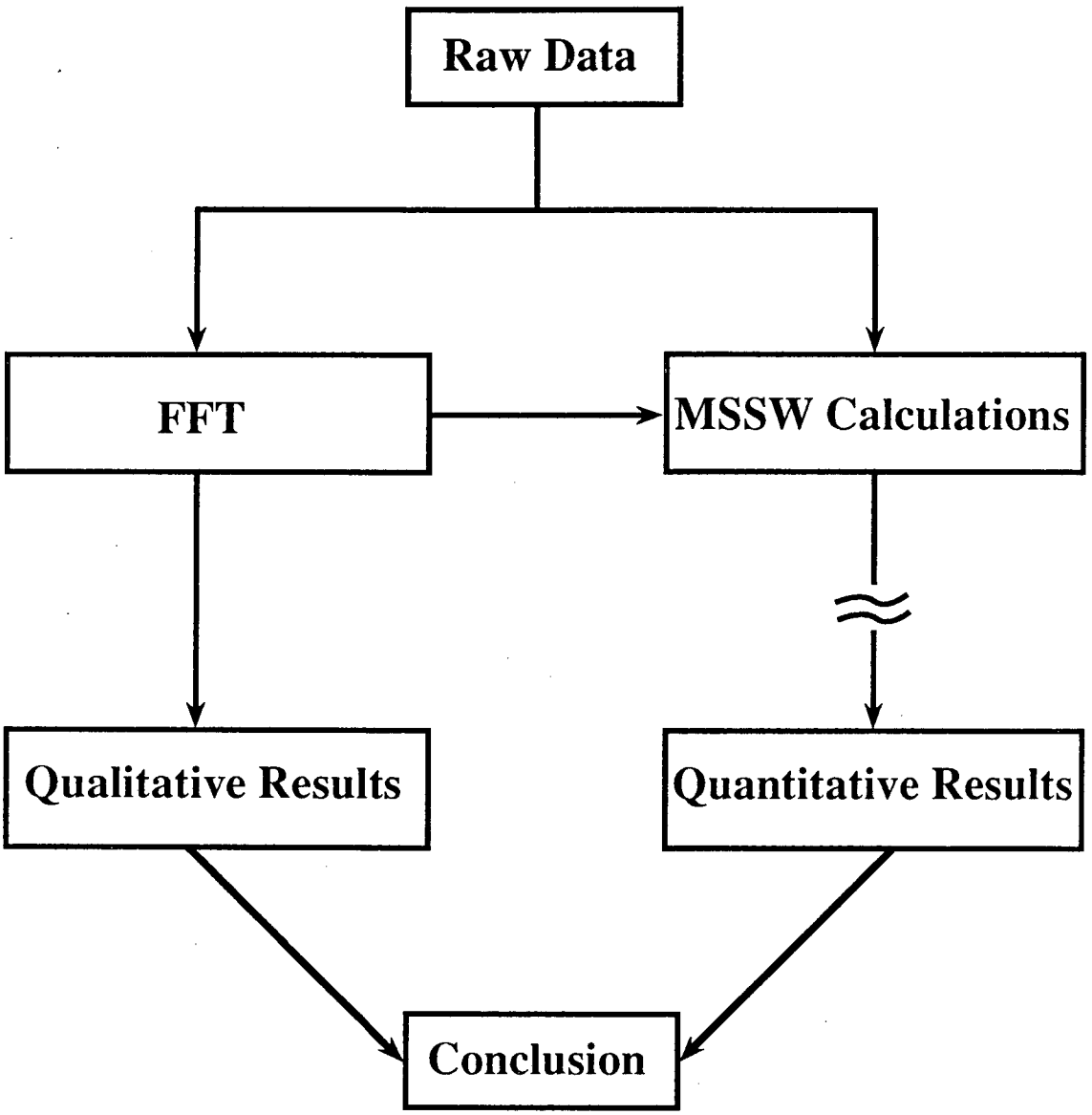


Figure 2

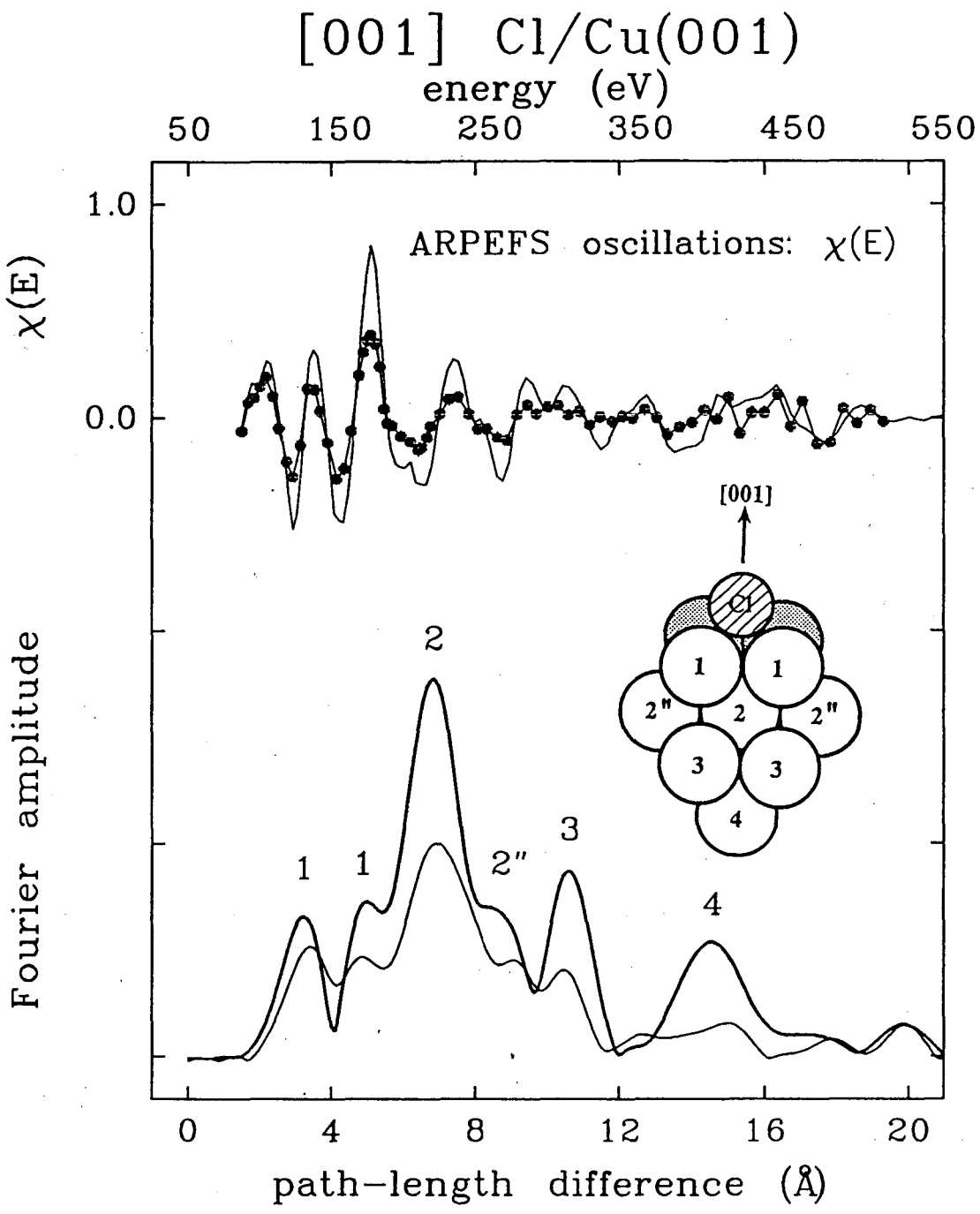
[001] Cl/Cu(001)
energy (eV)
50
150
250
350
450
550
1.0
0.0
χ(E)
ARPEFS oscillations: χ(E)
[001]
Cl
1
1
2"
2
2"
3
3
4
Fourier amplitude
2
1
1
2"
3
4
0
4
8
12
16
20
path−length difference (Å)

Figure 3

# Chapter 2

# Adsorbate Geometry and Substrate-Surface Relaxation of c(2×2)Cl/Cu(001) Using Low-Temperature ARPEFS

## Abstract

A detailed structural study of the c(2×2)Cl/Cu(001) adsorbate system was made, using the angle-resolved photoemission extended fine structure (ARPEFS) technique at low temperature, which yields both more accurate surface structural information and near-surface structural information for deeper substrate layers. Electrons were detected along two emission directions, [001] and [011], and at two temperatures, 110 K and 300 K. The Cl atoms were found to adsorb in the four-fold hollow site, 1.604(5) Å above the first copper layer, with a Cl-Cu bond length of 2.416(3) Å (in which the errors in parentheses are statistical standard deviations only). These values are in excellent agreement with a previous low-energy electron-diffraction study by Jona et al. The c(2×2)Cl-covered first copper layer showed no relaxation with respect to the bulk position. However, a small

corrugation of the second copper layer was found: The second-layer copper atoms below Cl atoms move 0.042(12) Å away from the surface, while those in open positions remain in their bulk positions. The distances from the Cl atoms to the third and fourth copper layers were found to be 5.222(25) Å and 7.023(22) Å, respectively, yielding a bulk-like interlayer spacing. Thus the depth sensitivity of low-temperature ARPEFS facilitated definitive referencing of near-surface atomic positions to the underlying lattice.

## 2.1 Introduction

There is chemical and physical interest in detailed surface structures, and in adsorbate-induced substrate surface relaxation. Techniques such as low-energy electron-diffraction (LEED),[1] surface extended x-ray-absorption fine structure (SEXAFS),[2] medium-energy ion scattering (MEIS),[3] the x-ray standing-wave method,[4] and angle-resolved photoemission extended fine structure (ARPEFS)[5] have been used to study surface structures. However, complete knowledge of adsorbate-induced substrate surface relaxation requires a reliable and accurate determination of both the surface and the near-surface structure, including the deeper substrate layers. ARPEFS may prove to be uniquely suitable in this regard among surface-structural techniques, because of its depth sensitivity to ca. 4-5 atomic layers. The main contribution of this chapter is to demonstrate this capability of ARPEFS by example: we determine the adsorbate geometry and the substrate surface relaxation of c(2×2)Cl/Cu(001) using low-temperature ARPEFS. The key point is that cooling the lattice effectively extends the range of ARPEFS to the fourth copper layer, thereby firmly referencing atomic positions in the surface and near surface layers to the bulk crystal lattice.

ARPEFS is a novel technique for studying surface structures using photoelectron diffraction.[6] Using the phenomenon of photoelectron diffraction as a probe of surface structure was originally proposed by Liebsch[7,8] and was observed experimentally by three groups independently.[9-11] Initially, our group employed normal photoelectron diffraction (NPD)[12,13], in which oscillations over a limited low energy range were fitted with a LEED-like theory to derive structures. Later, ARPEFS, which is formally analogous to extended x-ray-absorption fine structure (EXAFS), was developed. In ARPEFS, one measures the angle-resolved photoemission intensity from a core level of the adsorbate as a

function of the photoelectron kinetic energy over a wide energy range (typically = 50 - 500 eV). Photoelectrons from the adsorbate can be elastically scattered by neighboring atoms: the measured photoemission intensity contains surface structural information due to the final-state interference. Unlike LEED, ARPEFS allows qualitative data analyses by Fourier transformation, giving rather direct access to the structural information. This is similar to SEXAFS, but ARPEFS yields path-length differences while SEXAFS gives interatomic distances between the adsorbate (source) and substrate (scattering) atoms. A quantitative structural analysis by ARPEFS requires multiple-scattering spherical-wave (MSSW) theory,[14] while single-scattering is usually applied in SEXAFS. With a MSSW level analysis, effects as subtle as small corrugation and relaxation near the substrate surface can be characterized. More recently, an ARPEFS study of c(2×2)S/Cr(001)[15] has provided new experimental insight into the depth to which ARPEFS can probe into the substrate surface. For this stiff lattice (high Debye temperature), path-length differences greater than 10 Å were discernable and were successfully modeled by the MSSW calculations. By performing ARPEFS measurements at low temperatures similar advantages would be expected with softer lattices.

In this chapter we report the first low-temperature ARPEFS study on an atomic adsorbate system. We chose the c(2×2)Cl/Cu(001) system for several reasons. First, we believed that a detailed study of the surface and near-surface structure of c(2×2)Cl/Cu(001) at such a high level of accuracy that the substrate surface relaxation including small corrugation can be revealed might resolve some discrepancies in the literature. In a LEED study, Jona et al.[1] determined that the Cl atoms adsorb in the fourfold symmetric hollow sites with a Cl-Cu interlayer spacing of 1.60(3) Å and a slightly expanded Cu-Cu first interlayer spacing of 1.85(3) Å. However, a Cl-Cu interlayer spacing of 1.53(2) Å was derived from a SEXAFS bond length of 2.37(2) Å in SEXAFS studies,[2,16] and Patel et

al.[17] reported substrate surface relaxation for c(2×2)Cl/Cu(001) by using a combination of x-ray standing wave and SEXAFS techniques, finding a 0.07 (4) Å outward relaxation of the first copper layer. Indeed, both the LEED and SEXAFS studies have shown the expansion of the Cu-Cu first interlayer spacing. An interesting question is the following: how does the substrate relax in this expansion? Is it an outward relaxation of the first copper layer, or a downward relaxation of the second copper layer, or do both the first and second copper layer move? Another motivation for this work was to study the surface-atom vibrational anisotropy using temperature-dependent ARPEFS. That part of the work will be reported separately.

This chapter is organized as follows. Section 2.2 gives the experimental details. Section 2.3 describes the procedures of data collection and reduction, and presents results of two types of analysis used to extract structural information: Fourier and multiple-scattering analysis. Section 2.4 discusses and compares the results. A summary and conclusions are given in section 2.5.

## 2.2 Experimental

The experiments were performed at the Stanford Synchrotron Radiation Laboratory on Beamline III-3 using a Ge(111) double-crystal monochromator. The Cl 1s photoemission spectra were taken in the kinetic energy range from 50 to 550 eV with photon energies from 2870 to 3370 eV. The resolution of the double-crystal monochromator was approximately 2 eV through this photon energy range. The double Bragg reflection geometry significantly enhanced the already high degree of linear polarization of the incident synchrotron radiation.[18] A polarization of $\geq$ 98 % was achieved.

The photoemission spectra were collected with a hemispherical electrostatic analyzer described previously.[19] The analyzer is mounted on a carriage which allows rotations under UHV conditions of 360 ° about a vertical axis and 100 ° about a horizontal axis. Under the operating conditions of 160 eV pass energy, the energy resolution of the analyzer is ~ 1 eV FWHM and the angular resolution of the input lens is ± 3°. The UHV experimental chamber also contains a four-grid LEED system for doing LEED and AES, an ion gun, and an effusive beam doser for sample preparation.

A copper single crystal was cut, oriented to within ± 1° of the (001) direction as determined by Laue backscattering, then mechanically polished and chemically etched. The final finished crystal was mounted on a high precision manipulator with a liquid nitrogen cooling system, allowing enough motion to adjust the orientation of the sample. In the low-temperature measurements, the sample was cooled to 110 ± 5 K as measured by a chromel-alumel thermocouple attached to the sample. The clean Cu surface was prepared by repeated $Ar^+$ ion sputtering and annealing to about 850 K until AES showed no carbon, nitrogen, oxygen, or sulfur contamination and a sharp p(1×1) LEED pattern was observed. The Cu(001) surface was exposed to $Cl_2$ through an effusive beam doser. A sharp c(2×2) Cl overlayer LEED pattern was produced by dosing $Cl_2$ at room temperature for about two minutes with the main chamber pressure below $5x10^{-9}$ Torr. This was followed by a 400 K annealing for two minutes to completely dissociate $Cl_2$ into atomic Cl.

The pressure in the experimental chamber was between $2x10^{-10}$ and $6x10^{-11}$ Torr during all the measurements. The sample was flashed to about 400 K every 6-9 hrs during data collection, and more often for the low temperature measurements. The ARPEFS measurements were performed at room temperature and 110 ± 5 K, and along the two emission directions [001] and [011] at each temperature. The experimental directions were

determined by a He-Ne laser autocollimation referenced to the experimental viewports with an accuracy of ± 2°. The experimental geometries are shown in Fig. 1. For the [001] geometry, photoelectrons were collected along the surface normal with the photon polarization vector 35° from the surface normal toward the [011] direction. The other geometry, with the photon polarization vector 48° off the surface normal almost lying in the [011] direction and with the emission direction co-linear with the photon polarization vector, is simply called the [011] geometry for convenience in the discussion below. These two geometries were chosen to highlight nearby backscattering atoms, utilizing the directional sensitivity of ARPEFS. Backscattering in the [001] emission direction is most sensitive to the substrate copper atoms directly below the Cl atoms. Emission along the [001] direction can thus determine interlayer spacings effectively. The [011] emission direction was selected to emphasize the substrate copper atoms along the [011] direction, including the nearest neighbors.

## 2.3 Data Analysis and Results

In this section, we describe the procedures for reducing a series of photoelectron spectra into $\chi(k)$ curves, which contain the surface structural information. This information was extracted from the $\chi(k)$ curves in two ways: by Fourier analysis and by multiple-scattering spherical-wave (MSSW) analysis. Fourier analysis gave the adsorption site and approximate geometrical parameters. More precise values were obtained by comparing the experimental data to the MSSW calculations using an R-factor (reliability-factor) as a quantitative measure of the fit. An automatic routine was used to search the structural parameters at the minimum R-factor. Detailed procedures are described below.

### 2.3.1 Data Reduction

Four sets of ARPEFS data, at two geometries and two temperatures, were taken on separately prepared samples. A series of 80 - 100 photoemission spectra was taken for a given data set, in equal electron wave-number increments $\Delta k = 0.08 - 0.10$ Å$^{-1}$. Each photoemission spectrum was centered on the Cl 1s photoelectron peak, with an energy window of 25 - 30 eV. In the energy region where Auger peaks appeared (181 eV), an increment of 0.08 Å$^{-1}$ and an energy window of 30 eV were used.

In recent ARPEFS studies,[15,20] a Voigt function (Gaussian convoluted with a Lorentzian) was used to model the photoelectron peak, to account for lifetime broadening (Lorentzian) of the core hole and instrumental broadening (Gaussian) due to the monochromator and analyzer resolution. The Voigt function was found to fit the core-level photoelectron peak more accurately than a pure Gaussian function. In this work, each individual photoemission spectrum was fitted with three functions: a Voigt function to model the core-level photoelectron peak, a Gaussian convoluted with a step function (G step) to describe the inelastically-scattered electrons associated with the photoelectron peak, and an experimentally-measured background to account for other inelastic scattering processes. The quantity of interest was the area of the Voigt peak. It was necessary to normalize each photoemission spectrum to compensate for the irregularities in the photon flux, as well as for the analyzer transmission function. The experimental background consisted of three photoemission scans covering the kinetic energy range of 40 - 550 eV. Each scan was taken at a different photon energy so that the Cl 1s photoelectron peak lay about 10 eV below the lowest kinetic energy in each spectrum. A "master" background curve was taken for each geometry and temperature. It was used both for the the least-square fitting and for the normalization of each photoemission spectrum.

Since the Lorentzian width due to lifetime broadening is independent of the experimental conditions, it was fixed in the least-square fittings for all the photoemission spectra. The width of the G-step was kept at the same value as the width of the Gaussian part of the Voigt function. Lorentzian widths in the range of 1.0-1.5 eV, which is somewhat larger than the natural K-shell linewidth of 0.65 eV for Cl calculated by Krause and Oliver,[21] gave equally good fits. A final value of 1.5 eV was used. Each individual photoemission spectrum was normalized by a scale factor to the background function obtained in the least-square fitting. The total photoemission intensity I(E) was generated by plotting the area of each Voigt function as a function of the photoelectron kinetic energy taken as the mean energy of each Voigt function. The final I(E) curve was divided by the kinetic energy to compensate for the analyzer transmission function.

In analogy to EXAFS, the total photoemission intensity I(E) consists of a slowly varying atomic-like function and an oscillating contribution caused by the interference effects. I(E) can then be described as:

$$I(E) = [\chi(E) + 1]\, I_0(E) \quad , \qquad (1)$$

where $I_0(E)$ is a slowly varying atomic-like function and $\chi(E)$ is the oscillatory interference function which can be determined by removing the slowly varying function $I_0(E)$ from the total photoemission intensity I(E):

$$\chi(E) = \frac{I(E) - I_0(E)}{I_0(E)} \quad . \qquad (2)$$

This is finally the function of interest in ARPEFS, analogous to EXAFS.

Theoretically, $I_0(E)$ is essentially the Cl 1s atomic cross section, which can in principle be calculated from the atomic wave functions. In reality, since the exact form of $I_0(E)$ is not completely known and $I_0(E)$ contains only the very low frequency part of I(E), a low-order polynomial or a smooth cubic spline has been applied to simulate $I_0(E)$, in

analogy with EXAFS.[22] Experimentally, however, the low frequency part of I(E) contains not only the slowly varying atomic-like cross section but also some ARPEFS structures at low path-length differences, as well as any contributions introduced by the processes of data collection and experimental conditions. For example, movements of the photon beam and changes in the slope of the experimentally-measured background during data collection would give rise to low frequency components in the $\chi(E)$ curves. The choices of appropriate $I_0(E)$ were made by requiring the minimal intensity of the Fourier amplitude at zero path length in some of the previous studies.[15,23] However, this choice of $I_0(E)$ is arbitrary, and the $\chi(E)$ curves generated by using different low-order polynomials can vary. The structural information at the scattering path-length differences less than about 1.5-2.0 Å is therefore not reliable, being either distorted or completely removed. Since there can be no real structural information contained in the path-length differences less than 2 Å for the [001] data and 1.5 Å for the [011] data, low-order polynomials were first used to construct $\chi(E)$ curves in the current study, then Fourier filtering was applied to filter out the frequencies below those values. The resulting $\chi(E)$ curves are independent of the choices of the low-order polynomials. In comparing the experimental results with theory, the same procedures were used to filter the theoretical curves.

The experimental $\chi(E)$ curves are shown in Figs. 2 and 3 for the [001] and [011] data, respectively, at the two different temperatures. It is clear that the oscillation amplitudes of $\chi(E)$ at the lower temperature are greatly enhanced as compared with those at room temperature. The oscillation patterns are matched very well at the two temperatures.

Once reliable $\chi(E)$ curves were obtained, they were converted to $\chi(k)$ for the purposes of Fourier transformation and comparison with theory, using the De Broglie relation:

$$k = \hbar^{-1} \sqrt{2m_e (E + V_0)} \ , \qquad (3)$$

where $m_e$ is the electron rest mass and $V_0$ is the inner potential of the solid. The exact value of $V_0$ is unknown, but for copper $V_0$ is around 10 eV. We treated $V_0$ as an adjustable parameter in the fits, and determined its value as $10 \pm 2$ eV.

### 2.3.2 Fourier Analysis

Fourier analysis of the $\chi(k)$ curve in ARPEFS yields the path-length differences

$$\Delta R_j = r_j (1-\cos\theta_j) \ , \qquad (4)$$

which follows from single-scattering ARPEFS theory which gives

$$\chi(k) = 2 \sum_j A_j(k) \, e^{-\sigma_j^2 (1-\cos\theta_j) k^2} \, \cos[k r_j (1-\cos\theta_j) + \phi_j] \ , \qquad (5)$$

where $A_j(k)$ contains the elastic scattering amplitude modified by the inelastic losses and aperture integration, $r_j$ is the distance between the photoemitter and j th scattering atom , $\theta_j$ is the scattering angle at the j th atom, and $\phi_j$ is the scattering phase shift. The temperature effect is introduced as a Debye-Waller factor, where $\sigma_j$ is the mean square relative displacement between the photoemitter and the j th scattering atom, projected on the photoelectron momentum change direction. The Fourier peaks appear at the path-length differences $\Delta R_j$. Structural information can therefore be obtained directly from the Fourier spectrum of each emission geometry.

The Fourier transformation procedure was described previously.[5] Fourier spectra for the [001] and [011] data at the two temperatures are given in Figs. 4 and 5, respectively. In each case, the spectral features agree very well for the two temperatures, while the amplitudes at the lower temperature are enhanced. Strong Fourier peaks are present even at path-length differences greater than 10 Å for the lower-temperature spectra.

This is more prominent for the [001] data where real spectral features up to 20 Å path-length difference are evident. Thus, scattering from deeper substrate layers makes significant contributions to the ARPEFS signal at low temperature, providing an opportunity to extract both surface and near-surface structural information more accurately.

It is known from previous LEED (Ref. 1) and SEXAFS (Ref. 2) studies that the Cl atom adsorbs at the four-fold hollow site of the Cu(001) surface. We can in fact obtain this adsorption geometry simply by Fourier analysis of the ARPEFS data. Forward ($\theta_j$ = 0°) and backward($\theta_j$ = 180°) scatterings give the strongest signals in the k range of our data. However, for adsorbate source atoms, forward scattering alone does not occur in our geometries, which were chosen to highlight the backscatterers. Thus, backscattering provides the strongest ARPEFS signals, producing the dominant peak evident in each Fourier spectrum. From Eq. (4), the strongest peak due to backward scattering should appear at a path-length difference $\Delta R_j \approx 2r_j$ if a near-neighboring substrate atom lies at a distance $r_j$ directly behind the adsorbate atom. In Fig. 4, the strong peak at $\Delta R_j \sim 6.9$ Å in the [001] direction is thus assigned to the Cu atom directly below the Cl atom. An atop adsorption site could be considered as an alternative candidate structure. But a Cl atom in an atop site would then have a bond length of ~ 3.45 Å, too long for the Cl-Cu bond, and the peaks at ~ 3.3 Å and ~ 5.0 Å would be unexplained. In addition, an atop site would not give a 4.8 Å peak in the [011] emission data, thus an atop site is excluded. The peak at ~ 4.8 Å offers a reasonable estimate of the bond length of ~ 2.4 Å for either a bridge site or a four-fold hollow site. However, a bridge site, having no strong backscatterer, would not give a strong peak at ~ 6.9 Å in the [001] emission direction. Therefore, the four-fold hollow site is the favored high-symmetry adsorption site for the c(2×2)Cl/Cu(001) system, in agreement with previous LEED[1] and SEXAFS[2,16] results. Similar arguments rule out alternative lower symmetry sites.

Once the adsorption site is determined, the main features in the Fourier analysis can provide qualitative structural information about the c(2×2)Cl/Cu(001) system. Since multiple scattering is initially forward-focusing, which does not introduce an additional path-length difference, the relatively strong and distinctive Fourier peaks can usually be assigned to specific scattering path-length differences, with the proviso that a given peak can arise from two or more sites. Let us discuss the [011] Fourier spectra shown in Fig. 5 first. The peak at ~ 2.8 Å corresponds to scattering through an angle of ~ 116° from two nearest-neighboring atoms symmetrically located at either side of the plane containing the [001] and [011] directions, and the strongest peak at ~ 4.8 Å, to backscattering from the one of the four nearest-neighboring atoms that lies directly behind Cl along the [011] direction. This gives a Cl-Cu bond-length of ~ 2.4 Å, yielding a vertical distance of Cl to the first copper layer of ~ 1.6 Å. Scattering from the nearest neighboring atom at $\theta_j \approx 84°$ is almost negligible, because cos 84° = 0.10 in Eq. (5). If we consider a (011) plane including an atom labelled 1 in Fig. 5 as the first (011) plane perpendicular to the emission direction, the two peaks at ~ 7.6 Å and ~10.2 Å can be attributed mainly to scattering from the atoms in the second and third Cu(011) planes, respectively. The peaks at ~ 13.0 Å and ~ 15.0 Å should correspond largely to scattering from the fourth and fifth Cu(011) layers. These two peaks have more complicated origins, because at these high path-length differences scattering processes are very complicated: multiple scattering becomes important , and many scatterers are involved.

A similar analysis can be applied to the [001] Fourier spectra, shown in Fig. 4. As noted earlier, the strongest peak, at ~ 6.9 Å, is due to backscattering from the second layer copper atom directly below Cl, giving a ~ 3.45 Å separation between Cl and this atom. Together with the first-layer spacing of 1.6 Å, this already suggests a larger interlayer spacing than the bulk spacing (1.807 Å). The Fourier features at path-length differences

from 6.9 Å to 10.0 Å arise mostly from scattering by atoms in the second copper layer. The relatively strong Fourier peaks at high path-length differences ~ 10.7 Å and ~ 15.0 Å in the lower temperature data contain structural information from deeper substrate layers than do the room temperature data. The peak at ~ 10.7 Å has a large contribution from the four atoms in the third copper layer, while the broad peak at ~ 15.0 Å includes mainly scattering from atoms in the fourth copper layer. The peaks at ~ 3.3 Å and ~ 5.0 Å arise predominantly from scattering through 131° by the four nearest-neighboring atoms, which have a geometric path-length difference of ~ 4.0 Å, where no peak is observed in the [001] Fourier spectra. The Generalized Ramsauer-Townsend effect [5,23] causes peak splitting.

We have thus obtained approximate geometric structural parameters by assigning the main Fourier peaks. However, several factors limit this method to a qualitative analysis. First, one usually cannot simply attribute a peak to a single type of scattering process, because multiple scattering is involved and many scattering paths can give approximately the same path-length difference, especially at higher path-length differences. Furthermore, a path-length difference directly derived from the Fourier analysis contains not only the geometric difference but also the scattering phase shift $\phi_j$ shown in Eq. (5). Unfortunately, the back transformation of Fourier spectra cannot completely separate the geometric path-length difference from the scattering phase shift because of single and multiple scattering involved in the effective phase shift. Therefore, MSSW calculations are required to obtain quantitative structural information.

### 2.3.3 Multiple-Scattering Analysis

In this section, we present a quantitative analysis of the ARPEFS data based on multiple-scattering spherical wave (MSSW) calculations, after Barton, Robey and

Shirley.[14] The Taylor-series magnetic-quantum-number expansion (TS-MQNE) approximation permits economical MSSW calculations and takes into account important physical aspects of the problem.

A MSSW calculation requires several input parameters, both structural parameters of adsorbate-substrate geometry and nonstructural parameters including atomic partial wave phase shifts, Debye temperatures, mean-free path, emission and polarization directions, detector aperture, experimental temperatures, and inner potential. The theory is most sensitive to the structural parameters, but the choice of the nonstructural parameters affects the accuracy of the derived structural information. We first consider the nonstructural parameters. The copper phase shifts were from previous calculations,[23,24] while the chlorine phase shifts were calculated from a modified program developed by Pendry for LEED[25] and a potential obtained from atomic Hartree-Fock wave functions, which were truncated at a muffin-tin radius $R_{max}$. Values of $R_{max}$ from 1.0-1.8 Å were used in the calculations and an optimum value of $R_{max}$ was found to be 1.35 Å. Phase shifts at different values of $R_{max}$ did not cause strong differences in the results of the MSSW analysis. The exchange potential was calculated in the Xα approach with the factor α (0.723) used by Schwarz.[26] A total of 16 partial wave phase shifts for Cl were calculated from 40 to 600 eV.

The thermal effect was taken into account by a correlated Debye model which included surface-layer dependent and anisotropic mean-square relative displacements (MSRD).[14] The copper bulk Debye temperature was taken as 343 K, while the copper surface Debye temperature was set to 243 K assuming that the surface copper atoms have an MSRD twice as that of the bulk. The Debye temperature for the Cl overlayer was estimated to be 325 K from the Cu surface Debye temperature adjusted for the difference in masses. Actually, surface Debye temperatures for both Cl and Cu are varied in the

calculations based on the above estimated values. The mean free path was included in an exponential factor, $e^{-r/\lambda}$, with $\lambda = ck$. The value of $c = 0.753$ for Cu is similar to that for Ni.[27] In addition, the emission and polarization angles ($\pm$ 3°), the experimental temperature ($110 \pm 10$ K) and the inner potential ($10 \pm 5$ eV) were allowed to vary in the calculations.

### 2.3.3.1 Site Determination

Fourier analysis established a four-fold hollow adsorption site. Comparisons of the MSSW calculations with the experimental data confirm this result. The $\chi(k)$ curves for three unreconstructed adsorption geometries (atop, bridge and four-fold hollow ) were calculated using a Cl-Cu bond length of 2.41 Å derived from the Fourier analysis. The calculated curves are compared with the experimental data in Figs. 6 and 7 for the [001] and [011] directions, respectively. By visual inspection, the calculated curves from the four-fold hollow geometry most closely resemble the experimental data. Still, large differences exist even for the four-fold hollow geometry, based on these nonoptimized trial geometrical parameters. To derive a detailed quantitative structure, we therefore optimized both structural and nonstructural parameters to produce the best agreement between theoretical and experimental $\chi(k)$ curves.

### 2.3.3.2 Structural Determination

First, both the [001] and [011] experimental $\chi(k)$ curves, at both temperatures, were smoothed by Fourier filtering out the high-frequency portion of the data (path-length differences larger than 16.5 Å). Although there were some real signals beyond 16.5 Å,

the cutoff at this value retains all the major contributions from down to the fourth substrate layer and eliminates high-frequency noise at the same time, facilitating comparisons with the calculated curves. All subsequent comparisons of theory with experiment were done with the filtered data, 2.0-16.5 Å for the [001] data, and 1.5-16.5 Å for the [001] data. The MSSW calculations were performed with the same path-length difference cutoffs.

The comparison was based on an R-factor analysis, with optimum geometrical parameters being obtained when a minimum R-factor, defined by

$$R = \frac{\int[\chi_E(k) - \chi_T(k)]^2 dk}{\int \chi_T(k)^2 dk} , \qquad (6)$$

was reached. Here E and T denote experiment and theory. The R-factors were calculated over the k range 5.0-11.0 $Å^{-1}$.

It would be ideal to search out a global minimum in a large parameter space by varying all the possible parameters simultaneously. Unfortunately, all the nonstructural and structural parameters together give too many variables to handle at one time. In early ARPEFS analyses, this problem was simplified by varying one or two structural parameters at a time, while most of nonstructural parameters were kept fixed. Because some parameters are coupled, finding a global minimum by this approach can be elusive. In the present study, an automatic routine was therefore used to search many more parameters simultaneously with a reasonable number of iterations. Normally, it took about 200-400 iterations to achieve a convergence of R-factors for searching about 5-9 parameters at a time. This routine started from an unreconstructed trial geometry with physically reasonable boundaries. The structural parameters obtained by varying different groups of parameters at a time with different initial guesses are very consistent, showing that a minimum found in this way should be an absolute minimum. Some of the

nonstructural parameters were also varied along with the structural parameters, improving the accuracy of the structural parameters and allowing us to detect subtle changes in the surface structure.

No lateral substrate relaxation was included because of the c(2×2) structure of the Cl/Cu(001) system. We first optimized the following perpendicular distance parameters: the Cl-Cu(1) distance, the Cl-Cu(2a) distance to the atopped-site second layer copper, the Cl-Cu(2o) distance to the uncovered-site second layer copper, the Cl-Cu(3) distance, the "Debye temperatures" of Cl, in the parallel and perpendicular directions, respectively, the emission angle (polar angle) and the inner potential $V_0$ . For convenience, we use a short notation [001]-(110 K) for the [001] data at 110 K, and similarly for other data sets. The Cl-Cu(4) distance was optimized from the [001]-(110 K) data. Nonstructural parameters such as the Debye temperatures, the emission angle and the inner potential affected the extended fine structure more than did other nonstructural parameters, and they tended to be correlated with the structural parameters. Thus, all the major structural parameters and the important nonstructural parameters were taken as variables in the automatic routine. The emission angles were found to be $< 1°$ off from 48° for the [011] data, and $< 3°$ off the normal for the [001] data. The inner potential for the optimum geometry was $10 \pm 2$ eV, and the experimental temperature was optimized to be $110 \pm 5$ K. The structural parameters obtained from the four data sets were consistent, especially for the data at different temperatures with a given geometry. R-factor minima lay in the small range R = 0.06 - 0.15 in the various calculations.

The structural parameters determined from the above analysis are set out in Table I. The Cl-Cu(1) distance values lie within 0.01 Å among the four data sets, and the Cl-Cu(2a) distances are larger than the Cl-Cu(2o) distances within each data set. The R-factor

minima were smaller for a given geometry at the lower temperature, due to the increased signal to noise ratio.

The directional sensitivity of ARPEFS and the sensitivity of a given data set to each structural parameter are displayed by two-dimensional error contour plots. Fig. 8 shows contours for the [001]-(110 K) and [011]-(110 K) data, calculated by varying two parameters, Cl-Cu(1) and Cl-Cu(2a), while other parameters were fixed in their optimum values obtained previously. The [001] contour displays a very steep curvature when varying the Cl-Cu(2a) distance, indicating that the [001] data are more sensitive to Cl-Cu(2a), because there is a backscatterer Cu2a directly below Cl along the [001] direction. The [011] contour shows a greater sensitivity to the Cl-Cu(1) distance due to the existence of a backscatterer in the first copper layer directly behind Cl along the [011] direction. The contours generated by varying Cl-Cu(2a) and Cl-Cu(2o) for the [001]-(110 K) and [011]-(110 K) data are shown in Fig. 9. Not surprisingly, the [001] contour shows higher sensitivity to the Cl-Cu(2a) distance. However, a minimum along Cl-Cu(2o) is still well defined. The [011] contour exhibits a rather different shape. It shows similar sensitivities both to the Cl-Cu(2a) and the Cl-Cu(2o) distances with a relatively broad minimum, because the difference between the scattering angles for the uncovered-site and atopped-site copper atoms are not very significant, and the scattering amplitudes at these angles are relatively low.

As pointed out in the Fourier analysis, scattering off the third and the fourth copper layers makes significant contributions to the extended fine structure, especially for the [001]-(110 K) data. Fig. 10 shows comparisons of the [001]-(110 K) data filtered out to 20 Å with the MSSW calculations at cutoffs in the path-length differences up to 10 Å, 13 Å and 20 Å. By visual observation, the MSSW calculations for the 10 Å and 13 Å cutoffs, where the contributions from copper layers deeper than the third and fourth are

excluded, respectively, do not adequately model the high frequency portion of the experimental data, while the MSSW calculation up to 20 Å path-length difference compares more favorably. Here again, we demonstrate that the structural information from the deeper substrate layers is present in the extended fine structure and can be successfully modelled by the MSSW calculation including the scatterers from those layers.

Figure 11 shows a contour for the Cl-Cu(2o) and Cl-Cu(3) distances for the [001]-(110 K) data, which is more sensitive to the Cl-Cu(3) distance than to the Cl-Cu(2o) distance. The relatively steep curvature with respect to Cl-Cu(3) yields an accurate value for this parameter. Figure 12 presents a contour for Cl-Cu(3) versus Cl-Cu(4). The sensitivity to Cl-Cu(3) is expected to be larger than to Cl-Cu(4). Surprisingly, the sensitivity for the Cl-Cu(4) distance is still quite good. The 001-300K data set no large Fourier peaks at path-length differences greater than 10 Å (Fig. 4), and the Cl-Cu(3) distance derived from these data has a larger uncertainty. Thus, the lower temperature ARPEFS data improve the accuracy of the structural parameters for the deeper substrate layers.

### 2.3.3.3 Error Analysis

The error contour plots described previously indicate the relative sensitivity of a given data set to a structural parameter. However, it is important in structural determinations to evaluate the errors associated with each structural parameter. There are two kinds of error, statistical and systematic.

Statistical error analysis in non-linear least-squares fitting is based mainly on the $\chi^2$ method,[23,28] where $\chi^2$ is defined by

$$\chi^2 = \sum_j \{ \frac{1}{\sigma_j^2} [ Y_j - Y(x_j) ]^2 \} \quad . \tag{7}$$

We shall follow the universal convention and retain the symbol $\chi$ here, not to be confused with $\chi(k)$ or $\chi(E)$. Here $\sigma_j$ is the standard deviation of each data point $Y_j$, $Y(x_j)$ is the fitting function. A reduced $\chi^2$ is given by:

$$\chi_v^2 = \frac{\chi^2}{v} \quad , \tag{8}$$

with $v = N - n - 1$ representing the number of degrees of freedom, N the number of data points, and n the number of fitting parameters. The optimum values of parameters are obtained by minimizing $\chi^2$ with respect to each parameter, $P_j$, simultaneously. If the variation of $\chi^2$ with respect to each parameter is independent of the values of the others, and the reduced $\chi_v^2 \approx 1$, then the statistical error associated with each parameter can be obtained from the curvature of the $\chi^2$ parabola: that is, the standard deviation, $\sigma_{p_j}$, of a parameter $P_j$ can be expressed as

$$\sigma_{p_j}^2 = \frac{2}{\partial^2\chi^2/\partial P_j^2} \quad . \tag{9}$$

If $\chi^2$ is a parabolic function, $\chi^2 = a P^2 + b$, then

$$\sigma_{p_j}^2 = \frac{1}{a} \quad . \tag{10}$$

The procedure for extracting structural parameters by using the automatic search routine can be considered as the non-linear least -squares fitting of theoretical $\chi(k)$ functions to experimental data while optimizing several parameters simultaneously. No correlations between the structural parameters were found from the shapes of the error contour plots. Therefore, in principle, errors could be estimated by the $\chi^2$ method. However, even for the best ARPEFS fit, the difference between theory and experiment exceeds statistical expectations, and $\chi^2_{v_{min}} > 1$, where $\chi^2_{v_{min}}$ is the value at the minimum

of the $\chi^2$ parabola. In this case, the standard deviation of a parameter can be modified by multiplying $\sigma_{p_j}{}^2$ with $\chi^2_{v_{min}}$ ( = b/v) to get

$$\sigma'_{P_j}{}^2 = \frac{b}{a\ v}. \qquad (11)$$

Thus, the statistical errors are determined by the $\chi^2$ curvature a (the sensitivity to parameters), its minimum value b (the quality of fits), and the number of degrees of freedom v. Steeper curvature, smaller minima of the $\chi^2$ parabola, and more degrees of freedom give smaller statistical errors.

The parameters a and b in Eq. (11) have straightforward meanings, but v cannot be evaluated so simply. The relation v = N-n-1 is valid only if the N data points are independent. In a typical ARPEFS $\chi(k)$ curve there may be 100 or more data points, but the curve could be described by a substantially smaller number of points. The exact number needed, $N_{min,}$ and therefore the values of $v = N_{min} - n - 1$ and $\sigma$, can be estimated in several ways, which yield slightly different results. In this work we use a method based on a " spline-interpolation " step in the data analysis. This step is the interpolation of the raw $\chi(k)$ data onto an evenly-spaced mesh in k prior to Fourier transformation and simulation. $N_{min}$ is determined by reducing the mesh interval until the interpolated curve matches the raw data "curve" within the standard deviation $\sigma_j$ of each data point. Application of this method to the present 110 K curves yielded $N_{min}([001]) \sim 48$ and $N_{min}([011]) \sim 40$. This difference was expected because for [001] the $\chi(k)$ curve shows more structure.

In summary, the statistical error $\sigma_{p_j}$ in a given parameter $P_j$ depends upon v, varying as $v^{-1/2}$ [Eq. (11)]. We note that other methods of estimating v might give somewhat different results. However, even a factor of 2 difference in v would only change the statistical error estimate by $\sqrt{2}$. We therefore believe that this analysis gives a satisfactory estimate of the statistical error.

Table I lists, in columns 2-5 ( upper panel ), the statistical errors (standard deviations ) of each parameter for the four data sets, determined as described above. Column 6 gives the average value of each parameter determined by suitable weighting of the values in columns 2-5, using standard statistical methods.

Scatter in the values of each derived parameter, among the four data sets, can also be used to estimate the standard deviation in the mean value. In fact, if we did not already have a good estimate of our statistical $\sigma_{p_j}$, this would be our only way to assess them. While four values cannot simulate a Poisson, let alone a Gaussian, distribution, use of the "scatter" equation,

$$\sigma_j^2 = 1/4 \sum_i ( P_{ji} - \bar{P}_j )^2 \qquad (12)$$

gives an indication of the error to be associated with scatter in the derived values, per se. Column 7 in Table I lists the simple averages of the derived parameters, taken from columns 2-5, together with standard deviations determined from Eq. (12).

The close agreement between the derived values of parameters in columns 6 and 7, in which the statistical errors were estimated in very different ways together with the small standard deviations, reinforces our belief that the statistical uncertainty in these parameters is quite small. Column 8 lists our best values for these parameters, which we take as the values in column 6 - clearly preferred because the individual value from which they are derived are weighted - and the errors from the larger of those in columns 6 and 7. It seems inescapable that systematic errors contribute to the scatter of the derived parameter values, and we believe that this effect shows up in the generally larger errors in column 8. Conversely these errors probably give a reasonable estimate of the uncertainties due to combined statistical and systematic errors, with one exception, discussed below. We can

estimate the uncertainty due to these systematic errors, which might include the effect of misalignment, background evaluation errors, etc., from the differences between the mean values in columns 6 and 7. By this criterion, these systematic errors are also quite small.

The above discussion of systematic errors should apply to errors which lead to random scatter in the results. If there are also other systematic errors present which bias the derived parameter values either high or low, such errors will of course not show up even in column 7.

We cannot identify any systematic errors in the measurements that would bias the derived interatomic distances high or low. Path-length differences are most closely related to the electron's momentum vector k, which follows from the kinetic energy. There are always experimental errors, but no bias, associated with these parameters.

The theoretical modelling process could in principle introduce bias, by systematically over- or under- estimating a non-structural parameter such as the crystal potential $V_0$ or the scattering phase shift $\phi_j$. We note that, in contrast to EXAFS, for which a shift $\Delta$ R arises from the source-atom phase shift ( and is evaluated using model compounds), there is no source-atom phase shift in the ARPEFS scattering process because of cancellation: the direct and scattered waves both leave the source atom only once. As for $V_0$ and $\phi_j$, we know of no reason to expect a large bias in R values from these parameters.

Finally, the theoretical modelling process could introduce bias by omitting a physical process. Our candidate here would be dynamic screening changes as the source atom decays by an Auger cascade which the photoelectron is still close. The integrated effect might vary monotonically with k, introducing some bias. Consideration of such processes might be a fruitful topic for theoretical study, but to attribute a systematic error based on present knowledge would be too speculative.

In summary, we find no evidence for error sources that would systematically bias our results, and we therefore quote as our best values and standard deviations the values given in column 8 of the table I. In comparing these results, especially the errors, with values derived from other studies, caution should be exercised, because the quoted errors are often not standard deviations. In electing to quote standard deviations, which vary in our results from 0.003 Å to 0.033 Å, we have sought to retain this variation, and have eschewed the temptation to quote all errors as ca. ± 0.02 Å, in hopes of advancing a more quantitative approach to estimating errors.

### 2.3.3.4 Results

The best fits to the experimental $\chi(k)$ curves are shown in Figs. 13 and 14 for the [001] and [011] data, respectively. Agreements between the theoretical and experimental curves are excellent. Figure 15 shows the top and side views of the c(2×2)Cl/Cu(001) structure, labelling the layer spacing for which fitted values are listed in Table I. The Cl-Cu(1) distance of 1.604(5) Å, fits with a Cl-Cu bond length of 2.416(3) Å. The Cl-Cu(2a) distance of 3.453(11) Å then gives a Cu(1)-Cu(2a) distance of 1.849(12) Å, showing an expansion from the bulk value (1.807 Å), while the Cl-Cu(2o) distance of 3.412(21) Å yields a Cu(1)-Cu(2o) distance of 1.808(21) Å. The difference between Cl-Cu(2a) and Cl-Cu(2o) of 0.041(24) Å reveals a small corrugation of the second copper layer. Furthermore, the Cl-Cu(3) and Cl-Cu(4) distances were found to be 5.222(25) Å and 7.023(22) Å, respectively, giving the Cu(3)-Cu(4) distance of 1.801(33) Å and Cu(2o)-Cu(3) distance of 1.810(33) Å, in good agreement with the bulk spacing. By difference, the Cu(2a)-Cu(3) distance of 1.769(27) Å shows a contraction from the bulk value. The magnitude of this contraction in Cu(2a)-Cu(3) is approximately equal to that of

the expansion in Cu(1)-Cu(2a). Assuming the fourth copper layer is in the bulk position, from the bulk-like spacings of Cu(3)-Cu(4) and Cu(2o)-Cu(3), we infer that the third layer and uncovered-site second-layer copper atoms must also lie in the bulk positions.

## 2.4 Discussion

The distance Cl-Cu(1) of 1.604(5) Å obtained from the ARPEFS study is in excellent agreement with the LEED result,[1] but not with the SEXAFS result of 1.53 Å.[2,17] We have calculated $\chi$(k) curves based on this SEXAFS value for the Cl-Cu(1) distance and the other parameters as obtained from the current ARPEFS study. These curves are compared with two experimental $\chi$(k) curves in Fig. 16, to test the sensitivity of ARPEFS to the Cl-Cu(1) parameter. By visual inspection, the agreement is very poor; the R-factors are about 3 and 5 times larger than those for the [001] and the [011] ARPEFS optimum geometries, respectively. There are large shifts between the theoretical and experimental curves for the [011] geometry, but not so much for the [001] geometry, because scattering from the Cu2a atom dominates the [001] $\chi$(k) curve. In these fits, the inner potential $V_0$ was optimized to be ~ 10 eV from previous studies.[5,27] Even if a larger value of 15 eV was used in an effort to reduce the shifts for the [011] geometry, the agreement is still poor. It is also of interest to compare the Cl-Cu bond length as obtained from SEXAFS and ARPEFS, because this is the parameter which SEXAFS measures most directly. From Table I, we note that the SEXAFS value of 2.37(2) Å is only 1.9 % below what we believe to be the correct value of 2.416(3) Å: quite close by even fairly recent standards of surface structure determinations.

Since the third copper layer remains in the bulk position, by subtracting the bulk interlayer spacing twice from the Cl-Cu(3) distance of 5.222(25) Å, we can determine the

distance of Cl above the bulk-extrapolated first copper layer to be 1.608(25) Å, in excellent agreement with our Cl-Cu(1) distance of 1.604(5) Å with the surface reconstruction taken into account, and the result 1.60(4) Å obtained from the x-ray standing wave measurement.[17] Therefore, we conclude that there is no outward relaxation of the first copper layer, contrary to the results of Patel et al.[17] However, it has been shown that there was indeed an expansion of the topmost interlayer substrate spacing from three different techniques: ARPEFS, LEED, and SEXAFS. This expansion is mainly due to the downward relaxation of the second copper layer, based on the facts that there was no relaxation of the first copper layer and there was a contraction in the Cu(2a)-Cu(3) distance. This demonstrates that the lower temperature ARPEFS study can probe relaxation of not only the first substrate layer but also deeper layers relative to the bulk positions. Hopefully, the results obtained from this work can provide some experimental guidance for the theoretical work on adsorbate-induced relaxations.

Studies on the clean Cu(001) surface[29,30] showed a (1.1 ± 0.4) % contraction of the topmost interlayer spacing, while both LEED (Ref. 1) and this work showed an expansion of about 2% when Cl adsorbs on the clean surface, as compared with the bulk spacing, giving an expansion of about 3% with respect to the spacing of the clean Cu(001) surface. The (1.1 ± 0.4) % contraction of the clean surface resulted mostly from the inward movement of the first copper layer relative to the bulk position, according to a theoretical study.[31] Thus, with adsorption of Cl on the clean surface, the outward movement of the first copper layer and the downward movement of the second copper layer lead to a 3% expansion between the first and the second copper layers. Furthermore, the ARPEFS study revealed a small corrugation of the second copper layer, not observed by other techniques. This corrugation is understandable because atoms in the even

substrate layers are in two symmetry-inequivalent atomic sites relative to the adatoms for the c(2×2) structure.

The occurrence of the corrugation and expansion induced by the adsorption of Cl indicates that chemical bonding between the adsorbate and the substrate atoms modifies the surface and near-surface structure, inducing relaxation of the substrate layers. The mechanism of the relaxation may be very complicated, but we propose a simple physical picture. The metal-metal bond weakening induced by adsorption is probably the main factor in causing the expansion of the topmost interlayer spacing. In the case of c(2×2)Cl/Cu(001), the expansion due to metal-metal bond- weakening is expected to affect the atopped-site atoms directly below Cl more than the uncovered-site atoms, causing corrugation of the second copper layer, where the atopped-site atoms are displaced further away from the adsorbate. This kind of corrugation has been observed in other systems studied by ARPEFS.[27,32] In addition, a recent LEED study on c(2×2)O/Ni(001) (Ref. 33) showed a similar corrugation and an even larger expansion of the second substrate layer. In the O/Ni(001) system, the adsorbate O sits much closer to the metal substrate surface than the Cl atom, yielding a stronger interaction between the adsorbate and the metal substrate surface. A more complete understanding of the substrate surface relaxation induced by adsorbates would require a better knowledge of the nature of the surface chemical bonding.

## 2.5 Conclusion

We have presented a detailed study of the c(2×2)Cl/Cu(001) adsorption-geometry and substrate surface relaxation using low-temperature ARPEFS. Fourier analysis and the multiple-scattering spherical-wave (MSSW) analysis were applied in this study. Fourier

analysis yielded the adsorption site and the qualitative structural information, based on interpreting the features in the Fourier spectra with a single scattering model. Multiple-scattering analysis yielded more quantitative structural information by comparing the experimental data with the MSSW calculations based on the R-factor analysis. We conclude that the Cl atom adsorbs in the four-fold hollow site 1.604(5) Å above the first copper layer, giving a Cl-Cu bond length of 2.416(3) Å, in excellent agreement with the LEED result.[1] We have also observed that there is a 2% expansion of the separation between the first copper layer and the second atopped-site copper layer, and a small corrugation of the second copper layer where the atopped-site copper atoms are further away from the adsorbate Cl atom.

Real features in the Fourier spectra of the lower temperature data can be seen at path-length differences greater than 15 Å. The experimental data can be successfully modelled by the MSSW calculations by considering the path-length differences up to 16.5 Å. The lower temperature ARPEFS study has provided accurate near-surface structural parameters for the deeper substrate layers, 5.222(25) Å for the distance of Cl to the third copper layer, 7.023(22) Å for the distance of Cl to the fourth copper layer, yielding a bulk-like interlayer spacing between the third and the fourth copper layers. More significantly, no relaxation of the c(2×2)Cl-covered first copper layer with respect to the bulk position has been observed from the accurate near-surface structural information in the current work, which is inconsistent with the previous result obtained with a combination of the x-ray standing wave and SEXAFS techniques.[17] Instead, the downward relaxation of the second atopped-site copper layer results in an expansion of the topmost interlayer spacing, while the second uncovered-site copper layer remains in the bulk position.

We have demonstrated that low-temperature ARPEFS can probe deeper substrate layers, where information about the substrate surface relaxations relative to the bulk

positions can be obtained. Therefore, low-temperature ARPEFS holds the promise to completely and accurately map out surface and near-surface structures for adsorbate systems.

# References


* Present address: Department of Physics, Zhejiang University, Hangzhou, Zhejiang, China.

1. F. Jona, D. Westphal, A. Goldmann and P.M. Marcus, *J. Phys. C: Solid State Phys.* **16**, 3001 (1983).
2. P.H. Citrin, D.R. Hamann, L.F. Mattheiss and J.E. Rowe, *Phys. Rev. Lett.* **49**, 1712 (1982).
3. J.F. van der Veen, *Surf. Sci. Rep.* **5**, 199 (1985).
4. D.P. Woodruff, D.L. Seymour, C.F. McConville, C.E. Riley, M.D. Crapper and N.P. Prince, *Phys. Rev. Lett.* **58**, 1460 (1987).
5. J.J. Barton, C.C. Bahr, S.W. Robey, Z. Hussain, E. Umbach and D.A. Shirley, *Phys. Rev.* **B 34,** 3807 (1986).
6. J.J. Barton, C.C. Bahr, Z. Hussain, S.W. Robey, J.G. Tobin, L.E. Klebanoff and D.A. Shirley, Phys. *Rev. Lett.* **51**, 272 (1983).
7. A. Liebsch, Phys. *Rev. Lett.* **32,** 1203 (1974).
8. A. Liebsch, *Phys. Rev.* **B 13,** 544 (1976).
9. S. Kono, C.S. Fadley, N.F.T. Hall and Z. Hussain, *Phys. Rev. Lett.* **41**, 117 (1978).
10. D.P. Woodruff, D. Norman, B.W. Holland, N.V. Smith, H.H. Farrell and M.M. Traum, *Phys. Rev. Lett.* **41**, 1130 (1978).
11. S.D. Kevan, D.H. Rosenblatt, D.R. Denley, B.-C. Lu and D.A. Shirley, *Phys. Rev. Lett.* **41**, 1505 (1978).
12. S. D. Kevan, D H. Rosenblatt, D.R. Denley, B.-C. Lu and D.A. Shirley, *Phys. Rev.* **B 20**, 4133 (1979).

13. D.H. Rosenblatt, J.G. Tobin, M.G. Mason, R.F. Davis, S.D. Kevan, D.A. Shirley, C.H. Li and S.Y. Tong, *Phys. Rev.* **B 23**, 3828 (1981).

14. J.J. Barton, S.W. Robey and D.A. Shirley, *Phys. Rev.* **B 34**, 778 (1986).

15. L.J. Terminello, X.S. Zhang, Z.Q. Huang, S.Kim, A.E. Schach von Wittenau, K.T. Leung and D.A. Shirley, *Phys. Rev.* **B 38,** 3879 (1988).

16. F. Sette, C.T. Chen, J.E. Rowe and P.H. Citrin, *Phys. Rev. Lett.* **59**, 311 (1987).

17. J.R. Patel, D.W. Berreman, F. Sette, P.H. Citrin and J.E. Rowe, *Phys. Rev.* **B 40,** 1330 (1989).

18. Z. Hussain, E. Umbach, D.A. Shirley, J. Stohr and J. Feldhaus, *Nucl. Instrum. Methods* **195**, 115 (1982).

19. S.D. Kevan, Ph.D. thesis, University of California, Berkeley, 1980; LBL-11017.

20. X.S. Zhang, L.J. Terminello, S. Kim, Z.Q. Huang, A E. Schach von Wittenau and D.A. Shirley, *J. Chem. Phys.* **89**, 6538 (1988).

21. M.O. Krause and J.H. Oliver, *J. Phys. Chem. Ref. Data* **8**, 329 (1979).

22. P.A. Lee, P.H. Citrin, P. Eisenberger, and B.M. Kincaid, *Rev. Mod. Phys.* **53,** 769 (1981).

23. C.C. Bahr, J.J. Barton, Z. Hussain, S.W. Robey, J.G. Tobin and D.A. Shirley, *Phys. Rev.* **B 35**, 3773 (1987).

24. P.J. Orders and C.S. Fadley, *Phys. Rev.* **B 27,** 781 (1983).

25. J.B. Pendry, Low Energy Electron Diffraction (Academic, London, 1974).

26. K. Schwarz, *Phys. Rev.* **B 5,** 2466 (1972).

27. S.W. Robey, J.J. Barton, C.C. Bahr, G. Liu and D.A. Shirley, *Phys. Rev.* **B 35,** 1108 (1987).

28. P.R Bevington, Data Reduction and Error Analysis for the Physical Sciences (McGraw-Hill, New York, 1969), Chap. 11.

29. H.L. Davis and J.R. Noonan, *J. Vac. Sci. Technol.* **20**, 842 (1981).

30. J.R. Noonan and H.L. Davis, *Bull. Am. Phys. Soc.* **27**, 237 (1982).

31. J.F. van der Veen and M.A. Van Hove, *Structure of Surfaces*, **2** (Springer, Heidelberg, 1988).

32. A.E. Schach von Wittenau, L.Q. Wang, Z.G. Ji, Z.Q. Huang, T. Shulman and D.A. Shirley ( in preparation).

33. W. Oed, H. Lindner, U. Starke, K. Heinz, K. Muller and J.B Pendry, *Surf. Sci.* **224**, 179 (1989).

Table I. Summary of the structural results (in Å) determined from MSSW analysis and comparisons with the LEED and SEXAFS results. The statistical errors associated with each parameter for the four data sets are given in parentheses (see Sec. 2.3.3.3). The structural parameter values in the upper panel are derived directly from fits of the data, while those in the lower panel were derived by subtracting two corresponding values above the line.

| Parameter | $[001]_{110k}$ | $[001]_{300k}$ | $[011]_{110k}$ | $[011]_{300k}$ | Avg[a] (stat) | Avg[b] (scat) | This[c] work | LEED | SEXAFS |
|---|---|---|---|---|---|---|---|---|---|
| ClCu1 | 1.605(13) | 1.612(14) | 1.604(8) | 1.601(9) | 1.604(5) | 1.606(4) | 1.604(5) | 1.60(3) | 1.53(2) |
| ClCu2a | 3.451(8) | 3.459(10) | 3.441(25) | 3.431(36) | 3.453(6) | 3.446(11) | 3.453(11) | | |
| ClCu2o | 3.413(19) | 3.432(25) | 3.390(30) | 3.378(58) | 3.412(13) | 3.403(21) | 3.412(21) | | |
| ClCu3 | 5.223(13) | 5.237(23) | 5.186(34) | 5.178(81) | 5.222(11) | 5.206(25) | 5.222(25) | | |
| ClCu4 | 7.023(22) | | | | 7.023(22) | 7.023(22) | 7.023(22) | | |
| Cl-Cu | | | | | 2.416(3) | 2.418(3) | 2.416(3) | 2.41(2) | 2.37(2) |
| Cu1Cu2a | | | | | 1.849(8) | 1.840(12) | 1.849(12) | 1.85(3) | 1.90(2) |
| Cu1Cu2o | | | | | 1.808(14) | 1.797(21) | 1.808(21) | 1.85(3) | 1.90(2) |
| Cu2aCu3 | | | | | 1.769(13) | 1.760(27) | 1.769(27) | | |
| Cu2oCu3 | | | | | 1.810(17) | 1.803(33) | 1.810(33) | | |
| Cu3Cu4 | | | | | 1.801(25) | 1.817(33) | 1.801(33) | | |

a) Statistical errors only: Standard deviation. b) Standard deviation from the scatter of results.

c) Final adopted values, with standard deviation taken as the higher of a and b above. Not included in these values and error estimate are any possible offset due to (unknown) systematic error.

# Figure Captions

FIG. 1. A side view of the c(2×2)Cl/Cu(001) structure with the experimental geometries. The emission directions are labelled as [001] and [011], while the photon polarization vectors associated with each geometry are labelled as $\hat{\varepsilon}_{[001]}$ and $\hat{\varepsilon}_{[011]}$, respectively. The larger circles represent the copper atoms. The open circles are in the same plane as the Cl atoms, while the shaded circles lie in planes above and below the paper.

FIG. 2. Experimental $\chi(E)$ curves for the [001] geometry. The curve with solid dots is $\chi(k)$ at 300 K, and the heavier curve is $\chi(k)$ at 110 K.

FIG. 3. Experimental $\chi(E)$ curves for the [011] geometry at two temperatures, as in Fig. 2.

FIG. 4. Fourier spectra for the [001] geometry at two temperatures, 110 K and 300 K, respectively. Each numbered peak is associated with a scattering path-length difference for a numbered atom in the inset.

FIG. 5. Fourier spectra for the [011] geometry at two temperatures, 110 K and 300 K, respectively. Each numbered peak is associated with a scattering path-length difference for a numbered atom in the inset.

FIG. 6. Adsorption site determination for the [001] geometry at two temperatures. The experimental curves (solid lines) are compared to the MSSW calculated curves (dashed lines) for three unreconstructed adsorption geometries (atop, bridge, and four-fold hollow). The experimental data most closely resemble the four-fold hollow calculations at both temperatures.

FIG. 7. Adsorption site determination for the [011] geometry at two temperatures. The notation is similar to Fig. 6. The experimental data most closely resemble the four-fold hollow calculations at both temperatures.

FIG. 8. R-factor contours of Cl-Cu(1) vs. Cl-Cu(2a) for the [001] and [011] geometries at 110 K. For each contour, all the other parameters are kept at their optimum values. The minimum value of the R-factor is 0.11 for the [001] geometry and 0.07 for the [011] geometry. The inner most contour line corresponds to an R-factor of 0.20 for the [001] geometry and 0.10 for the [011] geometry. The contour interval is 0.10. The position of the R-factor minimum is marked by "+", where the size of this mark represents the statistical error for each parameter (see Section 2.3.3.3).

FIG. 9. R-factor contours of Cl-Cu(2a) vs. Cl-Cu(2o) for the [001] and [011] geometries at 110 K, as in FIG. 8. The minimum value of the R-factor is 0.11 for the [001] geometry and 0.07 for the [011] geometry. The contour interval between solid curves is 0.10.

FIG. 10. Illustration of ARPEFS path-length sensitivity beyond 10 Å The 20 Å calculated curve models the high frequency structure of the data very well, while the 10 Å and 13 Å curves do not.

FIG. 11. R-factor contours of Cl-Cu(2o) vs. Cl-Cu(3) for the [001] geometry at 110 K. The minimum value of the R-factor is 0.11 with a contour interval of 0.05, and the inner most contour line corresponds to R = 0.15.

FIG. 12. R-factor contour of Cl-Cu(3) vs. Cl-Cu(4) for the [001] geometry at 110 K, similar to Fig. 11.

FIG. 13. The best fits of the MSSW calculations (dashed curves) to the filtered (16.5 Å) ARPEFS data (solid curves) for the [001] geometry at two temperatures, 110 K and 300 K.

FIG. 14. The best fits of the MSSW calculations (dashed curves) to the filtered (16.5 Å) ARPEFS data (solid curves) for the [011] geometry at two temperatures, 110 K and 300 K.

FIG. 15. Top and side views of the c(2×2)Cl/Cu(001) structure. The side view (lower panel) corresponds to a cut in the plane shown the broken line in the top view (upper panel), while D1, D2o, D2a and D3 represent the perpendicular distances of Cl-Cu(1), Cl-Cu(2o), Cl-Cu(2a) and Cl-Cu(3), respectively, as described in the text.

FIG. 16. Comparisons of the filtered (16.5 Å) ARPEFS data (solid curves) to the MSSW calculations (dashed curves) for the [001] and [011] geometries at 110 K. The MSSW curves are calculated with a Cl-Cu(1) distance of 1.53 Å as obtained from a previous SEXAFS study, while all the other parameters are kept fixed at their optimum values.

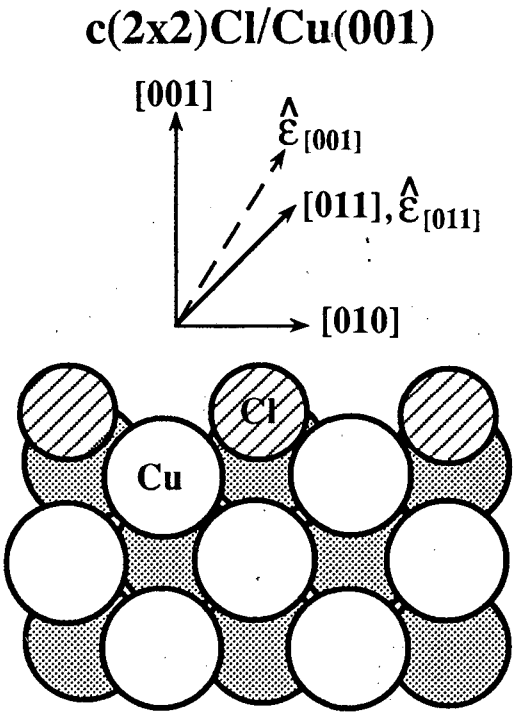
c(2x2)Cl/Cu(001)
[001]
$\hat{\varepsilon}_{[001]}$
[011], $\hat{\varepsilon}_{[011]}$
[010]
Cl
Cu

Figure 1

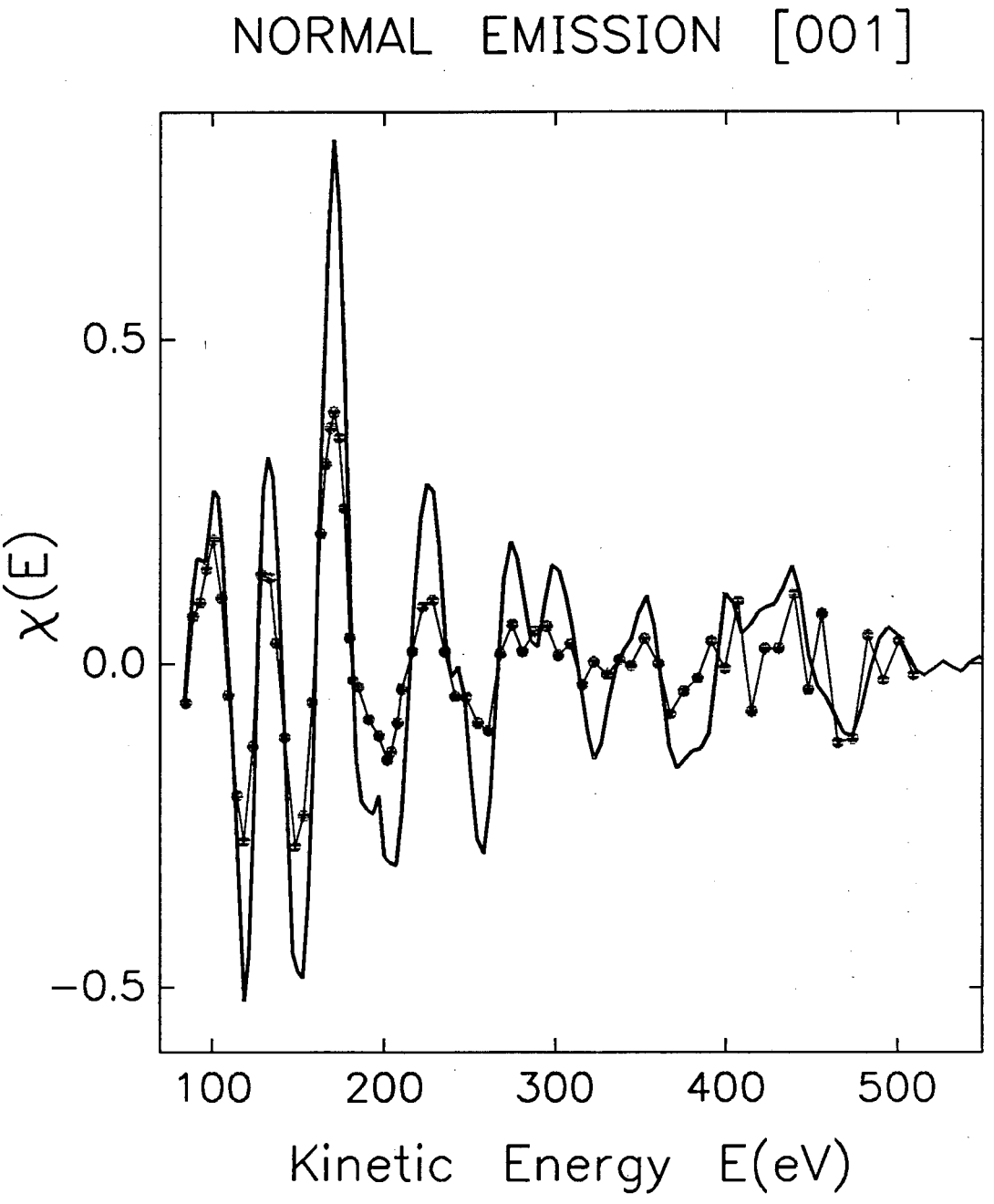
NORMAL EMISSION [001]
0.5
0.0
−0.5
χ(E)
100
200
300
400
500
Kinetic Energy E(eV)

Figure 2

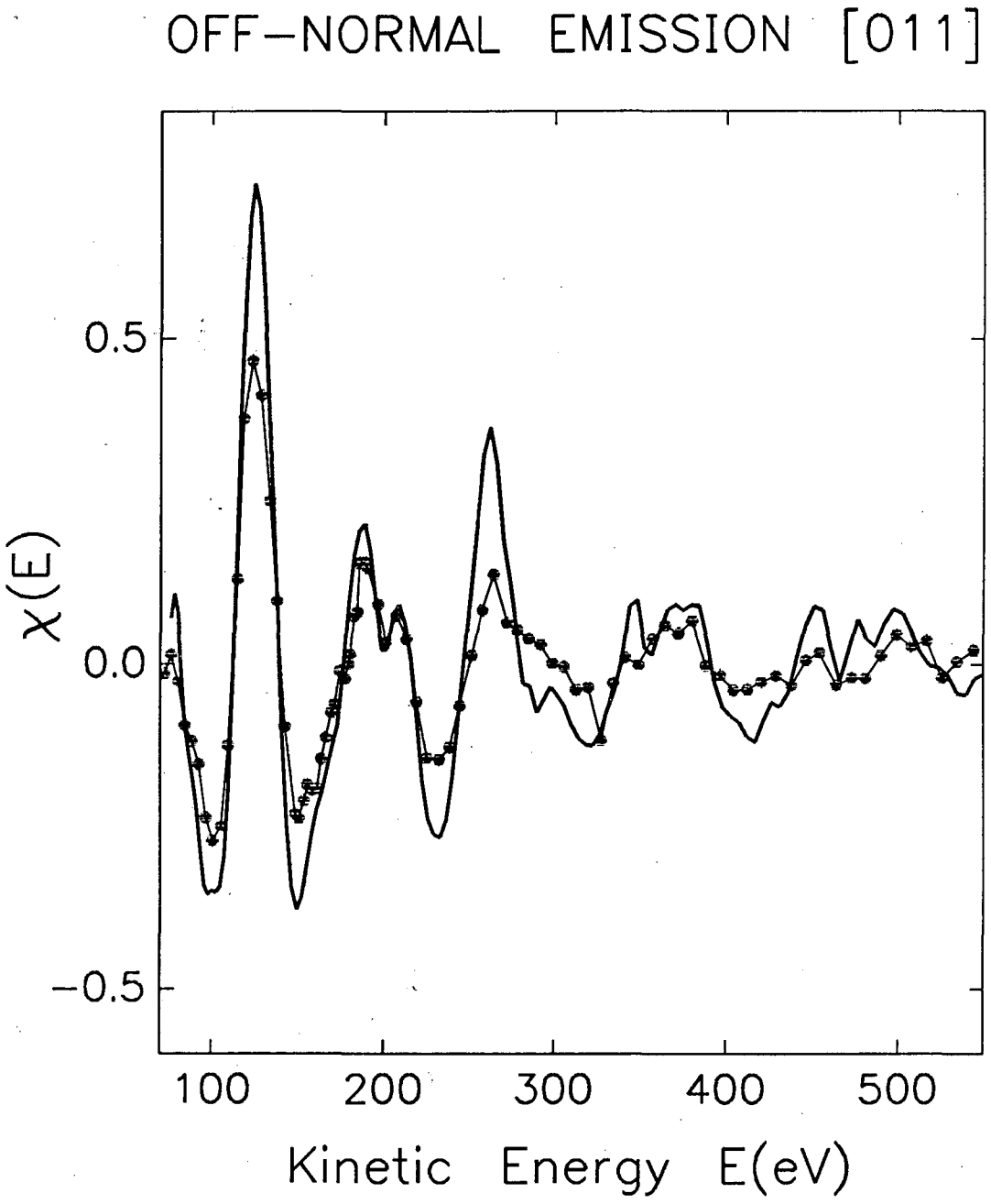
OFF–NORMAL EMISSION [011]
0.5
0.0
−0.5
χ(E)
100
200
300
400
500
Kinetic Energy E(eV)

Figure 3

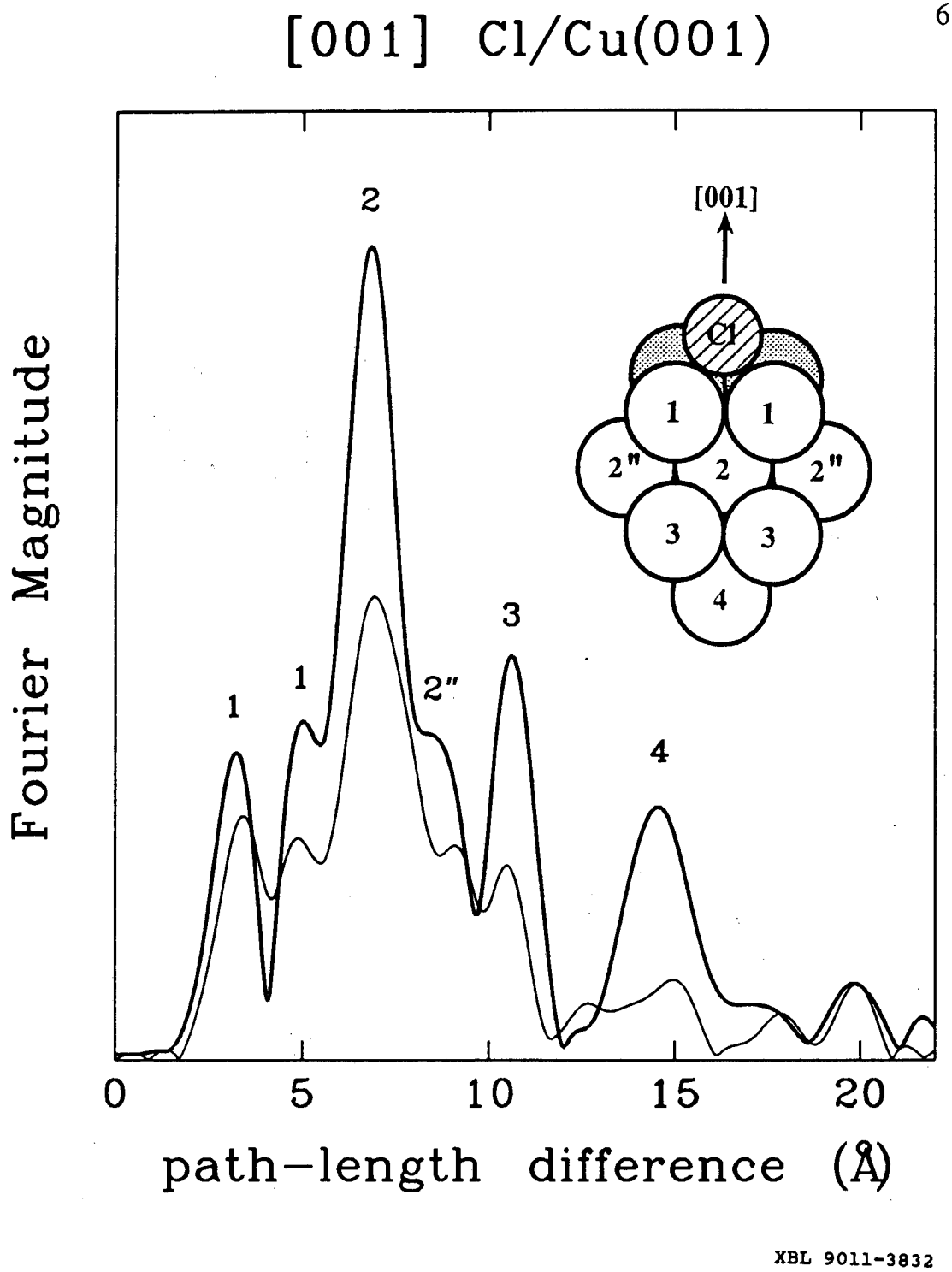
[001] Cl/Cu(001)
Fourier Magnitude
path-length difference (Å)
0
5
10
15
20
1
1
2
2"
3
4
[001]
Cl
1
1
2"
2
2"
3
3
4
XBL 9011-3832

Figure 4

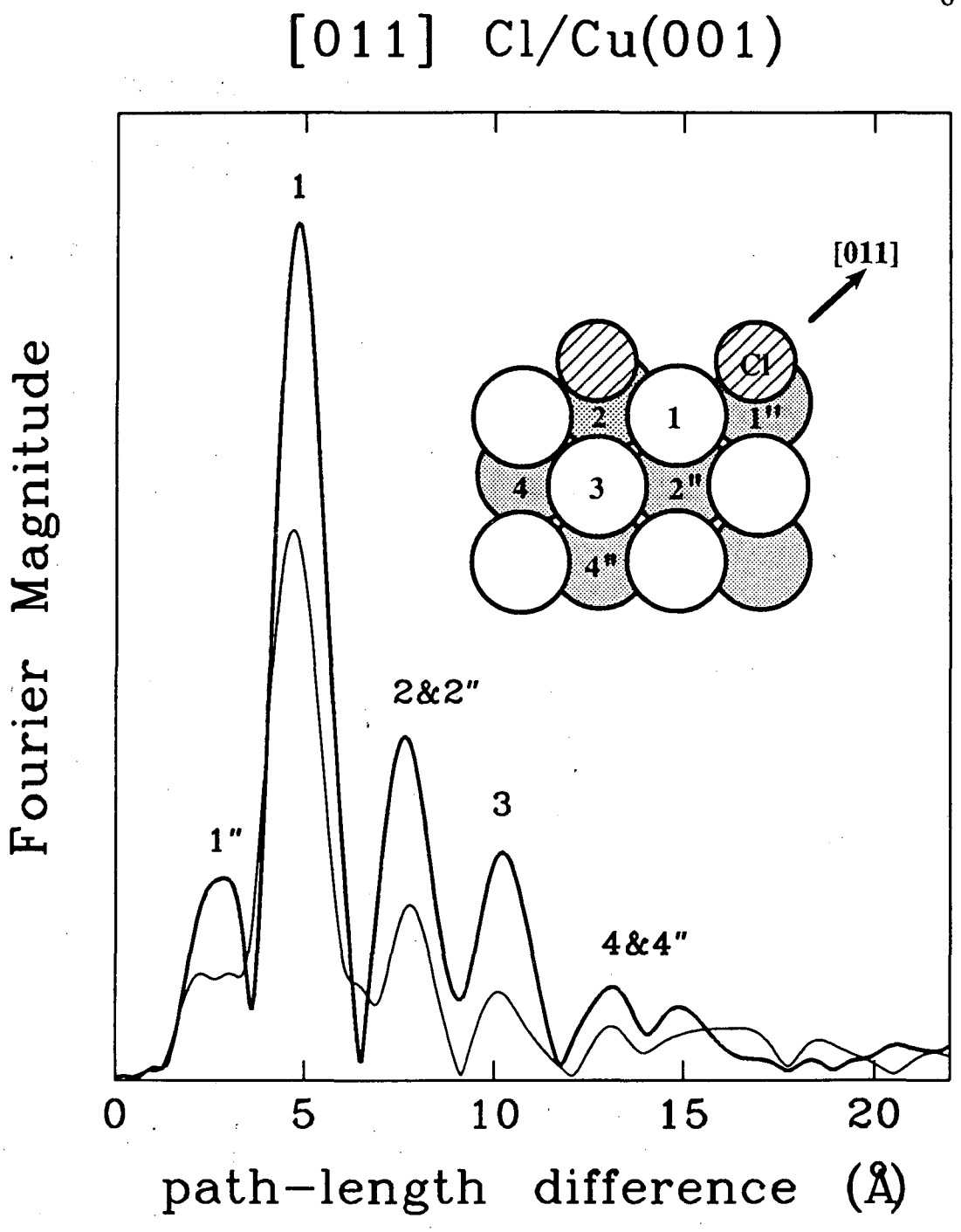
[011] Cl/Cu(001)
Fourier Magnitude
path-length difference (Å)
0
5
10
15
20
1
1"
2&2"
3
4&4"
[011]
Cl
2
1
1"
4
3
2"
4"
XBL 9011-3833

Figure 5

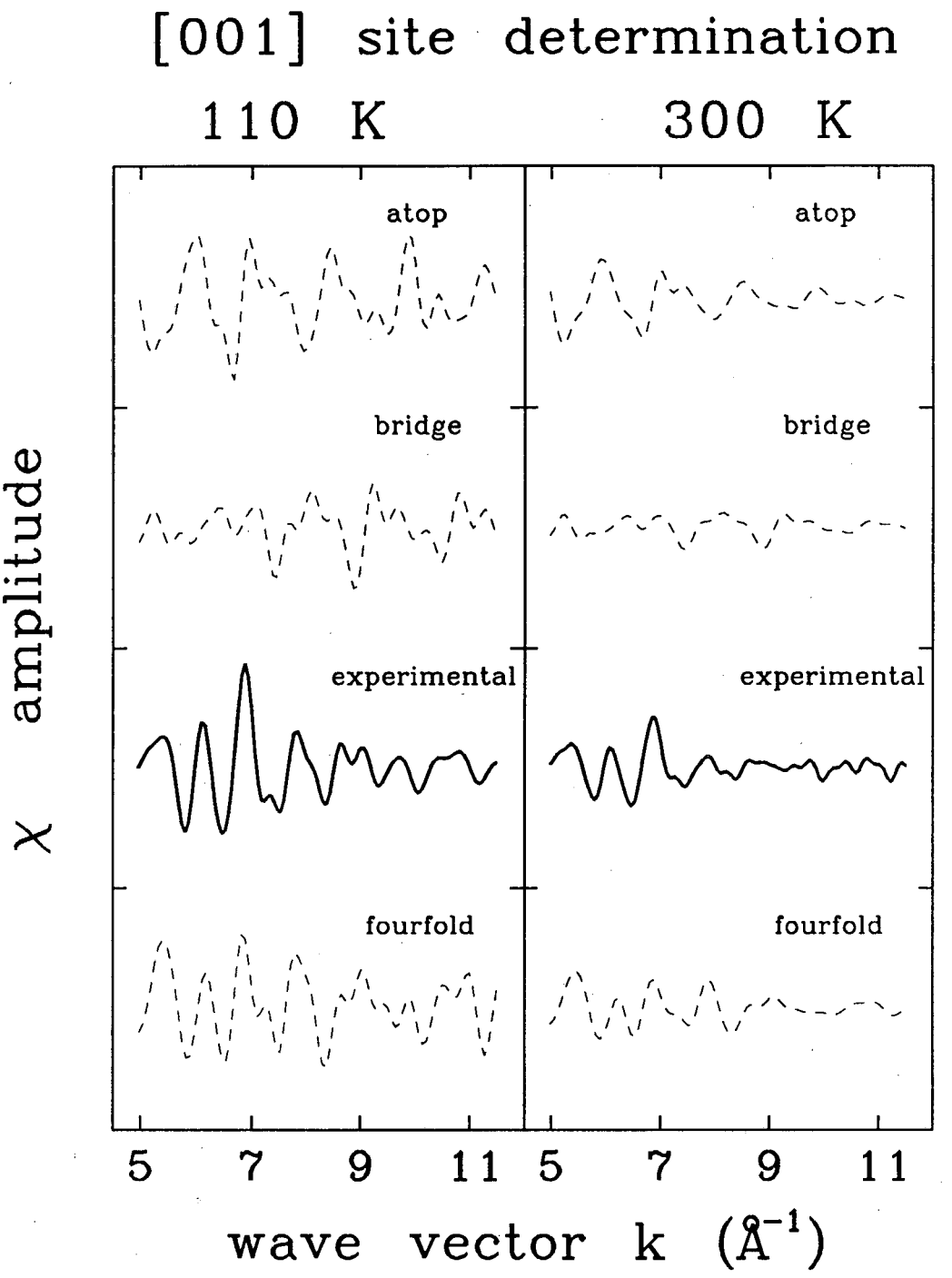
[001] site determination
110 K
300 K
atop
atop
bridge
bridge
experimental
experimental
fourfold
fourfold
χ amplitude
5
7
9
11
5
7
9
11
wave vector k (Å$^{-1}$)

Figure 6

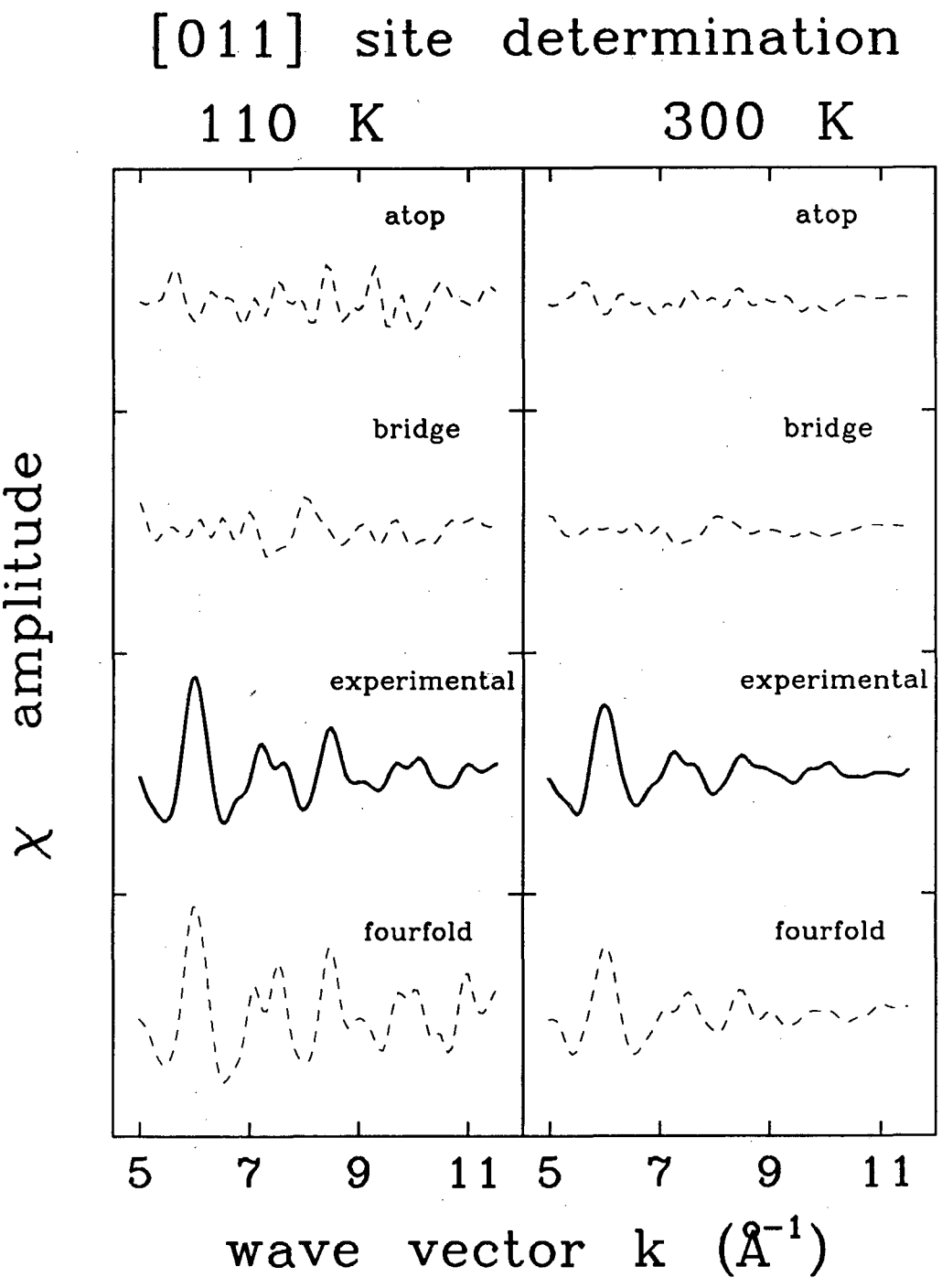
[011] site determination
110 K
300 K
atop
atop
bridge
bridge
experimental
experimental
fourfold
fourfold
χ amplitude
5
7
9
11
5
7
9
11
wave vector k (Å$^{-1}$)

Figure 7

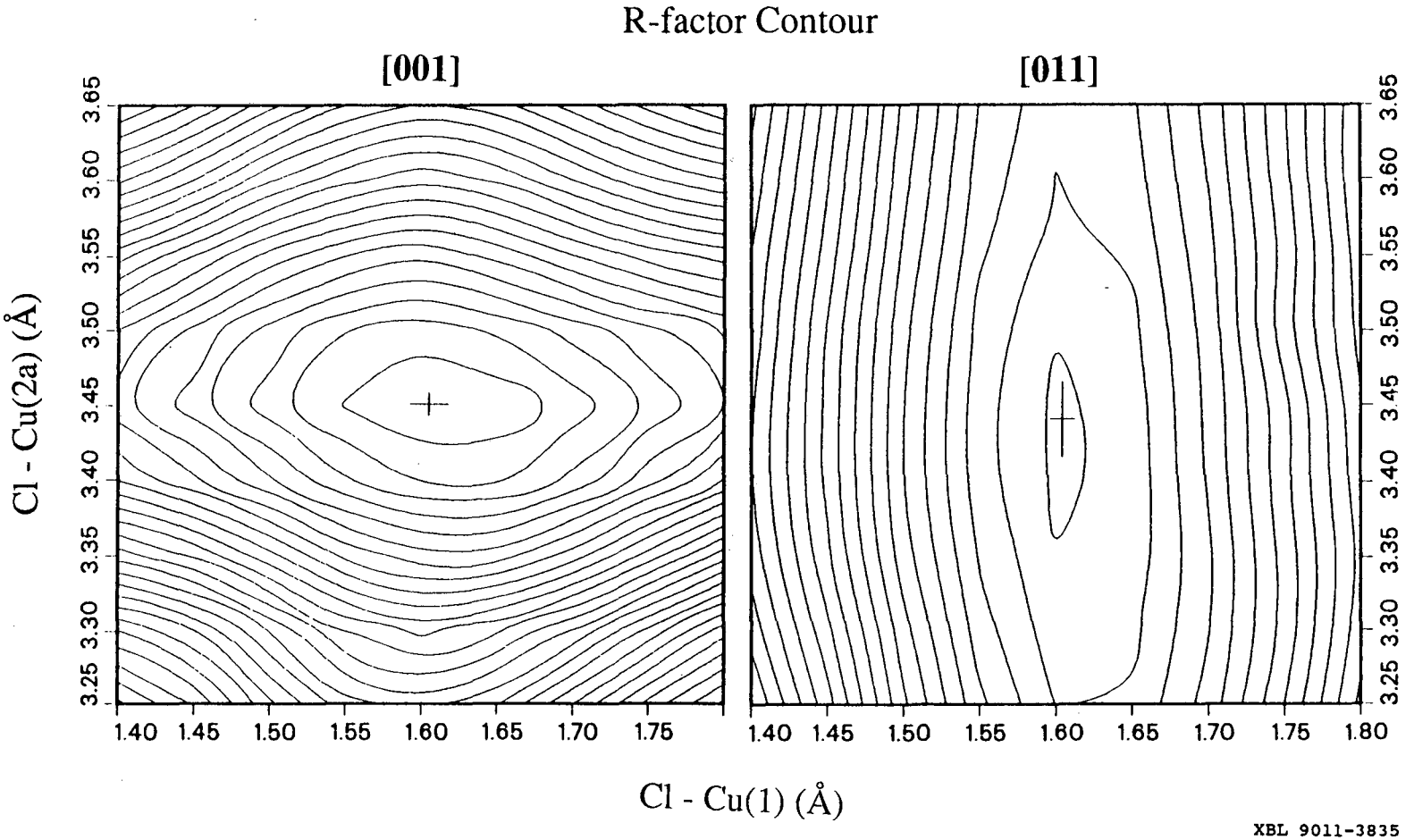
R-factor Contour
[001]
[011]
Cl - Cu(2a) (Å)
Cl - Cu(1) (Å)
3.25 3.30 3.35 3.40 3.45 3.50 3.55 3.60 3.65
1.40 1.45 1.50 1.55 1.60 1.65 1.70 1.75 1.80
XBL 9011-3835

Figure 8

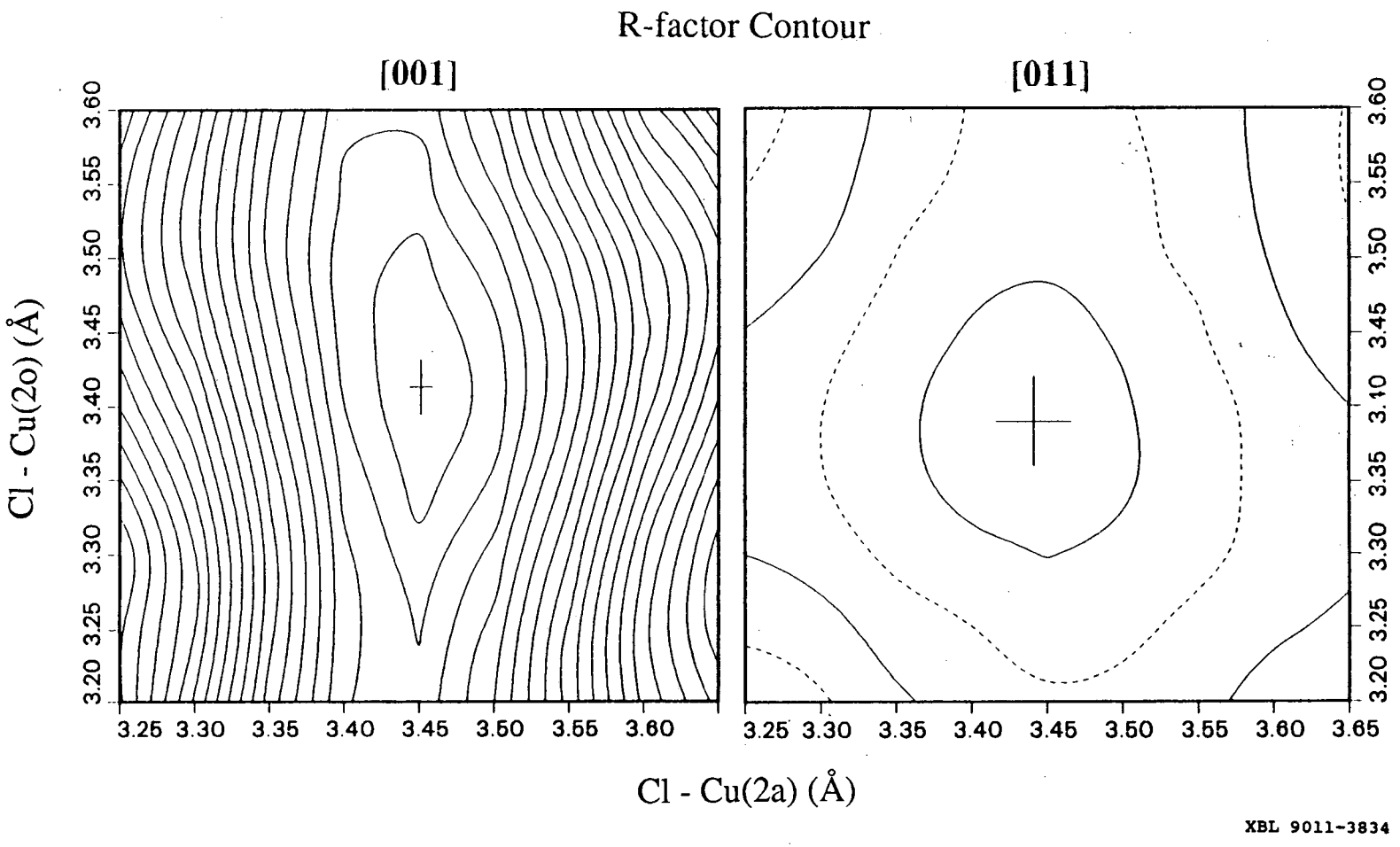
R-factor Contour
[001]
[011]
Cl - Cu(2o) (Å)
Cl - Cu(2a) (Å)
3.20 3.25 3.30 3.35 3.40 3.45 3.50 3.55 3.60
3.25 3.30 3.35 3.40 3.45 3.50 3.55 3.60 3.65
XBL 9011-3834

Figure 9

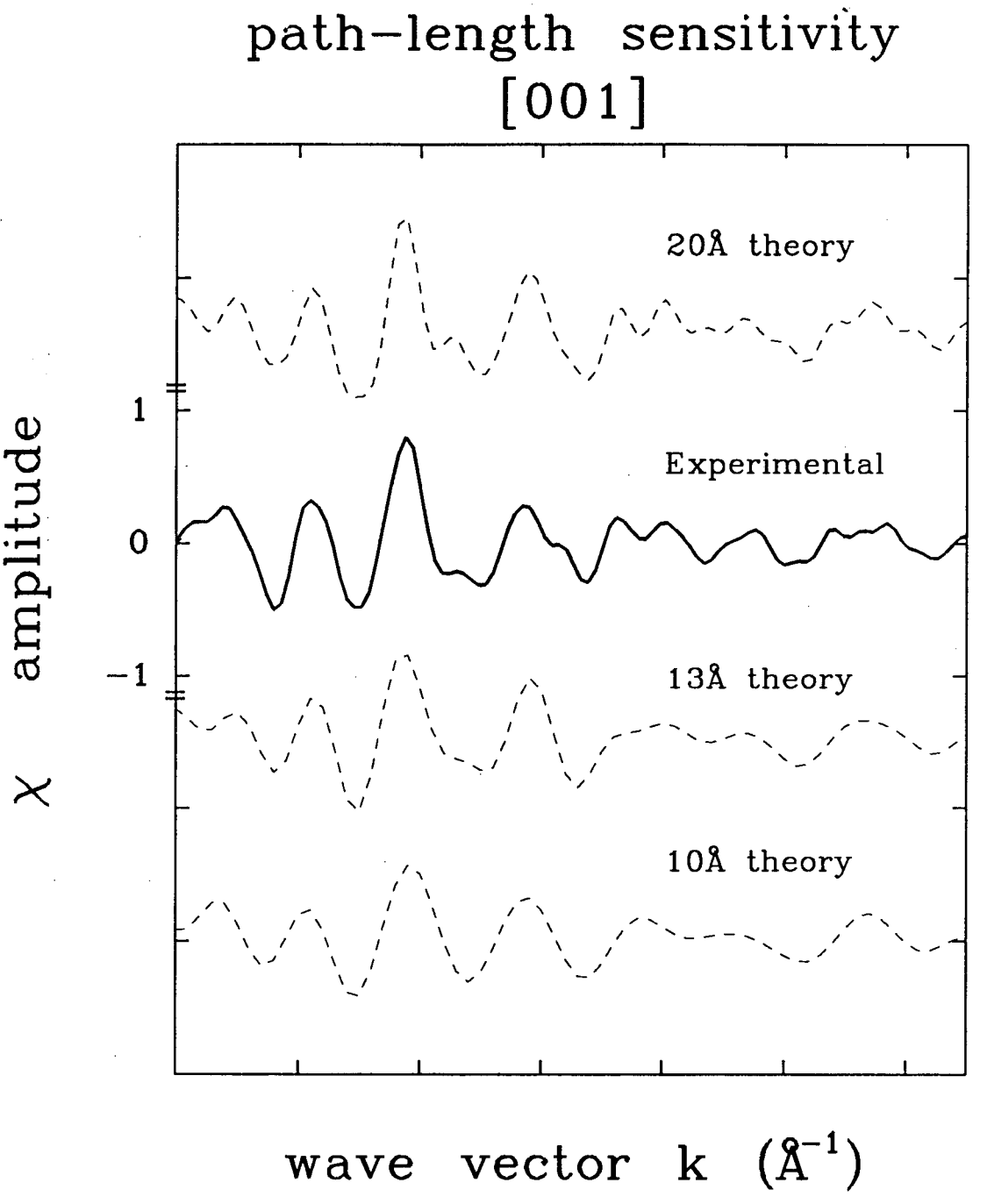
path−length sensitivity
[001]
20Å theory
Experimental
13Å theory
10Å theory
1
0
−1
χ amplitude
wave vector k (Å$^{-1}$)

Figure 10

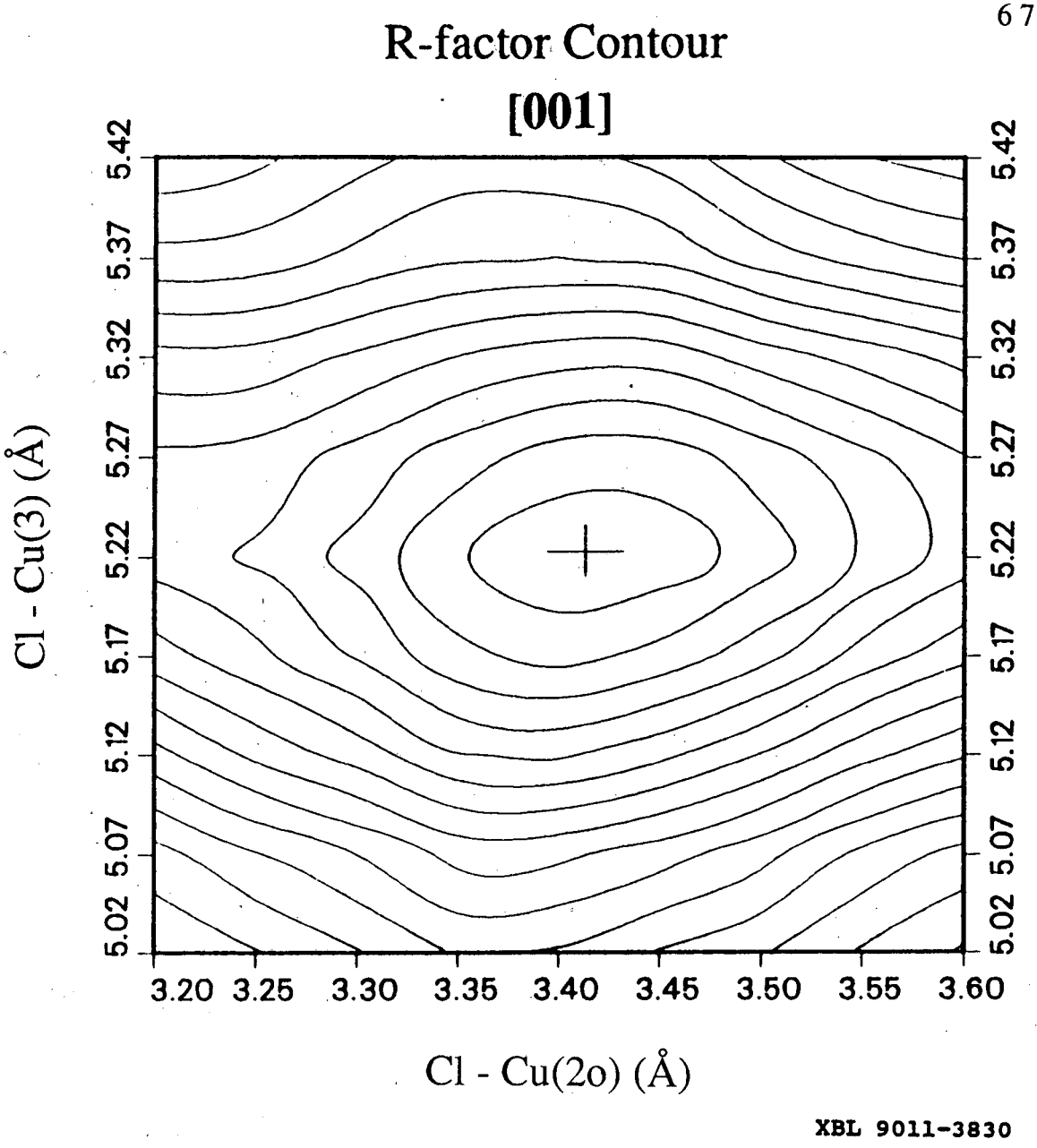
R-factor Contour
[001]
Cl - Cu(3) (Å)
5.02
5.07
5.12
5.17
5.22
5.27
5.32
5.37
5.42
3.20
3.25
3.30
3.35
3.40
3.45
3.50
3.55
3.60
Cl - Cu(2o) (Å)
XBL 9011-3830

Figure 11

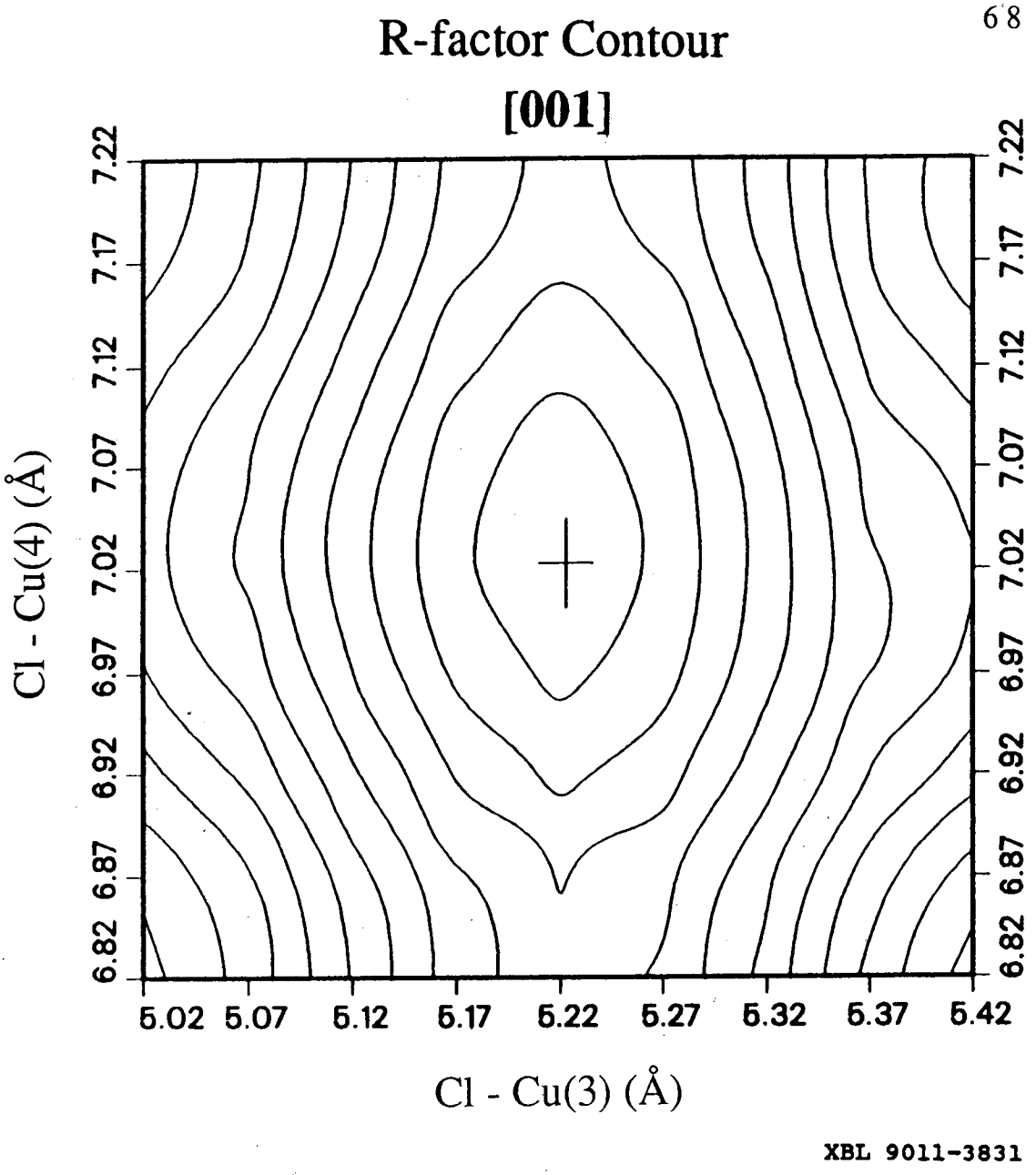
R-factor Contour
[001]
Cl - Cu(4) (Å)
7.22
7.17
7.12
7.07
7.02
6.97
6.92
6.87
6.82
5.02
5.07
5.12
5.17
5.22
5.27
5.32
5.37
5.42
Cl - Cu(3) (Å)
XBL 9011-3831

Figure 12

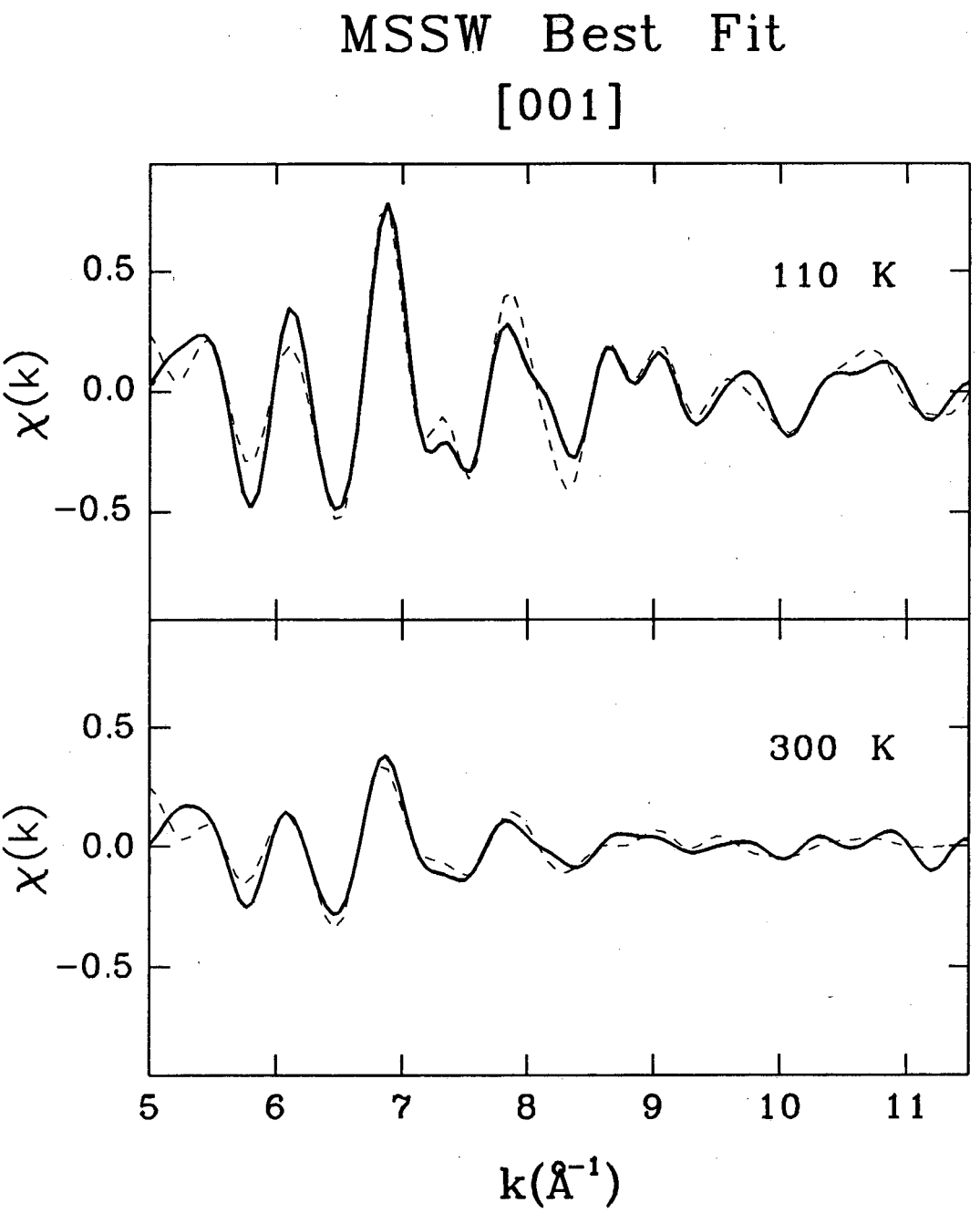


Figure 13

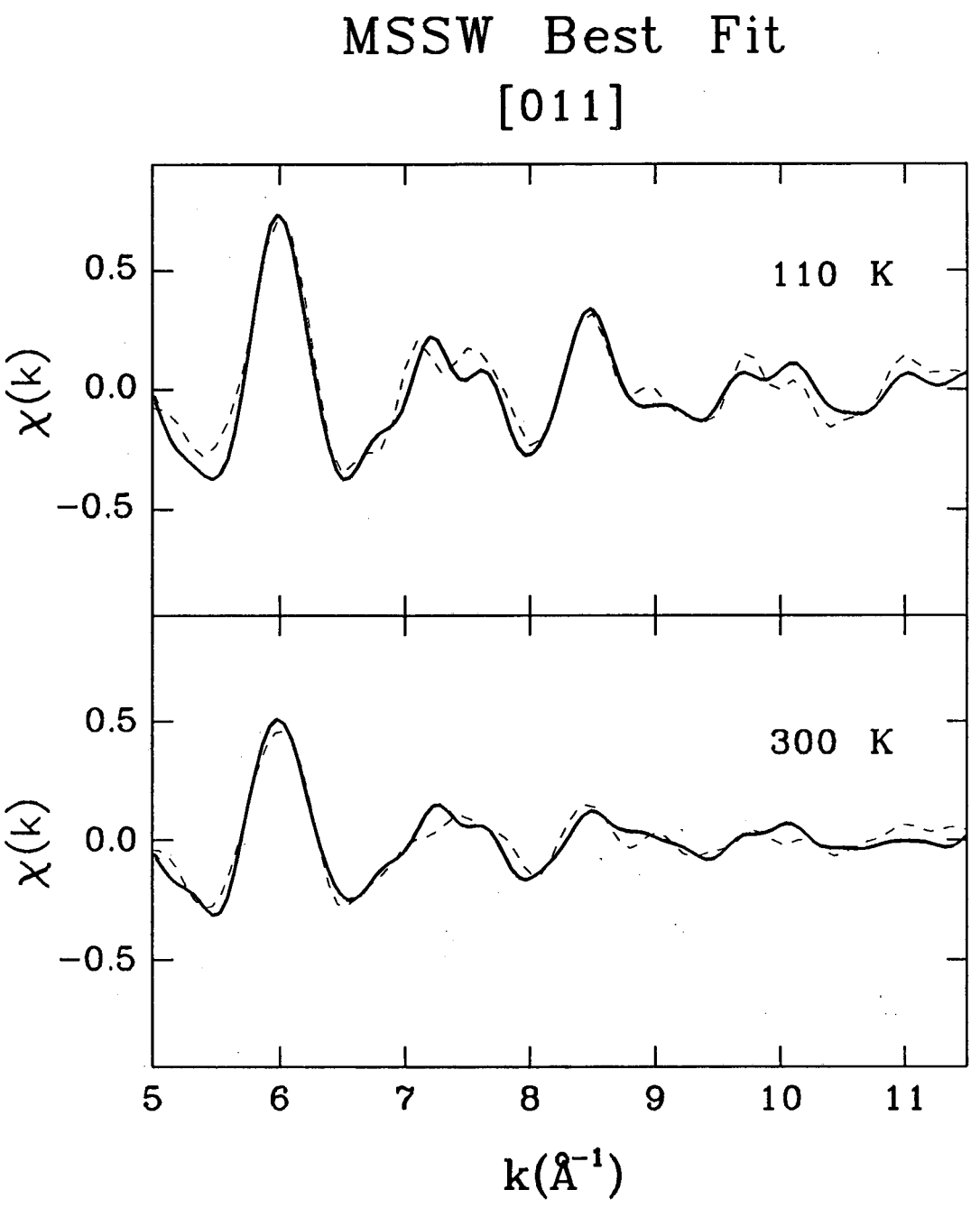


Figure 14

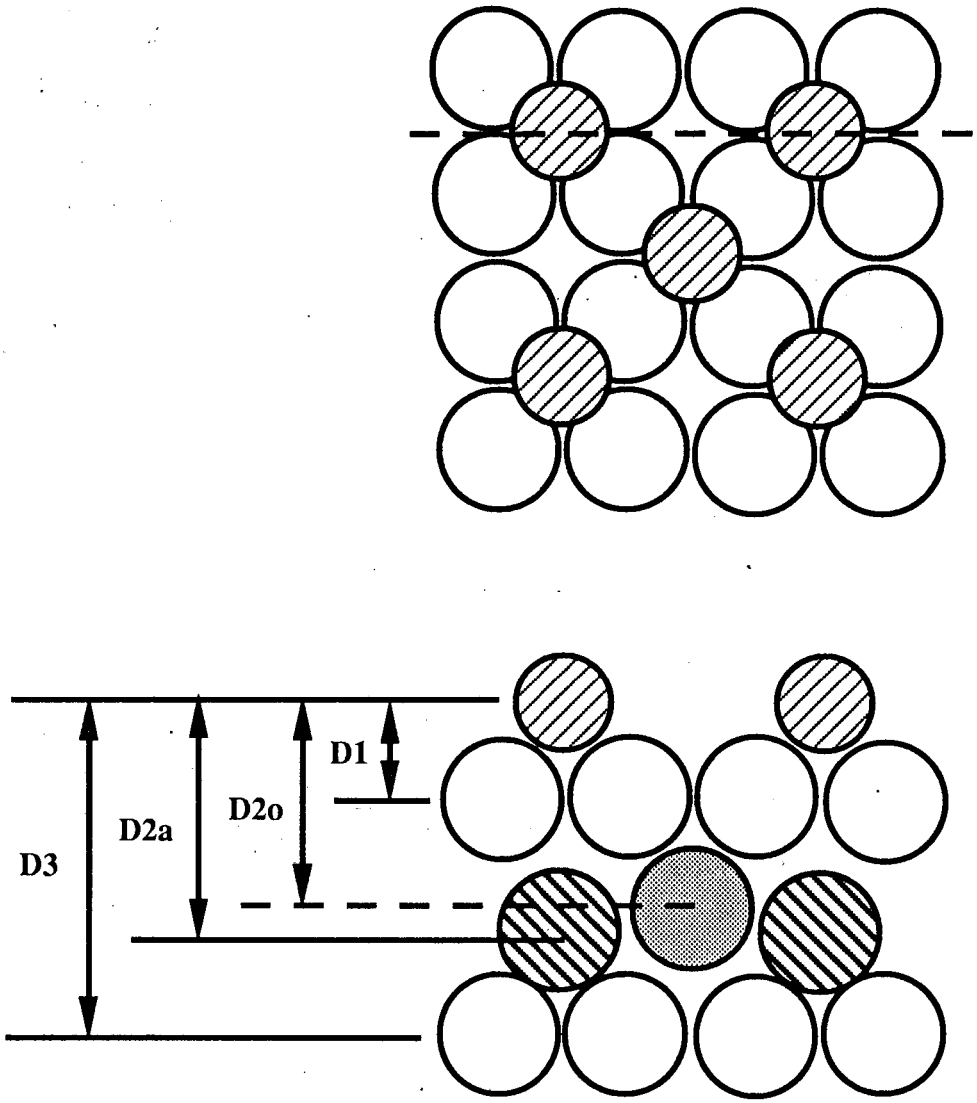


Figure 15

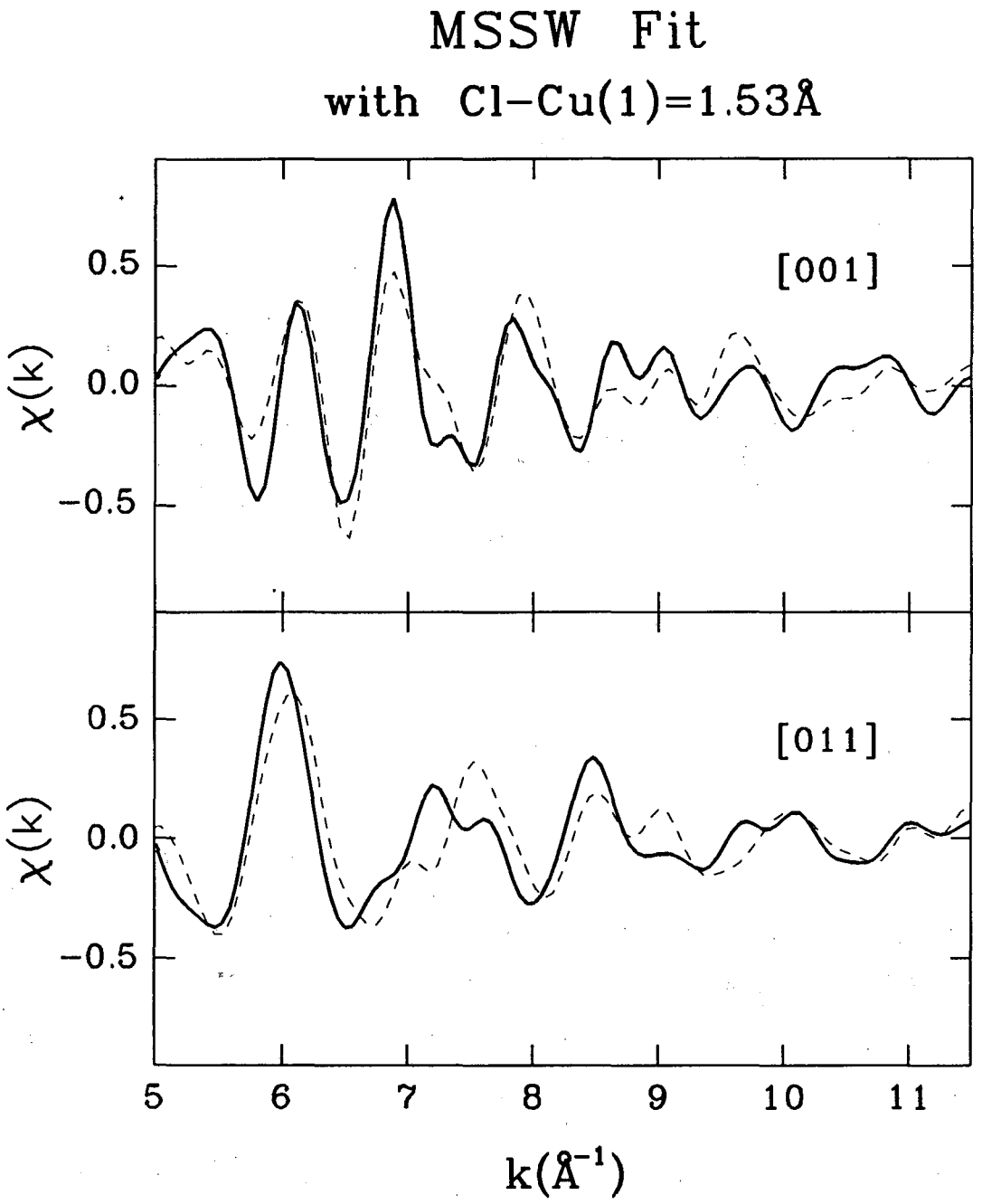


Figure 16

# Chapter 3

# Surface Structure of $\sqrt{3}\times\sqrt{3}$ R30° Cl/Ni(111) Determined Using Low-Temperature ARPEFS

## Abstract

A surface structural study of the $\sqrt{3}\times\sqrt{3}$ R30° Cl/Ni(111) adsorbate system was made using low-temperature angle-resolved photoemission extended fine structure (ARPEFS). The experiments were performed along two emission directions, [111] and [110], and at two temperatures, 120 K and 300 K. The multiple-scattering spherical-wave (MSSW) analysis determined that the Cl atom adsorbs in the fcc three-fold hollow site, 1.837(8) Å above the first nickel layer, with a Cl-Ni bond length of 2.332(6) Å, and an approximate 5% contraction between the first and the second nickel layers (the errors in parentheses are statistical standard deviations only).

# 3.1 Introduction

Adsorbed atoms or molecules frequently cause relaxations of substrate surfaces. However, the understanding of adsorbate-induced substrate surface relaxation requires accurate and detailed surface and near-surface structural information. Angle-resolved photoemission extended fine structure (ARPEFS)[1-5] has proven to be a powerful tool in this regard.

ARPEFS is the angle-resolved and energy-dependent form of photoelectron diffraction due to the final-state interference between the direct and the scattered photoelectron waves.[6] Fourier transformation of the extended fine structure provides direct and qualitative structural information. However, the more quantitative structural analysis requires multiple-scattering spherical-wave (MSSW) theory.[7] With a MSSW level analysis, effects as subtle as small corrugation and relaxation near the substrate surface can be characterized. Because thermal effects (larger mean-square-relative atomic displacements) reduce the amount of structural information present in the fine structure, cooling the lattice effectively extends the range of ARPEFS to deeper layers. Recent studies[5,8] have shown that the adsorbate geometry and the substrate relaxation can be determined more accurately by using low-temperature ARPEFS. In this chapter, we employ low-temperature ARPEFS to study the $\sqrt{3}\times\sqrt{3}$ R30° Cl/Ni(111) system.

There are several published reports of structural studies of halogen atoms on metal surfaces. For example, the c(2×2) Cl/Cu(001) system has been studied by several groups.[5,9-11] However, there are few studies of halogen atoms on fcc (111) surfaces. In SEXAFS study of $\sqrt{3}\times\sqrt{3}$ R30° Cl/Cu(111), D.P. Woodruff et al.[12] were unable to obtain accurate distances beyond the first-nearest neighbors, or to distinguish the two different three-fold hollow adsorption sites of the fcc (111) surface. However, these two

inequivalent hollow sites were distinguished in their photoelectron diffraction study, where only the distance from Cl to the first substrate layer was given. Since ARPEFS has high directional sensitivity, the different substrate atoms can be emphasized by choosing different emission geometries. Thus, ARPEFS can clearly distinguish between two kinds of three-fold adsorption sites. In our study, we use low-temperature ARPEFS to determine the adsorption site as well as to obtain an accurate distance to the second substrate layer for the $\sqrt{3}\times\sqrt{3}$ R30° Cl/Ni(111) system. Interestingly, H. Kuroda et al.[13] recently reported a study of the same Cl/Ni(111) system using combination of SEXAFS and the x-ray standing-wave method. They found that no substrate surface relaxations in the $\sqrt{3}\times\sqrt{3}$ R30° Cl/Ni(111), as opposed to the p(2×2)S/Ni(111)[14] where a significant contraction of 15% was observed with respect to the bulk spacing. Thus, their study offers an opportunity to compare the structural results obtained from different techniques.

This chapter is organized as follows. Section 3.2 gives the experimental details and the procedures of data collection and reduction. Section 3.3 describes two types of analysis: Fourier and multiple-scattering analysis, and present results. Section 3.4 discusses and compares the results. A summary and conclusions are given in section 3.5.

## 3.2 Experimental

The experiments were performed on Beamline X24A[15] at the National Synchrotron Light Source at Brookhaven using a Ge(111) double-crystal monochromator. The Cl 1s photoemission spectra were taken in the kinetic energy range from 50 to 550 eV, with photon energies from 2870 to 3370 eV. The resolution of the double-crystal monochromator was approximately 1 eV through this photon energy range. Data were collected with a rotatable hemispherical electrostatic analyzer[16] which has the energy

resolution of ~ 1 eV FWHM under the operating conditions of 160 eV pass energy, and the angular resolution of the input lens of ± 3°. The experimental chamber was equipped with a four-grid LEED/Auger systems, an ion gun, and an effusive beam doser for introducing chlorine gas.

A nickel single crystal was cut, oriented to within ± 1° of the (111) direction as determined by Laue backscattering, then mechanically polished and chemically etched. Since the fcc (111) crystal lacks two-fold symmetry, it is hard to tell the crystal azimuthal orientation from the p(1×1) LEED pattern. Thus, several Laue pictures were taken at different x-ray incident directions along the fixed crystal axis to define the azimuthal orientation of the crystal. The final finished crystal was attached to a Ta sample plate mounted on a high-precision manipulator with a liquid nitrogen cooling system. Sample heating was accomplished by electron bombardment from a tungsten filament located behind the sample plate. The temperatures were measured by a chromel-alumel thermocouple attached to the sample plate next to the sample. The nickel crystal was cleaned by repeated cycles of $Ar^+$ ion sputtering and annealing to about 880 K. This procedure was sufficient to remove all impurities except carbon. Carbon was then removed by heating the crystal to 770 K after exposure to $1x10^{-8}$ torr of oxygen for several minutes. The crystal was taken as clean when AES showed no detectable traces of carbon, nitrogen, oxygen, or sulfur contamination and a sharp p(1×1) LEED pattern was observed. The chamber pressure was about $3x10^{-10}$ torr during measurements. Because chlorine exposure to a clean Ni(111) surface produces a sequence of LEED patterns with superstructures, and a sharp $\sqrt{3}\times\sqrt{3}$ R30° LEED pattern is stable within a relatively small exposure range corresponding to ~ 0.2 L, the $\sqrt{3}\times\sqrt{3}$ R30° Cl overlayer preparation was done carefully in several steps. A sharp $\sqrt{3}\times\sqrt{3}$ R30° Cl overlayer LEED pattern was produced by dosing $Cl_2$ through an effusive beam doser at room temperature for a total of

4-5 minutes with the main chamber pressure at ~ $1x10^{-9}$ torr. This was followed by a 350 K annealing for two minutes to dissociate $Cl_2$ completely into atomic Cl.

The experiments were carried out along two emission directions, [111] and [110], and at two temperatures, 120 ± 5 K and 300 K. These four sets of ARPEFS data were taken on separately prepared samples. The sample was flashed to about 350 K every 6-9 hrs during data collection, and more often for the low-temperature measurements. The crystal orientation angle for each geometry was determined by a He-Ne laser autocollimation through the experimental chamber viewports with an accuracy of ± 2°. The experimental geometries are shown in Fig. 1. For the normal [111] geometry, photoelectrons were collected along the surface normal with the photon polarization vector 35° from the surface normal toward the [11$\bar{2}$] direction, while for the offnormal [110] geometry, the emission direction and photon polarization vector are co-linear along the [110] direction. These two geometries were chosen to highlight nearby backscattering atoms, utilizing the directional sensitivity of ARPEFS. The [111] geometry can determine interlayer spacings effectively, while the [110] geometry was selected to emphasize the nearest-neighbors along the [110] direction.

For each emission geometry at a given temperature, a series of photoemission spectra was collected over a 50-550 eV kinetic energy range in equal electron wave-number increments of 0.08 $Å^{-1}$. Each photoemission spectrum was centered on the Cl 1s photoelectron peak, with an energy window of 25 - 30 eV. The experimental background consisted of three photoemission scans covering the kinetic energy range of 40-560 eV. Each scan was taken at a different photon energy so that the Cl 1s photoemission peak lay about 10 eV below the lowest kinetic energy in each spectrum. This experimentally measured background was used in the least-square fitting for the normalization of each photoemission spectrum to compensate for the inhomogeneous photon flux and the

electron analyzer transmission function. The photoemission intensity was extracted by least-square fitting of each photoemission spectrum with three functions: a Voigt function to model the core-level photoelectron peak, a Gaussian convoluted with a step function (G step) to describe the inelastically-scattered electrons associated with the photoelectron peak, and an experimentally-measured background to account for other inelastic scattering processes. The detailed procedures have been described previously.[5]

In analogy to EXAFS, the total normalized photoemission intensity I(E) as a function of kinetic energy E is composed of a slowly varying atomic-like portion and a rapidly oscillating contribution due to the interference effects of electron scattering from neighboring ion cores. I(E) can be described as:

$$I(E) = [\chi(E) + 1]\, I_0(E) \quad , \qquad (1)$$

where $I_0(E)$ is a slowly varying atomic-like function and $\chi(E)$ is the oscillatory interference function which can be determined by removing the slowly varying function $I_0(E)$ from the total photoemission intensity I(E):

$$\chi(E) = \frac{I(E) - I_0(E)}{I_0(E)} \quad . \qquad (2)$$

The experimental $\chi(E)$ curves are shown in Fig. 2 for the [111] and [110] data at two temperatures, 120 K and 300 K, respectively. The $I_0(E)$ was fitted with simple low-order polynomials for constructing $\chi(E)$ curves. We can see from Fig. 2 that the oscillation amplitudes of $\chi(E)$ at the lower temperature are enhanced as compared with those at room temperature. The oscillation patterns are matched well at the two temperatures.

For Fourier data analysis, it is necessary to convert $\chi(E)$ to $\chi(k)$. The photoelectron kinetic energy E measured outside the solid is related to the wave-number k of the photoelectron inside the solid by the De Broglie relation:

$$k = \hbar^{-1}\sqrt{2m_e\,(E + V_0)}\ , \qquad (3)$$

where $m_e$ is the electron rest mass and $V_0$ is the inner potential of the solid. The value of $V_0$ is typically about 10 eV, but the exact value is unknown. The $V_0$ is therefore treated as an adjustable parameter in the fits.

## 3.3 Analysis and Results

Structural information can be extracted from the experimental $\chi(k)$ curves in two ways: by Fourier analysis and by multiple-scattering spherical-wave (MSSW) analysis. We first treat the data by Fourier analysis to obtain qualitative structural information such as adsorption site and approximate geometric parameters. MSSW calculations are then required to obtain quantitative structural information.

### 3.3.1 Fourier Analysis

Using the single-scattering model of ARPEFS[6], the expression for $\chi(k)$ can be written as

$$\chi(k) = 2\sum_j \frac{\cos\beta_j}{\cos\gamma}\frac{|f(\theta_j)|}{R_j} e^{-\Delta R_j/\lambda} e^{-\sigma_j^2(1-\cos\theta_j)k^2} \cos[kR_j\,(1-\cos\theta_j) + \phi_j]\ . \qquad (4)$$

The summation is over all atoms near the adsorbed "source" atom from which core-level photoemission originates. Here $\beta_j$ is the angle between the photon polarization vector and the vector connecting the emitting atom and the j th scattering atom, $R_j$ is the distance from the photoemitter to the j th scattering atom, and $\gamma$ is the angle between the emission direction and the photon polarization vector. The k-dependent complex scattering factor

$f(\theta_j)$ for a given scattering angle $\theta_j$ can be divided into the magnitude $|f(\theta_j)|$ and the phase $\phi_j$. The emission-angle dependent path-length difference is given by $\Delta R_j = R_j (1-\cos\theta_j)$. The temperature effect is introduced as a Debye-Waller factor, where $\sigma_j$ is the mean-square relative displacement (MSRD) between the photoemitter and the j th scattering atom, projected on the photoelectron momentum change direction. Inelastic losses due to excitation of plasmons and electron-hole pairs by the energetic photoelectron are incorporated in an electron mean-free path $\lambda$.

The cosinusoidal dependence of the $\chi(k)$ function permits a Fourier transformation, yielding an amplitude spectrum peaked near various scattering path-length differences. Fourier spectra for the [111] and [110] data at the two temperatures are given in Fig. 3. $V_0$ value of 10 eV was used. Forward ($\theta_j = 0°$) and backward ($\theta_j = 180°$) scatterings give the strongest signals: the strong feature at a path-length difference ~ 4.6 Å in the [110] direction arises from a nearest-neighbor Ni atom located directly behind Cl along the [110] direction, at a Cl-Ni bond length of ~ 2.3 Å. Atop and bridge adsorption sites are excluded because they have no backscattering atom along the [110] direction to give the strong peak at ~ 4.6 Å. However, there are two different three-fold hollow adsorption sites, which are called the fcc and hcp sites, respectively. The fcc sites are directly above atoms in the third substrate layer, while the hcp sites are directly above atoms in the second substrate layer. Figure 4 illustrates that one of the nearest-neighbor Ni atoms lies behind the Cl atom along the [110] direction in the fcc site, but not in the hcp site. Therefore, the strong Fourier backscattering peak in the [110] direction indicates that the fcc three-fold hollow site is the one occupied in the $\sqrt{3}\times\sqrt{3}$ R30° Cl/Ni(111) system. Furthermore, the two peaks at ~ 7.6 Å and ~ 9.1 Å in the [110] direction can be attributed mainly to scattering from the atoms in the second Ni(110) plane, while the first peak at ~

2.5 Å in the [110] direction, corresponds to scattering from two nearest-neighboring atoms symmetrically located at either side of the plane containing the [111] and [110] directions.

Fourier spectra in the [111] direction show two peaks at ~ 3.9 Å and ~ 7.8 Å. The first peak is due to scattering from the three nearest-neighboring atoms in the first Ni layer, while the second peak corresponds to scattering from the three third-nearest neighbor atoms in the second Ni layer. Thus, the normal emission data suggest that we can determine the distance of Cl to both the first and second Ni layers, providing information about the substrate surface relaxation.

### 3.3.2 Multiple-Scattering Analysis

ARPEFS studies[1-5] have shown that the detailed quantitative geometric structures can be obtained by comparing experimental $\chi(k)$ curves with theoretical calculations based on multiple-scattering spherical-wave (MSSW) theory[7], which comprehensively describes the ARPEFS scattering process. The MSSW calculation requires as input both structural and non-structural parameters. The copper and chlorine phase shifts were available from previous calculations.[5,17-18] The mean free path was included in an exponential factor, $e^{-r/\lambda}$, with $\lambda = ck$ and $c = 0.75$. Thermal effects were treated using a correlated Debye model which included surface-layer dependent and anisotropic mean-square relative displacements (MSRD).[7] The nickel bulk Debye temperature was taken as 390 K, while the nickel surface Debye temperature was set to 276 K, which assumes that the surface nickel atoms have an MSRD twice as that of the bulk. The Debye temperature for the Cl overlayer was estimated to be 355 K from the nickel surface Debye temperature adjusted for the difference in masses. Surface Debye temperatures for both Cl and Ni were, however, varied in the calculations based on the above estimated values. In addition, the

emission and polarization angles (± 3°), the experimental temperature (120 ± 10 K) and the inner potential (10 ± 5 eV) were allowed to vary in the calculations.

First, both the [111] and the [110] experimental $\chi(k)$ curves at the two temperatures were smoothed by Fourier filtering out the high-frequency portion of the data (path-length differences larger than 10.0 Å). Thus, the cutoff at about 10.0 Å eliminates high-frequency noise and retains all the real signals from down to the second substrate layer. Also, the cutoffs below 1.8-2.0 Å were made due to uncertainties of the low frequency portion of the data. All subsequent comparisons of theory with experiment were done with the filtered data, 2.0-10.0 Å for the [111] data, and 1.8-10.0 Å for the [110] data. The MSSW calculations were performed with the same path-length difference cutoffs.

The fcc three-fold adsorption site had already been determined for the $\sqrt{3}\times\sqrt{3}$ R30° Cl/Ni(111) system from the Fourier analysis above. Comparisons of the MSSW calculations with the experimental data confirm this result. The $\chi(k)$ curves for two different three-fold adsorption geometries (fcc and hcp) were calculated using the bulk Ni spacing (2.03 Å) with a Cl-Ni bond length of 2.3 Å estimated form the Fourier analysis. Figure 5 shows the comparison of the calculated $\chi(k)$ curves with the experimental data for the [111] and [110] directions at 120 K, respectively. By visual inspection, the calculated curve in the [110] direction for the fcc site unambiguously resembles the experimental data more than that for the hcp site, while in the [111] direction, it is not clear which calculated $\chi(k)$ curve more closely resembles the experimental data. Since there is a backscattering atom near the photoemitter for the fcc site, but not for the hcp site in the [110] direction, the calculated $\chi(k)$ curve for the hcp site has rather different features and weaker amplitude as compared with that for the fcc site. Thus, MSSW calculations provide strong evidence to support the fcc three-fold site, consistent with the Fourier analysis. However, there are

still large differences between the experimental $\chi(k)$ curve and the calculations for the fcc site using nonoptimized geometrical parameters. This suggests possible substrate surface relaxation in the $\sqrt{3}\times\sqrt{3}$ R30° Cl/Ni(111) system.

To derive a detailed quantitative structure, we optimized both structural and nonstructural parameters to achieve the best agreement between the theory and the experiment. An R-factor (reliability-factor) was used as a quantitative measure of the fit between the experiment and the theory. The optimum geometrical parameters were obtained when a minimal R-factor defined by

$$R = \frac{\int[\chi_E(k) - \chi_T(k)]^2 dk}{\int\chi_T(k)^2 dk}, \qquad (5)$$

was reached. Here E and T denote experiment and theory. The R-factors were calculated over the k range 5.2-11.2 $Å^{-1}$.

In recent ARPEFS studies,[5,8] an automatic routine was successfully used to search many parameters simultaneously with a reasonable number of iterations. The detailed procedure of this routine has been described previously. No lateral substrate relaxation and no corrugation of the second substrate layer were considered because of the $\sqrt{3}\times\sqrt{3}$ R30° structure of the Cl/Ni(111) system. The experimental data were fitted with two structural parameters: Cl-Ni(1), the vertical distance of Cl to first Ni layer, and Cl-Ni(2), the vertical distance of Cl to second Ni layer, while other nonstructural parameters such as electron emission angles, adsorbate and substrate surface Debye temperatures, the experimental temperature, and the inner potential were treated as adjustable parameters with reasonable initial guesses and bounds. The emission angles were found to be < 3° from the expected values for all the data sets. The inner potential for the optimum

geometry was $10 \pm 2$ eV, and the experimental temperature was optimized to be $120 \pm 5$ K. R-factor minima lay in the small range R = 0.05 - 0.13 in the various calculations.

The structural parameters determined from the best fits are listed in Table I, with statistical errors in parentheses. The error associated with each parameter was estimated as described in our previous study.[5] The best fits of the MSSW calculations to the filtered (10.0Å) experimental $\chi(k)$ curves are shown in Figs. 6 and 7 for the [111] and [110] geometries at the two temperatures, respectively. Agreements between the theoretical and experimental curves are excellent. From Table I, we can see that the structural parameters obtained from the four data sets were consistent, especially for the data at different temperatures with a given geometry. There are larger errors for the Cl-Ni(2) parameter in the [110] direction than those in the [111] direction, showing different sensitivity of a given data set to each structural parameter due to the directional sensitivity of ARPEFS.

Figure 8 shows R-factor plots for the [111] and the [110] geometries at the two temperatures, calculated by varying the Cl-Ni(1) and Cl-Ni(2) distances, respectively, while other parameters were fixed in their optimum values. The R-factor curvature for the Cl-Ni(2) distance in the [111] direction is steeper than that in the [110] direction, giving smaller error bars for the Cl-Ni(2) distance in the [111] geometry. Moreover, the R-factor minima were smaller for a given geometry at the lower temperature, due to the increased signal to noise ratio. The interlayer spacing between the first and the second Ni layers can thus be determined more accurately from the analysis of the low-temperature [111] data.

The top and side views of the $\sqrt{3}\times\sqrt{3}$ R30° Cl/Ni(111) structure are shown in Fig. 4. From Table I, the Cl-Ni(1) distance of 1.837(8) Å gives a Cl-Ni bond length of 2.332(6) Å. The Cl-Ni(2) distance of 3.763(7) Å then yields interlayer spacing between the the first and the second Ni layers Ni(1)-Ni(2) of 1.926(11) Å, showing an approximate 5 % contraction from the bulk value of 2.03 Å.

## 3.4 Discussion

The vertical distance of Cl to the first Ni layer Cl-Ni(1) of 1.837(8) Å obtained from this study is 0.08 Å smaller than the recent SEXAFS study[13] by Kuroda et al. This difference is beyond the standard error of each of the two techniques. However, studies on the p(2×2)S/Ni(111) system using several different techniques also showed rather different results for the vertical distance of S to the first Ni layer S-Ni(1), ranging from 1.40 to 1.66 Å.[14,19-22] For example, a SEXAFS study[14] by the same group gave the S-Ni(1) distance as 1.66 Å, while a LEED study[19] by Mitchell et al. showed a distance of 1.50 Å, a 0.16 Å difference. Furthermore, a recent low-temperature ARPEFS study[8] on the same system found the S-Ni(1) distance of 1.54 Å, which is closer to the LEED study. We can see that the distances of adsorbate to the first substrate layer from SEXAFS studies on both p(2×2)S/Ni(111) and $\sqrt{3}\times\sqrt{3}$ R30° Cl/Ni(111) systems tend to be larger than the results obtained from LEED and ARPEFS studies. This suggests some sort of unknown systematic errors among these techniques. With recent improvements in the quality of data and analysis, it now appears that ARPEFS, LEED, and SEXAFS may be inherently capable of yielding structural parameters of high precision: ± 0.01 - 0.02 Å in the case of ARPEFS, for example. If the remaining discrepancies among the three methods arise from systematic errors, the resolution of those errors is important.

The current ARPEFS study found a 0.104 Å or 5% contraction of the topmost Ni interlayer spacing as compared with that of the bulk for the $\sqrt{3}\times\sqrt{3}$ R30° Cl/Ni(111) system by analyzing structural information from the first and the second Ni layers. However, Kuroda et al. reported no relaxation in the same Cl/Ni(111) system, in contrast to a significant contraction of 15 % in the p(2×2)S/Ni(111) system using their SEXAFS results combined with those from the x-ray standing-wave method. Figure 9 shows the

comparisons of the experimental data for both the [111] and the [110] geometries at 120 K with the calculated $\chi(k)$ curves based on the bulk Ni spacing (2.03 Å), while other parameters were kept fixed at their optimum values. By visual inspection, the agreements for both geometries are very poor, indicating that the substrate surface relaxation is required to obtain the best fits between the experiment and the theory shown in Figs. 6 and 7. Although a combination of x-ray standing-wave and SEXAFS studies provides direct information about the relaxation of the first substrate layer relative to the bulk position, the information about the topmost interlayer spacing is indirect, as it requires the second substrate layer to remain in the bulk position. Low-temperature ARPEFS itself, however, can obtain the topmost interlayer spacing directly for the $\sqrt{3}\times\sqrt{3}$ R30° Cl/Ni(111) system, due to its ability to probe the second substrate layer.

Studies on the clean Cu(111) surface[23] showed a 0.7 ± 0.5% contraction of the topmost interlayer spacing, smaller than the contractions on more open (001) and (110) surfaces. If the clean Ni(111) surface also has little contraction in the topmost interlayer spacing, a 5% contraction in the $\sqrt{3}\times\sqrt{3}$ R30° Cl/Ni(111) system is much larger than that of clean Ni(111) surface, indicating the adsorbate-induced contraction. In contrast to the Cl/Ni(111) system, studies of adsorbates on fcc (001) surfaces such as S- and Cl-covered Ni(001) and Cu(001) have shown expansions of the topmost interlayer spacing,[1,5,8-11,24-25] which has been attributed to metal-metal bond weakening induced by adsorption. The mechanism for contraction is not clear in the $\sqrt{3}\times\sqrt{3}$ R30° Cl/Ni(111) system.

The previous low-temperature ARPEFS study[5] on the Cl/Cu(001) system showed that cooling the lattice effectively extends the range of ARPEFS to the fourth substrate layer. However, in this study, we could only obtain the distances from Cl to the first and to the second layers. In Fig. 2, we note consistent high-frequency oscillations in the experimental $\chi(k)$ curves at two temperatures, as compared with the filtered (10 Å) curves

shown in Figs. 6 and 7, suggesting the existence of real signals at large path-length differences (> 10 Å). Figure 10 shows the experimental Fourier spectrum in the [111] direction at 120 K, with the Fourier spectra obtained from single- and multiple-scattering calculations based on the optimized parameters. The agreement among these three Fourier transform spectra in the range 10 Å - 25 Å is not good enough to permit a quantitative structural interpretation, but it is intriguing. The single-scattering curve shows peaks spaced at 4 Å intervals, consistent with backscattering from the Ni(111) planes spaced at 2.03 Å. In fact, weak peaks near 20 Å and 24 Å, consistent with scattering from the fifth and sixth layers, appear in all three curves. However, for intermediate path-length differences 10 Å - 18 Å, single scattering yields only two peaks, while both multiple scattering and experiment show four. The later two curves agree only in regard to the overall intensity of the pattern of four peaks, but not with respect to their exact positions or detailed intensity pattern. We therefore conclude that the single-scattering calculation omits important (multiple-scattering ) effects which show up in the experimental curve, and the multiple-scattering theory, as we have applied it, does not model these effects accurately.

## 3.5 Conclusion

We have presented a low-temperature ARPEFS study of the $\sqrt{3}\times\sqrt{3}$ R30° Cl/Ni(111) system. The surface structure was determined by two methods: Fourier analysis which gives qualitative structural information and the multiple-scattering spherical-wave (MSSW) analysis, which yields more quantitative results. This ARPEFS study provided a clear distinction between the two inequivalent three-fold hollow sites using directional sensitivity of ARPEFS and found that the fcc three-fold hollow site is favoured for the $\sqrt{3}\times\sqrt{3}$ R30° Cl/Ni(111) system. Low-temperature ARPEFS allows us to

determine structural parameters more accurately due to the increased signal-to-noise ratio. Multiple-scattering spherical-wave (MSSW) analysis found the Cl atom adsorbed in the fcc three-fold hollow site, 1.837(8) Å above the first nickel layer with a Cl-Ni bond length of 2.332(6) Å and an approximate 5% contraction between the first and the second nickel layers, in disagreement with a recent study[13] by Kuroda et al.

# Reference


1. J.J. Barton, C.C. Bahr, S.W. Robey, Z. Hussain, E. Umbach and D.A. Shirley, *Phys. Rev.* **B 34,** 3807 (1986).
2. S.W. Robey, J.J. Barton, C.C. Bahr, G. Liu and D.A. Shirley, *Phys. Rev.* **B 35,** 1108 (1987).
3. L.J. Terminello, X.S. Zhang, Z.Q. Huang, S. Kim, A.E. Schach von Wittenau, K.T. Leung and D.A. Shirley, *Phys. Rev.* **B 38,** 3879 (1988).
4. X.S. Zhang, L.J. Terminello, S. Kim, Z.Q. Huang, A E. Schach von Wittenau and D.A. Shirley, *J. Chem. Phys.* **89**, 6538 (1988).
5. L.Q. Wang, A.E. Schach von Wittenau, Z.G. Ji, L.S. Wang, Z.Q. Huang, and D.A. Shirley, *Phys. Rev.* **B**, July 1991, in press.
6. J.J. Barton, C.C. Bahr, Z. Hussain, S.W. Robey, J.G. Tobin, L.E. Klebanoff and D.A. Shirley, Phys. *Rev. Lett.* **51**, 272 (1983).
7. J.J. Barton, S.W. Robey and D.A. Shirley, *Phys. Rev.* **B 34**, 778 (1986).
8. A.E. Schach von Wittenau, L.Q. Wang, Z.G. Ji, Z.Q. Huang, T. Shulman and D.A. Shirley ( in preparation).
9. F. Jona, D. Westphal, A. Goldmann and P.M. Marcus, *J. Phys. C: Solid State Phys.* **16**, 3001 (1983).
10. P.H. Citrin, D.R. Hamann, L.F. Mattheiss and J.E. Rowe, *Phys. Rev. Lett.* **49**, 1712 (1982).
11. J.R. Patel, D.W. Berreman, F. Sette, P.H. Citrin and J.E. Rowe, *Phys. Rev.* **B 40**, 1330 (1989).
12. M.D. Crapper, C.E. Riley, P.J.J. Sweeney, C.F. McConville, D.P. Woodruff, and R.G. Jones, *Surf. Sci.* **182**, 213 (1987)

13. M. Funabashi, Y. Kitajima, T. Yokoyama, T. Ohta and H. Kuroda, *Physica* **B 158**, 664 (1989)

14. T. Yokoyama, M. Funabashi, Y. Kitajima, T. Ohta and H. Kuroda, *Physica* **B 158**, 643 (1989)

15. P.L. Cowan, S. Brennan, R.D. Deslattes, A. Henins, T. Jach, and E.G. Kessler, *Nucl. Instrum, Methods* **A 246**, 154(1986).

16. S.D. Kevan, Ph.D. thesis, University of California, Berkeley, 1980; LBL-11017.

17. P.J. Orders and C.S. Fadley, *Phys. Rev.* **B 27**, 781 (1983).

18. J.B. Pendry, Low Energy Electron Diffraction (Academic, London, 1974).

19. Y.K. Wu and K.A.R. Mitchell, *Can. J. Chem.* **67**, 1975 (1989).

20. T. Fauster, H. Durr, and D. Hartwig, *Surf. Sci.* **178**, 657 (1986).

21. D. R. Warburton, P.L. Wincott, G. Thornton, F.M. Quinn, and D. Norman, *Surf. Sci.* **211/212**, 71 (1989).

22. J.E. Demuth, D.W. Jepsen, and P.M. Marcus, *Phys. Rev. Lett* **32**, 1182 (1974).

23. S.A. Lindgren, L. Wallden, J. Rundgren and P. Westrin, *Phys. Rev.* **B 29**, 576 (1984).

24. J.E. Demuth, D.W. Jepsen, and P.M. Marcus, *Phys. Rev. Lett.* **31** 540 (1973), and **32**, 1184 (1974).

25. T. Yokoyama, Y. Takata, T. Ohta, M. Funabashi, Y. Kitajima, and H. Kuroda, *Phys. Rev.* **B 42**, 7000 (1990)

Table I. Summary of the structural results (in Å) determined from MSSW analysis. The statistical errors associated with each parameter for the four data sets are given in parentheses.[5] The structural parameter values in the upper panel are derived directly from fits of the data, while those in the lower panel were derived by subtracting two corresponding values above the line.

| Parameter | $[111]_{120k}$ | $[111]_{300k}$ | $[110]_{120k}$ | $[110]_{300k}$ | Avg[a] (stat) | Avg[b] (scat) | This work [c] |
|---|---|---|---|---|---|---|---|
| Cl-Ni(1) | 1.831(8) | 1.828(10) | 1.848(9) | 1.844(16) | 1.837(5) | 1.838(8) | 1.837(8) |
| Cl-Ni(2) | 3.767(10) | 3.763(13) | 3.754(14) | 3.761(40) | 3.763(7) | 3.761(5) | 3.763(7) |
| Cl-Ni (bond length) | | | | | 2.332(4) | 2.333(6) | 2.332(6) |
| Ni(1)-Ni(2) | | | | | 1.926(10) | 1.923(9) | 1.926(11) |

a) Statistical errors only: Standard deviation.

b) Standard deviation from the scatter of results.

c) Final adopted values, with standard deviation taken as the higher of a and b above. Not included in these values and error estimate are any possible offset due to (unknown) systematic error.

# Figure Captions

FIG. 1. A view of the $\sqrt{3}\times\sqrt{3}$ R30° overlayer of chlorine (shaded atoms) on the (111) face of a nickel single crystal. The emission directions are labelled as [111] and [110], while the photon polarization vectors associated with each geometry are labelled as $\hat{\varepsilon}_{[111]}$ and $\hat{\varepsilon}_{[110]}$, respectively.

FIG. 2. Experimental $\chi(k)$ curves for the [111] and the [110] geometries. The curve with solid dots is $\chi(k)$ at 300 K, and the heavier curve is $\chi(k)$ at 120 K.

FIG. 3. Fourier spectra for the [111] and the [110] geometries at two temperatures, 120 K and 300 K. The heavier curves are the spectra at 120 K.

FIG. 4. Top and side views of the $\sqrt{3}\times\sqrt{3}$ R30° Cl/Ni(111) structure. The smaller shaded circles represent the Cl atoms in the fcc sites, while the smaller open circles represent the Cl atoms in the hcp sites. The side view (lower panel) corresponds to a cut in the plane shown the broken line in the top view (upper panel).

FIG. 5. Adsorption site determination for the [111] and the [110] geometries at 120 K. The experimental curves (solid lines) are compared to the MSSW calculated curves (dashed lines) for two kinds of unreconstructed three-fold hollow adsorption geometries (fcc and hcp).

FIG. 6. The best fits of the MSSW calculations (dashed curves) to the filtered (10.0 Å) ARPEFS data (solid curves) for the [111] geometry at two temperatures, 120 K and 300 K.

FIG. 7. The best fits of the MSSW calculations (dashed curves) to the filtered (10.0 Å) ARPEFS data (solid curves) for the [110] geometry at two temperatures, 120 K and 300 K.

FIG. 8. R-factor plots for the [111] and the [110] geometries at the two temperatures, 120 K and 300 K, calculated by varying the Cl-Ni(1) and the Cl-Ni(2) distances, respectively, while other parameters were fixed in their optimum values.

FIG. 9. Comparisons of the filtered (10.0 Å) ARPEFS data (solid curves) to the MSSW calculations (dashed curves) for the [111] and [110] geometries at 120 K. The MSSW curves are calculated with the bulk Ni spacing (2.03 Å), while all the other parameters are kept fixed at their optimum values.

FIG. 10. Comparison among the Fourier spectra for the [111] geometry at 120 K: experimental Fourier spectrum with those spectra obtained from single- and multiple-scattering calculations based on the optimized parameters.

$\sqrt{3} \times \sqrt{3}$ R30° Cl/Ni(111)

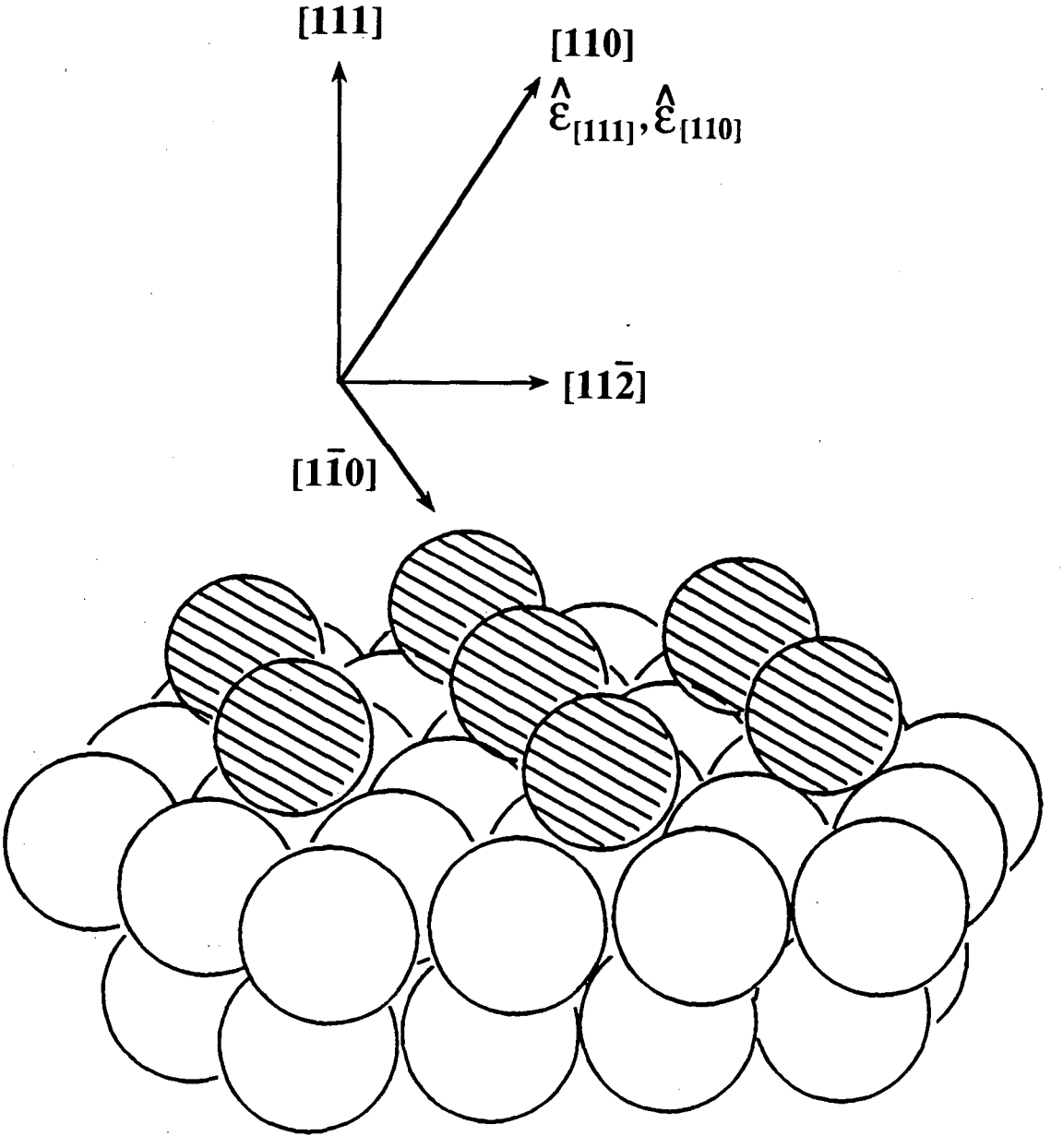


Figure 1

XBL 914-738

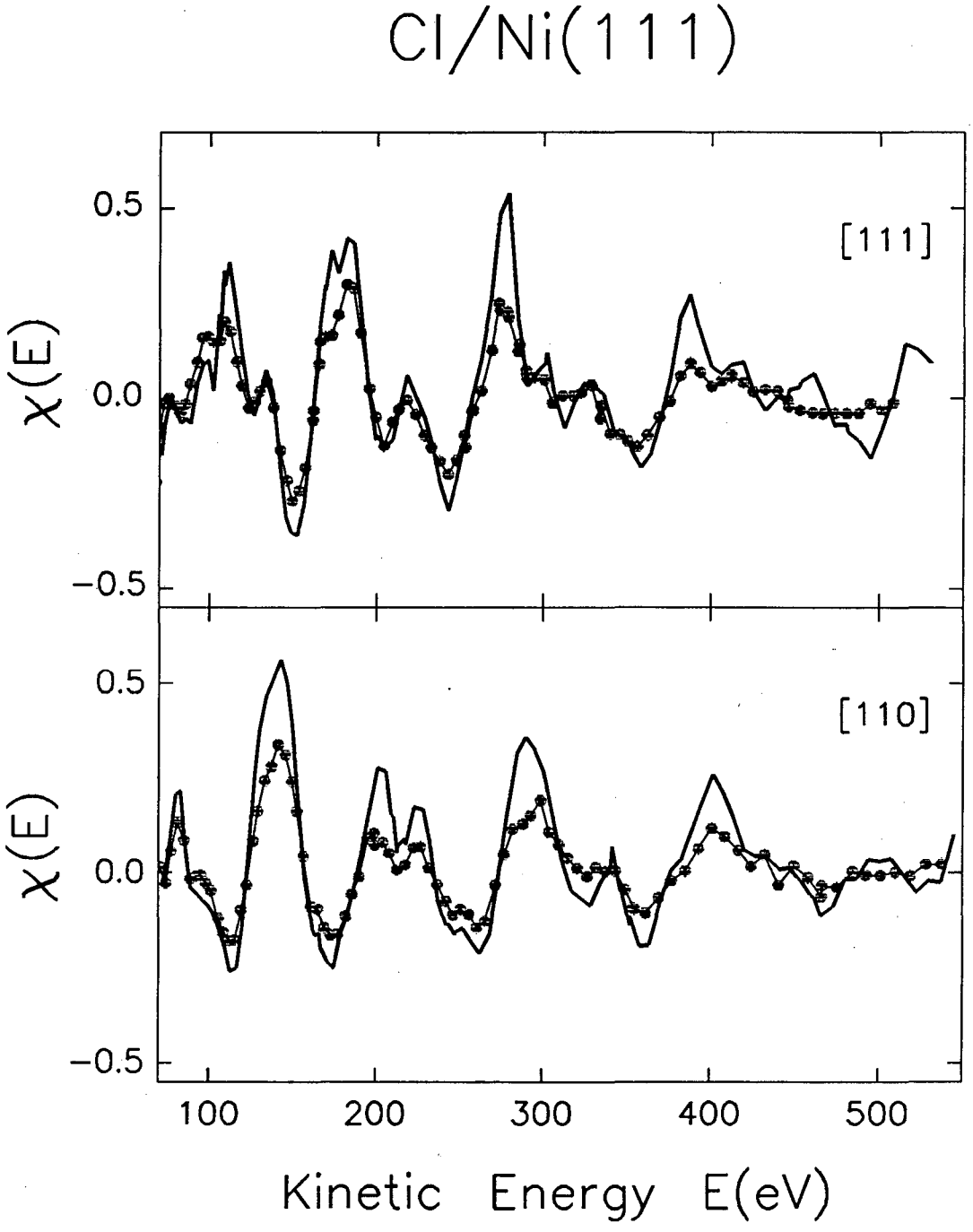
Cl/Ni(111)
0.5
0.0
−0.5
χ(E)
[111]
0.5
0.0
−0.5
χ(E)
[110]
100
200
300
400
500
Kinetic Energy E(eV)

Figure 2

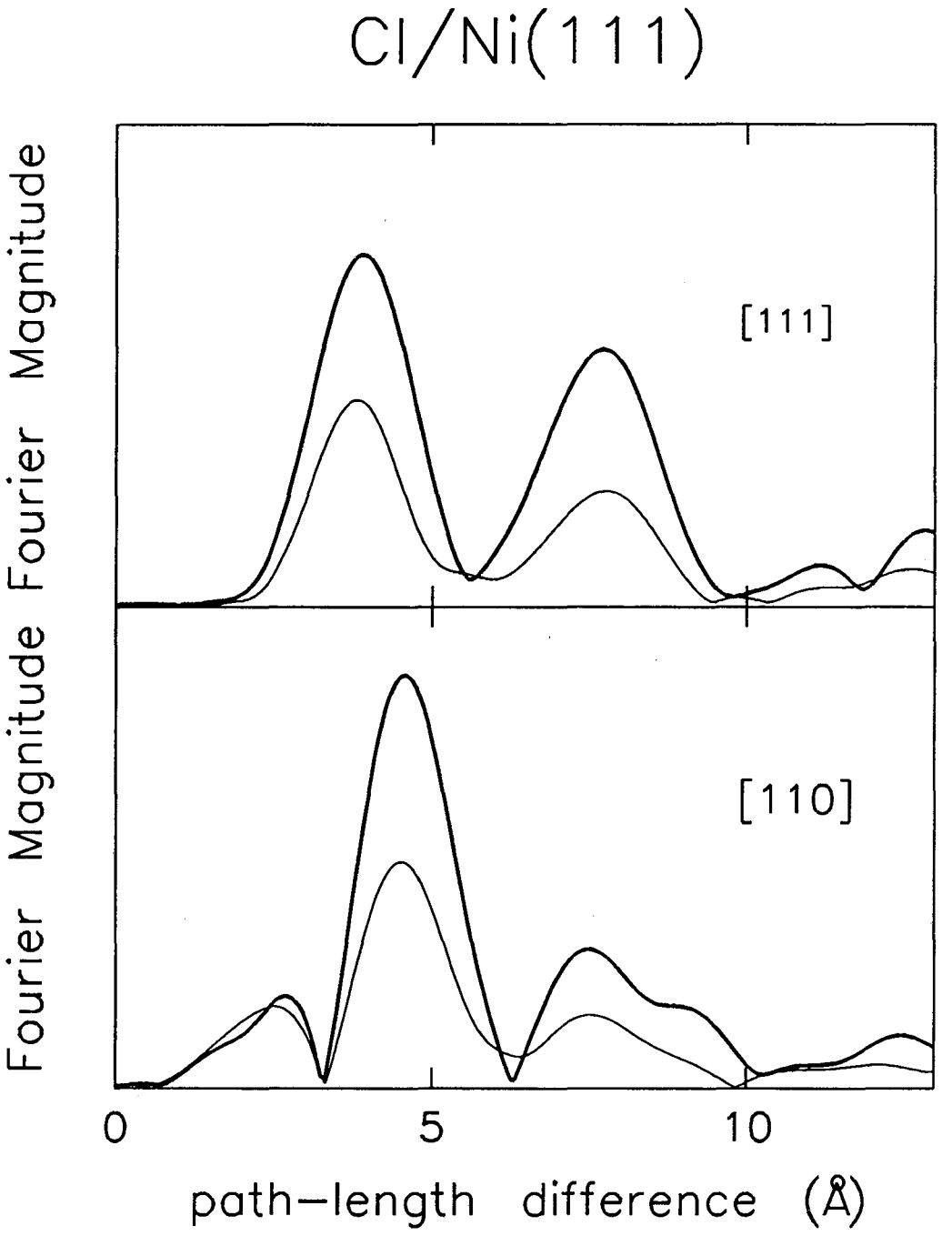
Cl/Ni(111)
Fourier Magnitude Fourier Magnitude
[111]
[110]
0
5
10
path-length difference (Å)

Figure 3

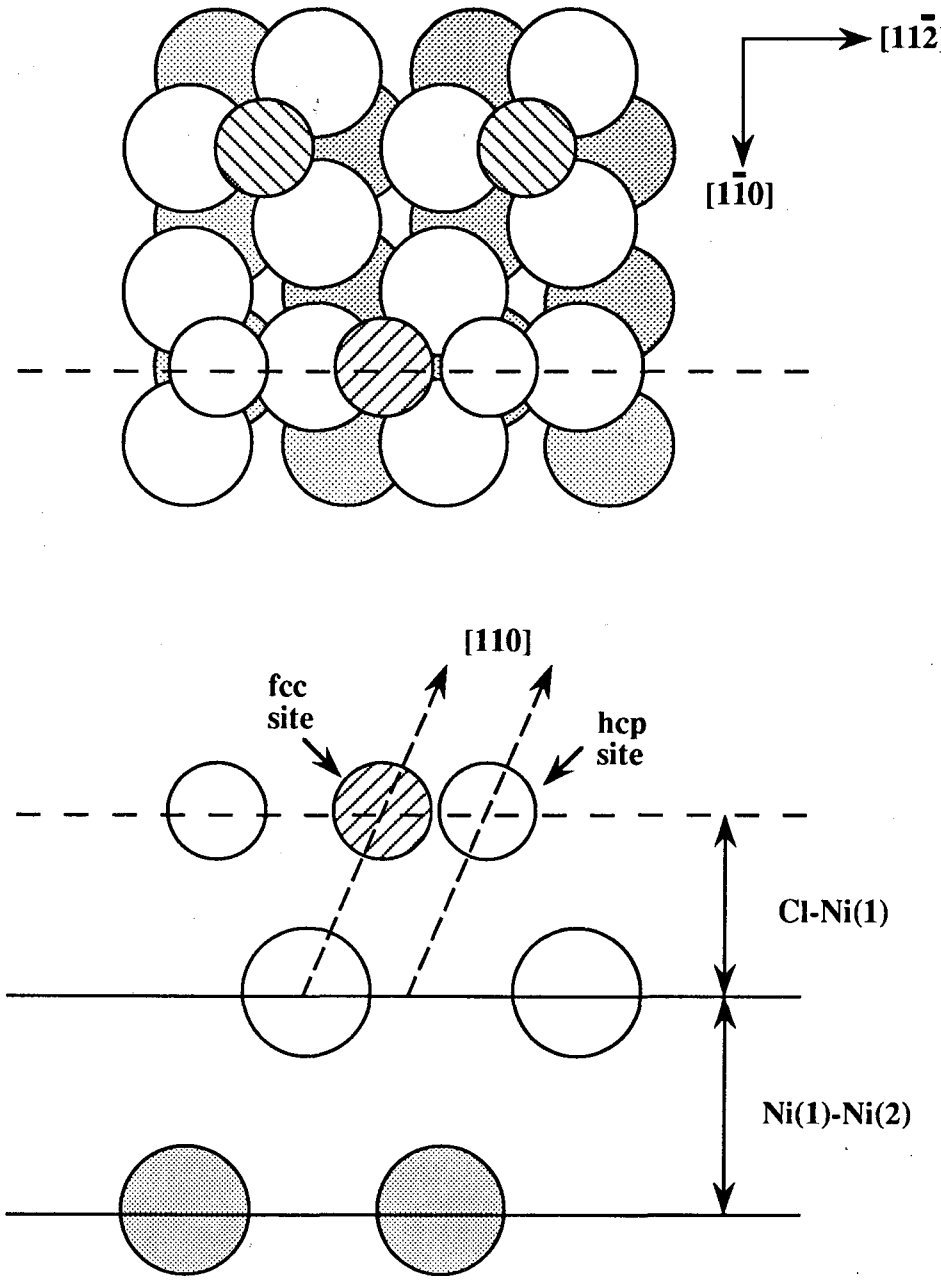


Figure 4

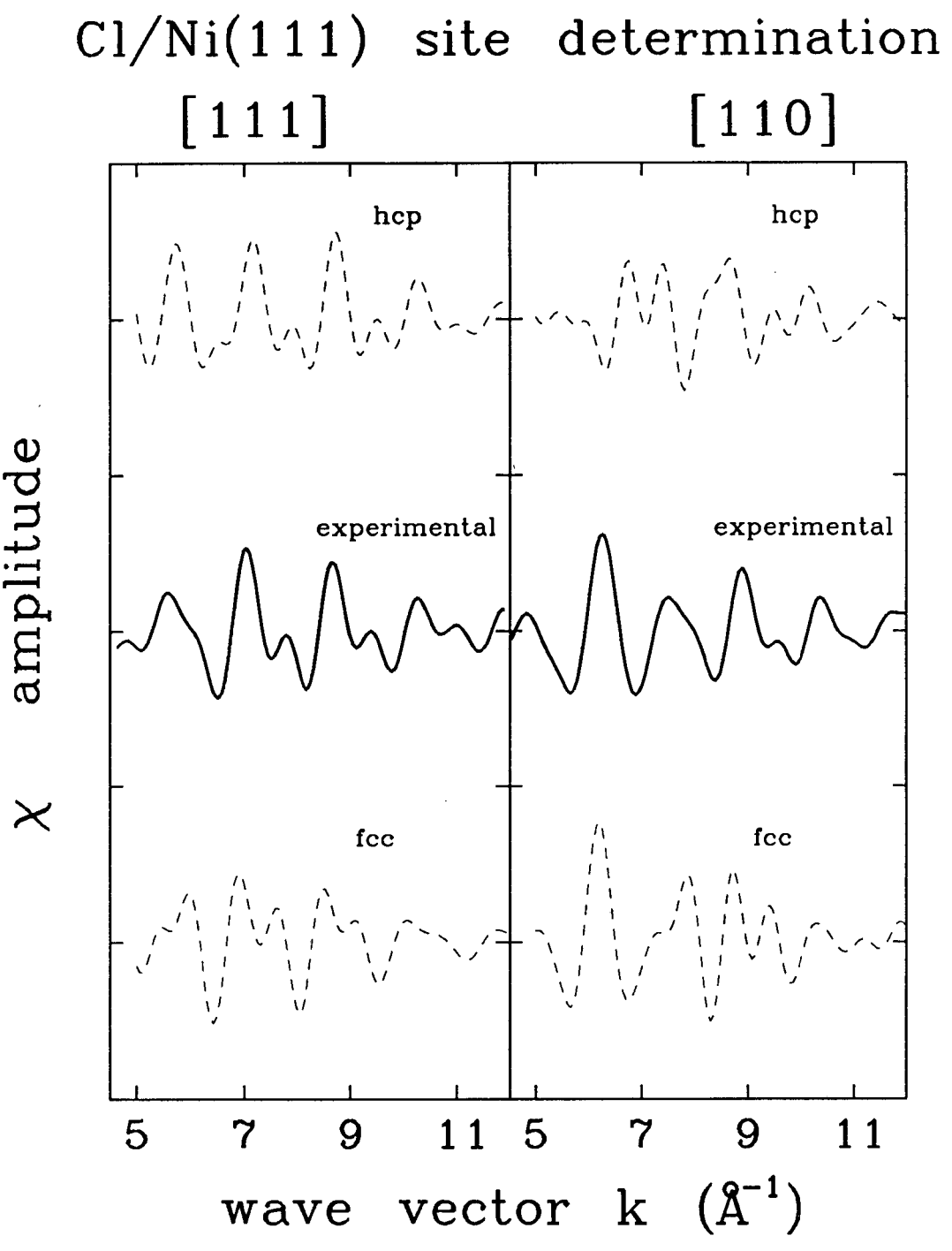
Cl/Ni(111) site determination
[111]
[110]
hcp
hcp
experimental
experimental
fcc
fcc
χ amplitude
5
7
9
11
5
7
9
11
wave vector k (Å$^{-1}$)

Figure 5

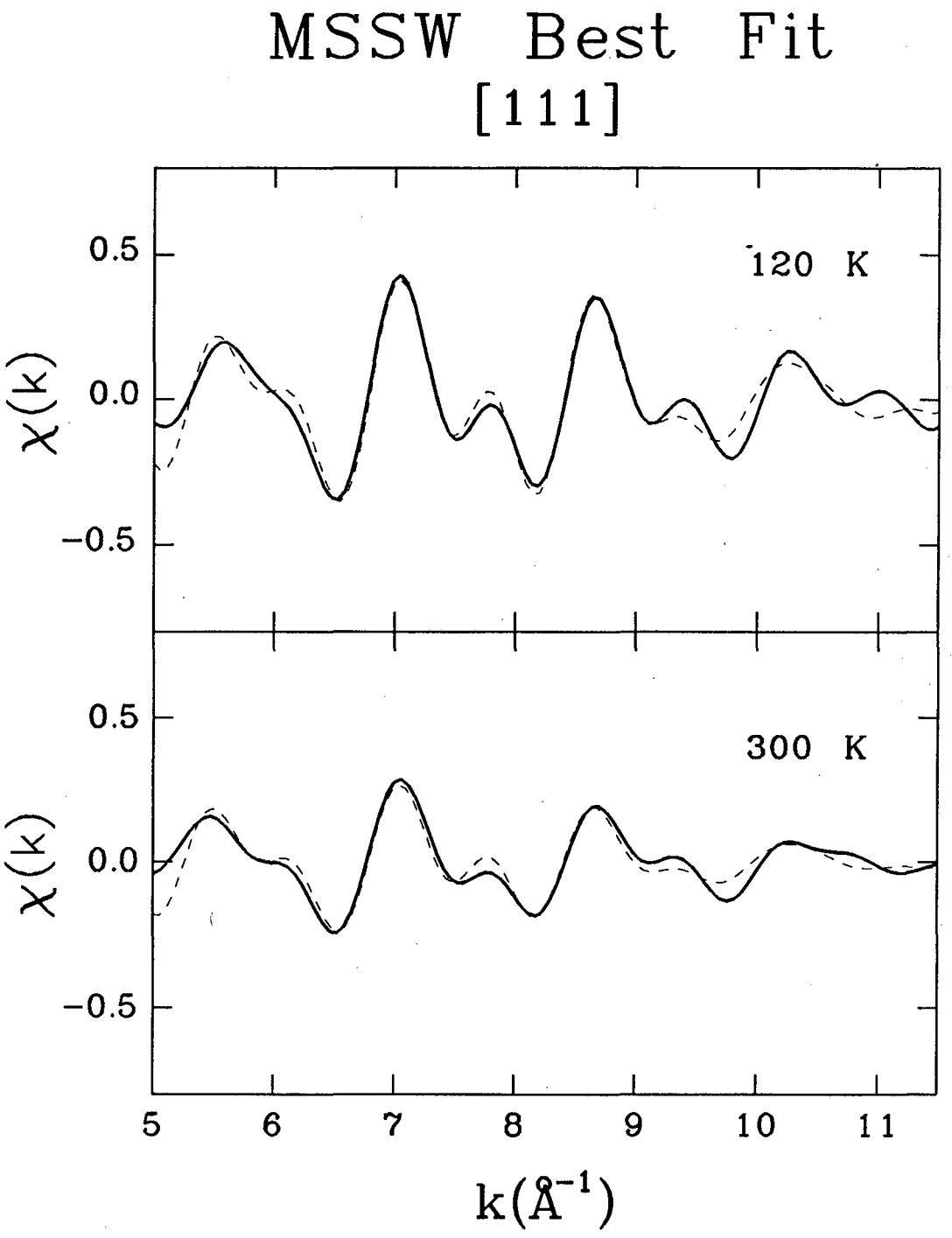


Figure 6

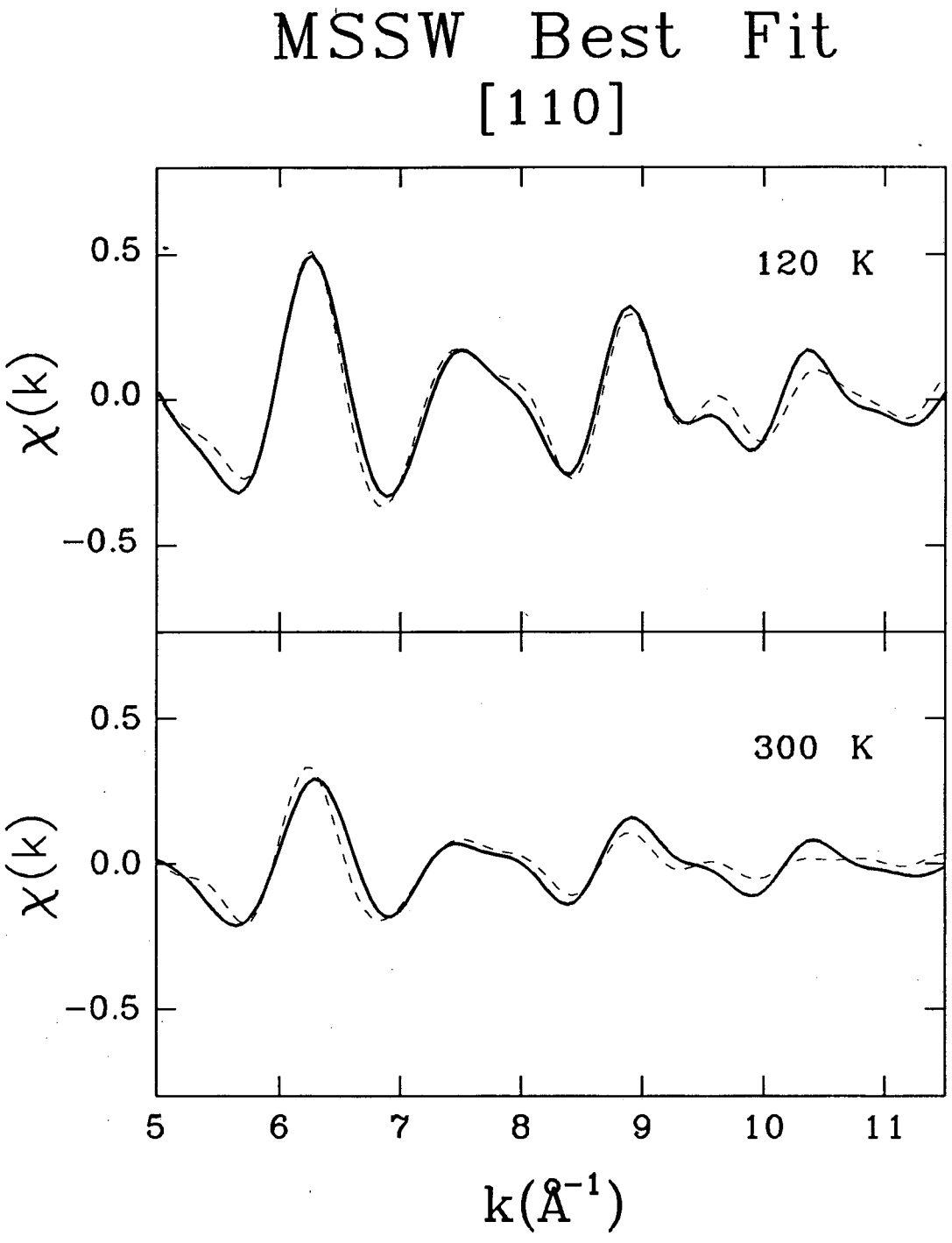


Figure 7

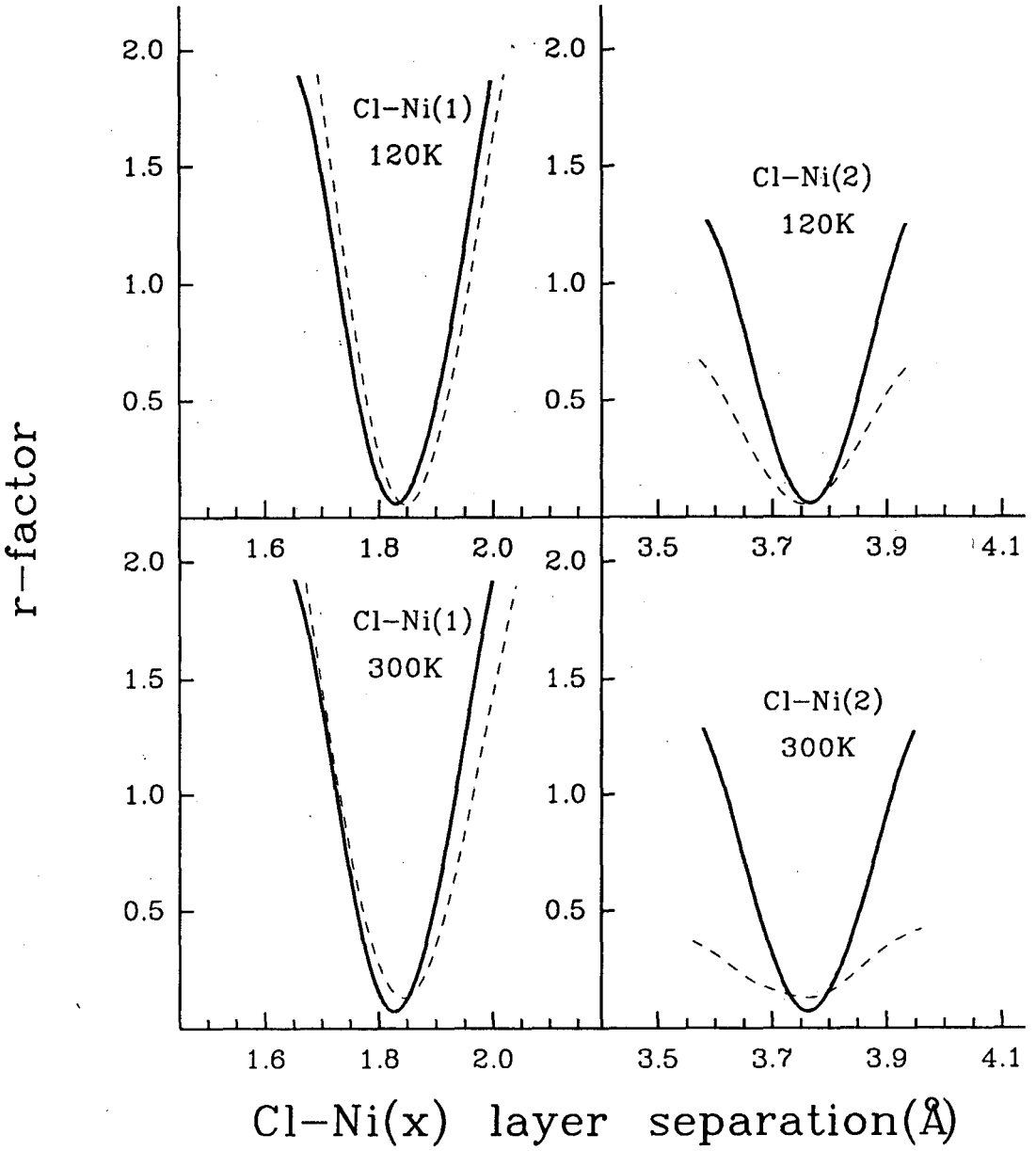
r-factor
Cl-Ni(1)
120K
Cl-Ni(2)
120K
Cl-Ni(1)
300K
Cl-Ni(2)
300K
2.0
1.5
1.0
0.5
1.6
1.8
2.0
3.5
3.7
3.9
4.1
Cl-Ni(x) layer separation(Å)

Figure 8

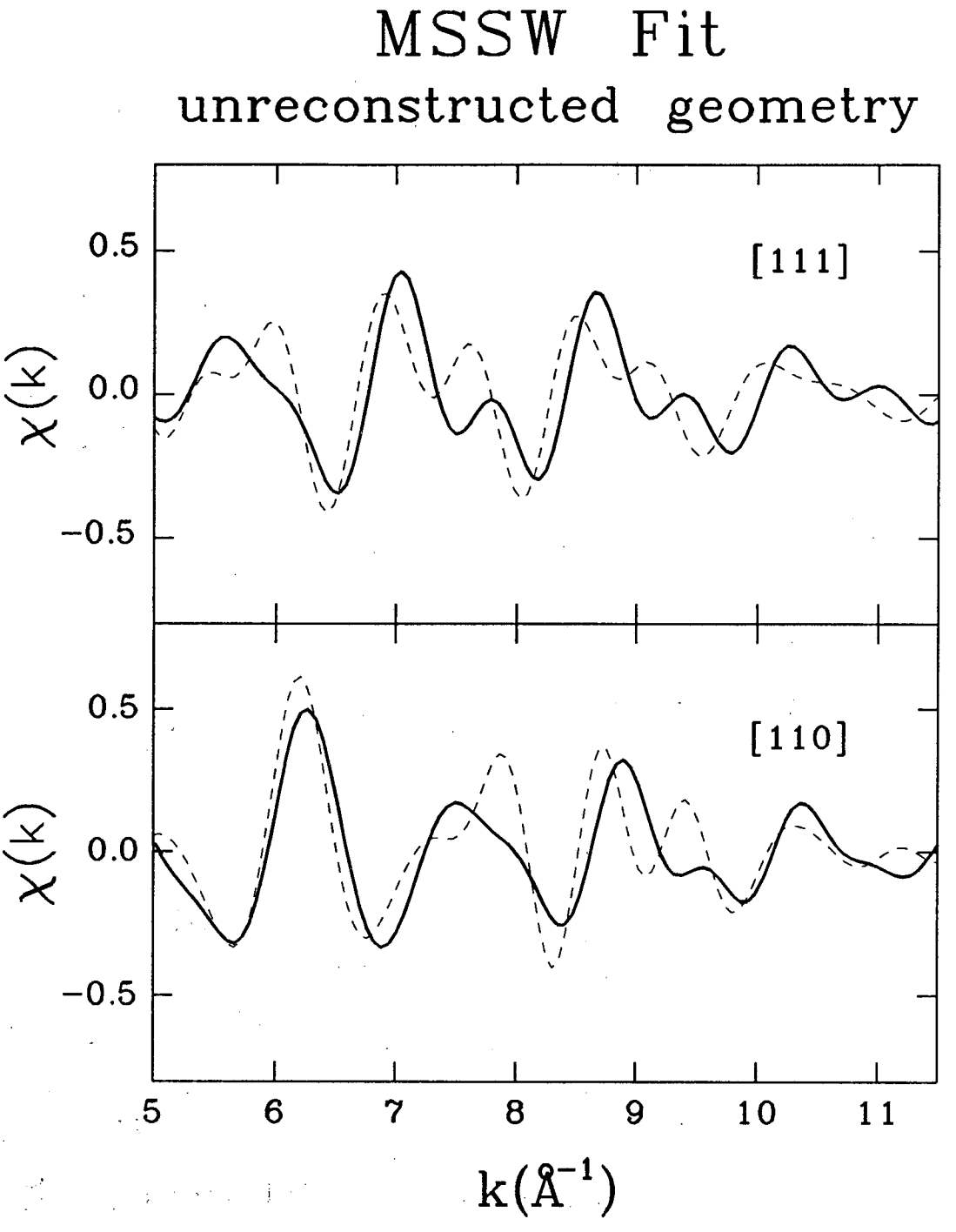
MSSW Fit
unreconstructed geometry
[111]
[110]
χ(k)
0.5
0.0
−0.5
5
6
7
8
9
10
11
k(Å⁻¹)

Figure 9

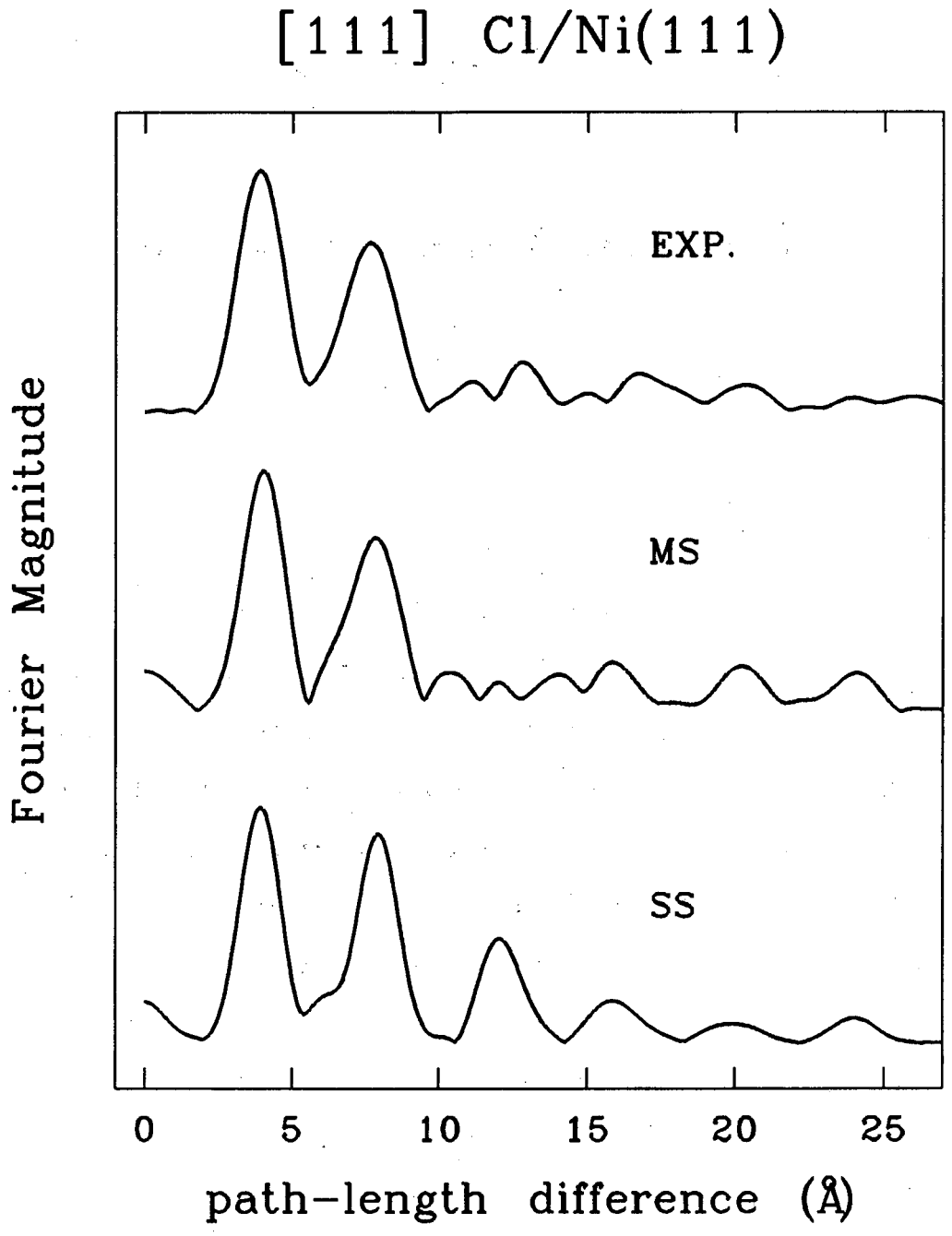
[111] Cl/Ni(111)
EXP.
MS
SS
Fourier Magnitude
0
5
10
15
20
25
path-length difference (Å)

Figure 10

# Chapter 4

# Surface-Atom Vibrations

## Abstract

A study of surface-atom vibrations for both the $\sqrt{3}\times\sqrt{3}$ R30° Cl/Ni(111) and c(2×2)Cl/Cu(001) systems was made using temperature-dependent ARPEFS. The adsorbate mean-square displacements in the direction parallel to the surface were found to be larger than those perpendicular for both systems. However, the relative magnitude of the vibrational anisotropy in the parallel direction to the perpendicular direction was found to be larger for the $\sqrt{3}\times\sqrt{3}$ R30° Cl/Ni(111) than that for the c(2×2)Cl/Cu(001). A model for predicting the adsorbate vibrational anisotropy from the structures was proposed and also successfully applied to the $\sqrt{3}\times\sqrt{3}$ R30° Cl/Ni(111), the c(2×2)Cl/Cu(001), and other available systems. This model offered a simple and straightforward physical picture for understanding different types of vibrational anisotropy. For example, the c(2×2) overlayers of S and O on Ni(100) have the opposite vibrational anisotropy for S and O atoms.

# 4.1 Introduction

During recent years, there have been remarkable advances in the understanding of lattice vibrations on both clean and adsorbate-covered surfaces. Techniques such as He-atom scattering[1] and electron energy-loss spectroscopy (EELS)[2] have proved to be powerful tools for studying surface-atom vibrations from the dispersion relations of surface phonons and surface resonances. Recent studies[3-6] using temperature- and polarization-dependent surface extended x-ray-absorption fine structure (SEXAFS) have showed that the difference of mean-square relative displacements (MSRD) between two temperatures can be extracted experimentally through Debye-Waller factors which take into account the vibrational attenuation in scattering processes. In this chapter, we focus on the temperature-dependent angle-resolved photoemission extended fine structure (ARPEFS).

The existence of surface-atom anisotropic vibrations has been addressed in several recent studies. In a study of epitaxial, unrelaxed (1×1)Co/Cu(111) surface, Roubin et al.[3] found a larger amplitude in the correlated surface-atom vibrations perpendicular to the surface than in those parallel, which is consistent with the conventional view for clean metal surfaces that perpendicular surface-atom vibrational amplitudes should be larger because of the increased degrees of freedom at the surface. This is also true for the c(2×2)O/Ni(001) system.[7-8] However, the opposite vibrational anisotropy was found by Sette et al.[5] for the c(2×2)Cl/Cu(001) system, where vibrational amplitudes of surface atoms in the direction perpendicular to the surface is smaller than those parallel to the surface. Studies of S and Cl overlayers on Ni(100)[6] also showed the similar trend. It seems that whether the surface-atom vibrational amplitude perpendicular to the surface is larger than that parallel to the surface depends on the specific adsorbate system. An

interesting question is raised: can a universal model be proposed to predict the surface-atom vibrational anisotropy for all the systems mentioned above?

A specific adsorbate system has its unique geometric structure. Surface properties such as geometric structures, electronic structures, and dynamic phenomena are often related to each other. In this study, we present a model to predict the vibrational anisotropy from structures and to link static structural and dynamic information. Since both ARPEFS and SEXAFS are direct in determining surface structures, structural parameters obtained from them can be used to predict the vibrational anisotropy. At the same time, the results obtained from the model prediction can be compared with those extracted from the experiments for the same system. Unlike SEXAFS, ARPEFS has high directional sensitivity. Thus, the vibrational anisotropy may be more prominent in ARPEFS than in SEXAFS. In this chapter, we investigate the vibrational anisotropy for both the c(2×2)Cl/Cu(001) and $\sqrt{3}\times\sqrt{3}$ R30° Cl/Ni(111) systems by using temperature-dependent ARPEFS.

There are several reasons for studying both the c(2×2)Cl/Cu(001) and $\sqrt{3}\times\sqrt{3}$ R30° Cl/Ni(111) systems. First, our results for the c(2×2)Cl/Cu(001) can be compared with those obtained from SEXAFS. Because of the difference between the fcc(111) and fcc(001) lattices, we expect that a study of $\sqrt{3}\times\sqrt{3}$ R30° Cl/Ni(111) could give different results from that of c(2×2)Cl/Cu(001). Second, structural parameters from the previous low-temperature ARPEFS studies on both systems[9-10] can be used to predict the the vibrational anisotropy. Also, we can test our model for predicting the vibrational anisotropy with the results extracted from the temperature-dependent ARPEFS measurements on both systems.

Section 4.2 introduces the theoretical treatment for the vibrational attenuation in ARPEFS. Section 4.3 describes the detailed procedures for extracting vibrational

anisotropy from ARPEFS experiments, and compares the ARPEFS method with SEXAFS. The results for both c(2×2)Cl/Cu(001) and $\sqrt{3}\times\sqrt{3}$ R30° Cl/Ni(111) systems are also presented in this section. In Sec. 4.4, a model for predicting the vibrational anisotropy is proposed and applied to several adsorbate systems. Discussion and conclusions are given in Sec. 4.5.

## 4.2 Theoretical Treatment

An atom vibrates around its equilibrium position in a crystal lattice. The effect of lattice vibrations was first discussed by Schmit[11] and later was treated more completely in EXAFS by Beni and Platzman[12]. Since electron scattering takes place on a time scale much shorter than that of atomic motion, the measurement of individual events in fact takes a snapshot of the instantaneous atomic configurations. Therefore, an average of all these configurations must be taken in the calculating of the extended fine structure. The instantaneous position of the scattering atom can be written as:

$$\mathbf{a} = \mathbf{a}_0 + \mathbf{u}_a - \mathbf{u}_0 = \mathbf{a}_0 + \Delta\,\mathbf{u}_a\,, \qquad (1)$$

where $\mathbf{a}_0$ is the equilibrium position of the scattering atom, $\mathbf{u}_0$ and $\mathbf{u}_a$ are the displacements for the emitting atom (origin) and the scattering atom, respectively, and $\Delta\,\mathbf{u}_a$ is the change in the equilibrium bond length (see Fig. 1).

In analogy to EXAFS,[12] an ARPEFS $\chi$ function in a single scattering case can be represented by

$$\chi(\mathbf{a}) = \chi(\mathbf{a}_0) < \exp\,(\,-i\,\mathbf{K}_{aR}\cdot\Delta\,\mathbf{u}_a\,) >\,, \qquad (2)$$

where $\mathbf{K}_{aR} = k\,(\,\hat{\mathbf{R}} - \hat{\mathbf{a}}_0\,)$: the unit vector $\hat{\mathbf{R}}$ specifies the direction to the electron analyzer, and k is the electron wave-number (see Fig. 2).

In the harmonic approximation,[13] we have

$$< \exp ( -i \mathbf{K}_{aR}.\Delta \mathbf{u}_a ) > = \exp [-\frac{1}{2} < ( \mathbf{K}_{aR}.\Delta \mathbf{u}_a )^2 >]$$
$$= \exp [-\frac{|\mathbf{K}_{aR}|^2}{2} < ( \hat{\mathbf{K}}_{aR}.\Delta \mathbf{u}_a )^2 >]$$
$$= \exp (-\frac{|\mathbf{K}_{aR}|^2}{2} \sigma_a^2 )$$
$$= \exp (-k^2 (1- \cos\theta_{aR}) \sigma_a^2 ) , \qquad (3)$$

where $\sigma_a^2 = < ( \hat{\mathbf{K}}_{aR}.\Delta \mathbf{u}_a )^2 >$ and $|\mathbf{K}_{aR}|^2 = 2k^2 (1- \cos\theta_{aR})$. The above term in Eq. (3) is the Debye-Waller factor describing the vibrational attenuation in ARPEFS. Here $\sigma_a^2$ is the temperature-dependent mean-square relative displacement (MSRD) between the emitting and scattering atoms projected on the photoelectron momentum change direction $\mathbf{K}_{aR}$.

There are several physical models for calculating $\sigma_a^2$. The Debye model has been extensively used to predict the mean-square relative displacements,[12,14] in agreement with EXAFS experiments[15]. Recently, Barton et al.[16] proposed a modified ARPEFS Debye model including the surface-layer dependence, the anisotropy of the mean-square displacements, and the mass dependence required for an adsorbate, based on a combination of the work of Allen et al.[17] on mean-square displacements on surfaces, of Housley and Hess[18] on mean-square displacements in general, and of Sevillano et al.[14] on mean-square relative displacements.

The MSRD $\sigma_a^2$, can be expanded into the sum of the mean-square displacements (MSD) of the emitting atom (origin) and the scattering atom, projected on $\mathbf{K}_{aR}$, minus twice their displacement correlation function (DCF):

$$< [ \hat{\mathbf{K}}_{aR}.(\mathbf{u}_a - \mathbf{u}_o) ]^2 > \approx < ( \hat{\mathbf{K}}_{aR}. \mathbf{u}_a )^2 > + < ( \hat{\mathbf{K}}_{aR}. \mathbf{u}_o )^2 >$$
$$-2[< ( \hat{\mathbf{K}}_{aR}. \mathbf{u}_a )( \hat{\mathbf{K}}_{aR}. \mathbf{u}_o ) >] . \qquad (4)$$

In Cartesian coordinates, we approximate

$$< ( \hat{\mathbf{K}}_{aR} . \mathbf{u}_a )^2 > = \sum_{\alpha=(x,y,z)} \hat{\mathbf{K}}_\alpha^2 < ( \mathbf{u}_a )_\alpha^2 > . \qquad (5)$$

Here we choose x and y for the two orthogonal directions in a plane parallel to the surface, and z for the direction perpendicular to the surface. The mean-square vibrational displacement for the individual atom in a given direction $\alpha$ is given by[14]

$$< ( \mathbf{u}_a )_\alpha^2 > = \frac{\hbar}{2m_a} \int_0^{\omega_{max}} \frac{\coth(\hbar\omega/2k_BT)}{\omega} f_\alpha(\omega, l_{3a})\, d\omega , \qquad (6)$$

where $m_a$ is the atomic mass, $f_\alpha(\omega, l_{3a})$ is the normalized density of states at frequency $\omega$ with $\alpha$-direction displacements on atoms in layer $l_{3a}$, and $\omega_{max}$ is the highest frequency of the system.

In the moderate-temperature region (i.e., $T > \frac{\hbar\omega_{max}}{2\pi k_B}$), according to a Thirring expansion[13,19] of $\coth x \approx 1/x + x/4$, we obtain

$$< ( \mathbf{u}_a )_\alpha^2 > = \frac{k_BT}{m_a} < \omega_\alpha^{-2}(l_{3a}) > + \frac{\hbar^2}{16 m_a k_B T} < \omega_\alpha^{0}(l_{3a}) > . \qquad (7)$$

Here we introduce the moment of the frequency distribution,

$$< \omega_\alpha^n(l_{3a}) > = \int_0^{\omega_{max}} f_\alpha(\omega, l_{3a})\, \omega^n\, d\omega . \qquad (8)$$

First, we apply the Debye model for describing the density of states,

$$f_\alpha(\omega, l_{3a}) = \frac{3\omega^2}{[\omega_D(l_{3a})]_\alpha^3} , \qquad (9)$$

where $\omega_D = \theta_D(k_B/\hbar)$ and $\theta_D$ is the Debye temperature. The directional- and layer-dependent Debye-frequency cutoff $[\omega_D(l_{3a})]_\alpha$, is associated with the directional- and layer-dependent Debye temperature $\theta_D(\alpha,l_{3a})$. In the Debye approximation, we substitute $\omega_{max}$ into Eq. (8) with $\omega_D$. Thus, we can calculate

$$< \omega_\alpha^0(l_{3a}) > = \int_0^{\omega_D} \frac{3\omega^2}{[\omega_D(l_{3a})]_\alpha^3} d\omega = 1 \qquad (10)$$

and

$$< \omega_\alpha^{-2}(l_{3a}) > = \int_0^{\omega_D} \frac{3\omega^2}{[\omega_D(l_{3a})]_\alpha^3} \omega^{-2} d\omega = \frac{3}{\omega_D^2} = \frac{3\hbar^2}{[k_B\theta_D(\alpha,l_{3a})]^2} . \qquad (11)$$

Therefore,

$$< ( u_a )_\alpha^2 > = \frac{3\hbar^2}{k_B\theta_D(\alpha,l_{3a})m_a} [ \frac{T}{\theta_D(\alpha,l_{3a})} + \frac{\theta_D(\alpha,l_{3a})}{48T} ] . \qquad (12)$$

The above equation shows that the projected atomic mean-square displacement in the direction $\alpha$, with $\alpha$ = x, y, or z, can be calculated from the individual atomic mass $m_a$, the anisotropic and surface-layer dependent Debye temperature $\theta_D(\alpha,l_{3a})$, and the experimental temperature T. Hence, the surface-atom vibrations described by the mean-square displacement (MSD) of the individual atom depends on the above factors. The softer substrate surface ( lower $\theta_D$ ), the higher temperature, and the smaller atomic mass give the larger attenuation of ARPEFS oscillation amplitudes. A similar treatment can be used to calculate the DCF function of the MSRD, $\sigma_a^2$.

Now we apply the Einstein model for calculating the density of states,

$$f_\alpha(\omega, l_{3a}) = \delta [\omega - \omega_E(l_{3a})] , \qquad (13)$$

where $\omega_E = \theta_E(k_B/\hbar)$, $\theta_E$ is the Einstein temperature, and $\omega_E = \omega_{max}$. According to Eq. (6), we obtain

$$< ( u_a )_\alpha^2 > = \frac{\hbar}{2m_a} \int_0^{\omega_E} \frac{\coth(\hbar\omega/2k_BT)}{\omega} \delta [\omega - \omega_E(l_{3a})] d\omega$$

$$= \frac{\hbar}{2m_a\omega_E}\coth(\hbar\omega_E/2k_BT)$$

$$= \frac{\hbar^2}{2m_ak_B\theta_E}\coth(\theta_E/2T)\,. \qquad (14)$$

Thus, the directional- and layer-dependent Einstein temperature $\theta_E$ can be used to estimate the MSD for a given direction. It has been shown that the Einstein model also reasonably modelled the experiment.[14]

Although both Debye and Einstein models oversimplify the density of states for real systems, they give good estimates of the MSRD for the experiments. As Barton et al.[16] have suggested, the averaging property of the moments of vibrational frequency distribution might reduce the errors in both models. The lattice-dynamic calculations provides more accurate values for the MSRD. However, it requires information about geometry and force constants of surface bonding for constructing the normal modes and eigenstates. For many surface systems, this approach is not practical because of our poor understanding of them. Thus, Debye and Einstein models have been extensively used in ARPEFS, SEXAFS, and LEED for the theoretical treatment of the vibrational attenuation. Although the Einstein model is cruder than the Debye model because it only assumes a single vibrational frequency for an ensemble of noncorrelated harmonic oscillator, a theoretical study[14] showed that the differences in estimating the MSRD between two models are not profound. In this study, we use the modified ARPEFS Debye model to estimate the MSRD in calculating theoretical $\chi$ curves. The previous ARPEFS studies on both the c(2×2)Cl/Cu(001) and $\sqrt{3}\times\sqrt{3}$ R30° Cl/Ni(111) systems[9-10] mainly emphasized structural information. However, this study using temperature-dependent ARPEFS is to obtain the surface-atom vibrational information and to provide a useful test for the validity of the modified Debye model. Any anharmonicity is not included in the study.

# 4.3 Data Analysis and Results

## 4.3.1 Ratio Method

As we have discussed in the previous section, the thermally excited vibrational motion of surface atoms is greatly dependent on the temperature. This temperature effect is included in the extended fine structure by multiplying a temperature-dependent vibrational attenuation factor. In a single-scattering model[20], an ARPEFS $\chi$ function at temperature T can be written as:

$$\chi(k,T) = 2\sum_j A_j(k) \cos[kr_j (1-\cos\theta_j) + \phi_j] \exp[-\sigma_j^2(T) (1-\cos\theta_j)k^2] , \quad (15)$$

where the summation is over all atoms near the adsorbed "source" atom from which core-level photoemission originates. Here $A_j(k)$ contains the elastic scattering amplitude modified by the inelastic losses and aperture integration, $r_j$ is the distance between the photoemitter and j th scattering atom , $\theta_j$ is the scattering angle at the j th atom, and $\phi_j$ is the scattering phase shift. The last term in Eq. (15) is the ARPEFS vibrational attenuation factor, or the Debye-Waller factor, with $\sigma_j^2(T)$ being the mean square relative displacement (MSRD) between the photoemitter and the j th scattering atom, projected on the photoelectron momentum change direction.

By taking the logarithmic ratio of $\chi$ functions given in Eq. (15) at two different temperatures, $T_1$ and $T_2$, for a single scattering off the j th scattering atom, we obtain

$$\ln \left[ \frac{\chi_j(k,T_1)}{\chi_j(k,T_2)} \right] = k^2 (1-\cos\theta_j) [\sigma_j^2(T_2) - \sigma_j^2(T_1)]$$

$$= k^2 (1-\cos\theta_j) \Delta\sigma_j^2(T), \quad (16)$$

where $\Delta \sigma_j^2(T)$ is the change of $\sigma_j^2(T)$ between two temperatures. Equation (16) shows the linearity of the logarithmic ratio of two $\chi$ curves at different temperatures, as a function of $k^2$, with a slope of $(1-\cos\theta_j)\,\Delta \sigma_j^2(T)$.

Figure 3 illustrates the ratio method for evaluating $\Delta \sigma_j^2(T)$. The two $\chi$ curves (see Fig. 3a) at different temperatures were calculated from a 5-atom linear chain using a single-scattering model. The Fourier spectra (see Fig. 3b) show four well-separated peaks corresponding to each of the four substrate atoms in the chain. After inverse Fourier transform of the first peak, we obtained two $\chi$ curves (see Fig. 3c) corresponding to the single scattering only from the first nearest-neighbor. These two $\chi$ curves at different temperatures have the same scattering phase $\phi_j(k)$, but different amplitude functions $A_j(k,T)$. Fig. 3d shows the linearity of the logarithmic ratio of the amplitudes of the above two $\chi$ curves at 110 K and 300 K, in the $k^2$ range of 25-150 $Å^{-2}$.

The ratio method was originally used in EXAFS. Until recently, it has been applied to SEXAFS. This method is simple and theory-independent because it does not require any backscattering amplitudes and phase shifts determined from a model compound or from theoretical calculations, thus eliminating some systematic errors from estimating these parameters. However, SEXAFS studies using the ratio method can only obtain the difference of the mean-square relative displacements $\Delta \sigma_j^2$ between two temperatures, but not the $\sigma_j^2$ itself, or the absolute mean-square displacement $< u^2 >$ for the individual atom. Thus, we can not compare the SEXAFS results directly with those obtained from x-ray diffraction or LEED, where the absolute amplitude of mean-square displacement is given. From Eqs. (15) and (16), we can see that the logarithmic ratio of two $\chi$ curves is a linear function of $k^2$ only for the single-scattering case. Furthermore, a good linearity of the logarithmic ratio of two experimental $\chi$ curves requires high-quality

data at both temperatures. Indeed, several SEXAFS experiments have shown the linear $k^2$-dependent plots in the limited range ($k^2$ = 10-80 $Å^{-2}$) for several near shells, indicating the dominance of single scattering in these shells. For the higher shells, the linearity is worse because of multiple scattering. Now the question is whether or not we can apply the ratio method to the temperature-dependent ARPEFS in the similar way as with the SEXAFS.

Although ARPEFS is analogous to SEXAFS, there are differences between them. In ARPEFS, the interference of photoelectron waves takes place at the angle-resolved electron detector, depending on the scattering path-length difference, while in SEXAFS, the interference happens on the emitter, giving the interatomic distance between the emitter and the scatterer. The single-scattering model has proven to be adequate for SEXAFS, but not for ARPEFS which requires multiple-scattering spherical wave (MSSW) theory.[16] As we have discussed in chapter 3, the strongest peak at a path-length difference ~ 4.6 Å in the [110] Fourier spectra of the $\sqrt{3}\times\sqrt{3}$ R30° Cl/Ni(111) was mainly assigned to the backscattering by one of the three nearest-neighbor substrate atoms along the [110] direction, and then forward focussing by the adsorbate atom (emitter) to the detector. Forward focussing itself does not bring any additional changes to the attenuation factor because of $\exp[-k^2(1 - \cos\theta_{aR})\sigma_a^2] = 1$, when $\theta_{aR} = 180^o$. Thus, backscattering and forward focussing together should also give the linearity of the logarithmic ratio as does the single scattering alone shown in Fig. 3. However, we can not obtain the linear function for the strong Fourier peak at ~ 4.6 Å by using the ratio method (see Fig. 4), indicating that this peak may contain different scattering events with similar path-length differences. Figure 5 shows the comparison of the $\chi(k)$ curve calculated with a single-pair scattering (backscattering and forward focussing) model to a full multiple-scattering calculation based on the optimum parameters obtained from chapter 3. We can see that

backscattering and forward focussing together contribute most of the intensity of the peak at ~ 4.6 Å. However, there are still some differences between these two $\chi$ curves, indicating that other scattering events exist besides the backscattering and forward focussing described in a single-pair scattering model. Since a full multiple-scattering model which accurately describes the experimental data includes a large cluster size of several atoms in the first and second substrate layers with up to the fourth-scattering order, the nonlinearity of the logarithmic ratio must be due to these many different scattering events. Thus, we can not simply use the ratio method in ARPEFS as with SEXAFS. However, in comparison with SEXAFS, high directional sensitivity and large oscillations in ARPEFS should allow us to determine surface-atom vibrational amplitudes from experimental data. But a different approach has to be taken to analyze the temperature-dependent ARPEFS data.

### 4.3.2 ARPEFS Analysis and Results

In this section, we present ARPEFS analysis and results for both the c(2×2) Cl/Cu(001) and $\sqrt{3}\times\sqrt{3}$ R30° Cl/Ni(111) systems. Since multiple scattering and many scatterers are involved in a single ARPEFS Fourier peak, we expect the ARPEFS analysis to be more complicated than the simple ratio method used in SEXAFS. In our analysis, we simulate the temperature-dependent ARPEFS data with the multiple-scattering spherical-wave (MSSW) theory[16] including a modified Debye model described in the previous section for considering the temperature effect in the extended fine structure. Thus, the vibrational information can be extracted from the temperature-dependent ARPEFS data based on the known structural parameters from the previous studies.[9-10]

As we have discussed in Sec. 4.2, the directional- and layer-dependent Debye temperature $\theta_D(\alpha, l_{3a})$ was used to calculate the mean-square displacement (MSD) and the mean-square relative displacement (MSRD) in the modified ARPEFS Debye model, where each layer is characterized by three directional Debye temperatures. In the simulation, the ratio of these Debye temperatures is proposed to reduce the number of free parameters. We also relate surface- and bulk- Debye temperatures by allowing the surface mean-square displacements to decay exponentially to the bulk values in three or four layers. Furthermore, the adsorbate directional Debye temperatures can be estimated based on the substrate surface- Debye temperatures adjusted for the difference in masses. However, these estimates of Debye-related parameters are only the initial guesses for the later simulations. Initially, we set copper and nickel bulk Debye temperatures as 343 K and 390 K, respectively, while their surface Debye temperatures were taken as 243 K and 276 K. The Debye temperatures were estimated to be 325 K for the Cl adsorbate on the copper surface, and 355 K for Cl on the nickel surface.

In the previous structural analyses on both the c(2×2) Cl/Cu(001) and $\sqrt{3}\times\sqrt{3}$ R30° Cl/Ni(111) systems,[9-10] the optimum structural parameters were obtained when a minimum R-factor, measuring the goodness of the fits between the theoretical and experimental $\chi(k)$ curves, was reached. Although some of the nonstructural parameters, including Debye temperatures, were also varied along with the structural parameters, it is difficult to extract accurate nonstructural parameters from the analysis because the theory is much more sensitive to the structural parameters. In the previous studies[9-10], we also found that the Debye-related parameters were not strongly correlated with the structural parameters although their reasonable estimates improved the fits between the theory and the experiment. From Eq. (15), we can see that the nonstructural parameters, mean free path and Debye temperature, mainly modulate the oscillatory amplitude of the extended

fine structure $\chi(k)$, while the oscillatory frequency is mostly determined by the structural parameters and phase shifts. Thus, the simulation method emphasizing the oscillatory amplitudes of the extended fine structure may increase the sensitivity to the Debye temperatures. There are two forms of experimental data: $\chi(k)$ curves and Fourier spectra. In comparison of a $\chi$ (k) curve with its Fourier spectrum, we found that varying structural parameters in a small range leads to a larger shift in the $\chi$ (k) curve than in the Fourier peak position, and the Fourier peak intensity is greatly dependent on the choices of Debye-related parameters when other structural parameters are close to their optimum values. Since the optimum structural parameters are known from the previous studies[9-10], simulating the experimental data, including Fourier spectra, can increase the accuracy of the Debye parameters. It would be ideal to fit a single Fourier peak at a time with few parameters. Unfortunately, we have to use many parameters to fit the single Fourier peak because of multiple scattering and many scatterers involved in the single peak. Moreover, different combinations of three directional Debye temperatures for a single pair of scatterers can give the similar value of MSRD with equally good fits. Thus, the directional Debye temperatures may not be uniquely defined if we only fit the single Fourier peak mostly due to the single-pair scattering. Therefore, we chose to fit the whole Fourier spectrum in simulations. By simulating both the $\chi$ (k) curve and its Fourier spectrum simultaneously for a given geometry, we can obtain the best fits between theory and experiment in both momentum (k) and real (R) spaces with increased accuracy for the fitting parameters.

We made comparisons of theory with experiment for all data sets by using the same path-length-difference cutoffs as in previous studies.[9-10] In the present study, an automatic routine described previously[9] was used to search many parameters at a time. To avoid changing too many parameters at a time, we first optimized the Debye-related

parameters while other parameters were kept in their optimum values obtained previously. These parameters are: the crystal bulk- Debye temperature, the crystal surface- Debye temperature in the direction perpendicular to the surface, the ratio of the crystal surface-Debye temperature in the parallel direction to that in the perpendicular direction, the exponential decay length, and the Debye temperatures of Cl, in the parallel and perpendicular directions.

First, we simulated the $\chi(k)$ curve and its Fourier spectrum simultaneously for a given geometry for all data sets. The optimum parameters were obtained when the sum of two R factors, calculated from the $\chi(k)$ curve and the Fourier spectrum, respectively, reached the minimum. The R factors were calculated over the k range 5.0 - 11.0 $Å^{-1}$. In addition to optimizing the above Debye-related parameters, we also varied the structural and nonstructural parameters at the same time to avoid any correlations between the Debye-related parameters and other parameters. The structural parameters obtained in this way agree with the results obtained in the previous studies within their error limits, further indicating no strong correlations between the Debye-related parameters and other parameters. However, the Debye-related parameters obtained from the normal emission data at two different temperatures have better consistency than those from the offnormal data. As we have discussed previously, the directional Debye temperatures might not be uniquely defined for the offnormal data because its Fourier spectrum is dominated by one strong peak which mainly comes from the one backscatterer. Second, we simulate both $\chi(k)$ curves at two different emission geometries simultaneously for a given temperature with one set of Debye-related parameters, using the ARPEFS directional sensitivity. The results for the Debye-related parameters agree with those obtained from the normal emission data in the first method. Although the results obtained from the above two methods are not as consistent for the offnormal emission data, both methods offered

equally good fits, further demonstrating that the three directional Debye temperatures are not well defined for the offnormal data. Finally, we simulate both $\chi(k)$ curves at different temperatures for the normal emission data with the same sets of Debye-related parameters, using the temperature dependence of the $\chi(k)$ function. The results are consistent with those obtained from the above two methods. In summary, all three methods provided fairly consistent results, especially for the relative magnitudes of adsorbate- Debye temperatures in the parallel direction with respect to that in the perpendicular direction. Fitting two experimental curves simultaneously with less varying parameters induces statistical errors because of the increased number of degrees of freedom. The results for the crystal bulk- and surface- Debye temperatures and the exponential decay length were found to be close to the estimated values. The ratio of the crystal surface- Debye temperature in the parallel to that in the perpendicular direction was 1-1.3. However, we can't determine the anisotropy of the substrate surface- Debye temperatures accurately. Using a simple force-field model, we found that for both the c(2×2)Cl/Cu(001) and $\sqrt{3}\times\sqrt{3}$ R30° Cl/Ni(111) systems, each of the first-layer substrate atoms not only no longer vibrates isotropically in the x and y directions but also no longer has the same site symmetry orientaton.[21] Figure 6 gives an example showing that half of the atoms in the first substrate layer vibrate differently from another half in the c(2×2) adsorbate structure. In our model, we assume all atoms in the same layer having the same set of three directional Debye temperatures. Thus, the substrate directional Debye temperatures obtained from the simulations are actually the averaged results of all the atoms in the same layer.

The mean-square displacements (MSD) for the adsorbate atoms are shown in Table I. These values were calculated from Eq. (12) using the adsorbate directional Debye temperatures obtained from the above analysis. The adsorbate MSD for the

c(2×2)Cl/Cu(001) system is $0.9 \times 10^{-2}$ (Å$^2$) in the parallel direction, and $4.0 \times 10^{-3}$ (Å$^2$) in the perpendicular direction, while for the $\sqrt{3}\times\sqrt{3}$ R30° Cl/Ni(111) system, the MSD in the parallel direction is $2.4 \times 10^{-2}$ (Å$^2$), and $4.9 \times 10^{-3}$ (Å$^2$) in the perpendicular direction. From Table I, we can see that the MSD values in the parallel direction are larger than those in the perpendicular direction for both systems. However, the ratio of the MSD between the parallel and the perpendicular directions for the $\sqrt{3}\times\sqrt{3}$ R30° Cl/Ni(111) system is larger than that for the c(2×2)Cl/Cu(001) system.

| | c(2×2)Cl/Cu(001) | $\sqrt{3}\times\sqrt{3}$ R30°Cl/Ni(111) |
|---|---|---|
| Adsorption site | fourfold | threefold |
| $<(u_{\parallel}^{Cl})^2>$ | $0.9 \times 10^{-2}$ (Å$^2$) | $2.4 \times 10^{-2}$ (Å$^2$) |
| $<(u_{\perp}^{Cl})^2>$ | $4.0 \times 10^{-3}$ (Å$^2$) | $4.9 \times 10^{-3}$ (Å$^2$) |
| $\frac{<(u_{\parallel}^{Cl})^2>}{<(u_{\perp}^{Cl})^2>}$ | 2.3 | 4.9 |

Table I. The adsorbate mean-square displacements (MSD) for both the c(2×2)Cl/Cu(001) and the $\sqrt{3}\times\sqrt{3}$ R30° Cl/Ni(111) systems. These values were calculated from Eq. (12) using the adsorbate directional Debye temperatures obtained from the simulations of the experimental data.

## 4.4 Prediction of Vibrational Anisotropy

Recent studies[3-6] have shown the existence of different types of surface-atom vibrational anisotropy. Sette et al.[5], in a study of c(2×2)Cl/Cu(001), proposed that the origin of an adsorbate parallel mean-square displacement ($< ( \mathbf{u}_{\parallel}^{a} )^2 >$) larger than the perpendicular one ($< ( \mathbf{u}_{\perp}^{a} )^2 >$) is connected with the charge transfer from the substrate to the adsorbate atoms. They expected that such charge transfer induces a stiffening of the effective perpendicular adsorbate-substrate force constant, a softening of the in-plane surface vibrational modes due to the weakening of the metal-metal surface bonds, and an expansion in the topmost substrate interlayer spacing. However, this simple picture does not fit the reversed case c(2×2)O/Ni(001), where the adsorbate $< ( \mathbf{u}_{\parallel}^{a} )^2 >$ is smaller than the $< ( \mathbf{u}_{\perp}^{a} )^2 >$. Our ARPEFS studies have showed the adsorbate $< ( \mathbf{u}_{\parallel}^{a} )^2 >$ is larger than the $< ( \mathbf{u}_{\perp}^{a} )^2 >$ for both the $\sqrt{3}\times\sqrt{3}$ R30° Cl/Ni(111) and c(2×2)Cl/Cu(001) systems, in agreement with the SEXAFS study by Sette et al.[5] However, using their picture, we can't explain the larger ratio of the MSD between the parallel and the perpendicular directions for the $\sqrt{3}\times\sqrt{3}$ R30° Cl/Ni(111) system than that for the c(2×2)Cl/Cu(001) system, and the contraction of the topmost substrate interlayer spacing in the $\sqrt{3}\times\sqrt{3}$ R30° Cl/Ni(111) system. It therefore seems difficult to predict the surface-atom vibrational anisotropy with a universal model. Recently, Yang et al.[8] presented lattice-dynamical calculations of the mean-square displacements of the adsorbate and first-layer substrate atoms for c(2×2) S and O overlayers on Ni(100). They found that for S atoms the mean-square displacement in the plane parallel to the surface is larger than that along the surface normal, while the opposite case is for the O atoms, in agreement with SEXAFS experiments. However, the lattice-dynamical calculation requires phonon spectral

densities derived from EELS experiments. Because of the limited number of systems studied by EELS and a large amount of computations required for the calculation, only a few systems have been studied by using this method. Therefore, it is important to have a simple and straightforward way to predict the vibrational anisotropy. In this section, a model for predicting the vibrational anisotropy is presented and applied to several available systems for testing its validity.

We first consider the fourfold adsorption geometry such as the c(2×2) or p(2×2) overlayers on the fcc (100) surfaces. The c(2×2)Cl/Cu(001) system is an example of this. A picture of a 5-atom cluster with one adsorbate and four nearest substrate atoms is shown in Fig. 7, where parameters d(Å) and b(Å) represent the perpendicular distance from the adsorbate to the first substrate layer and the interatomic distance between the adsorbate and the nearest substrate atom projected on the direction parallel to the surface, respectively. In the model prediction, we assume that the interaction between the adsorbate and each of the four stationary substrate atoms is a pair-wise interaction which can be described by a Lennard-Jones (LJ) potential,

$$\Phi(R) = 4\,\varepsilon\,[\,(\sigma / R)^{12} - (\sigma / R)^{6}\,]. \qquad (17)$$

Here R is the interatomic distance between the adsorbate and the substrate atoms, $\varepsilon$ is the potential parameter, and $\sigma$ is related with the equilibrium interatomic distance Re through the relation

$$Re = 2^{1/6}\,\sigma = (b + d)^{1/2}\,. \qquad (18)$$

The LJ potential used in this study is for its simplicity. There is only one potential-dependent parameter $\varepsilon$ in its form shown in Eq. (17). In Cartesian coordinates, we choose **X** and **Y** for two orthogonal directions in a plane parallel to the surface, and **Z** for the direction perpendicular to the surface. The displacement for the adsorbate atom in a given direction (**X**, **Y** or **Z**) is represented by X, Y, or Z, respectively. Since the force constant

for the adsorbate atom in a given direction can be calculated by taking the second derivative of the projected potential on that direction at the equilibrium position $\alpha = 0$, with $\alpha = X$, Y, or Z, we obtain

$$K_X = \partial^2 \sum_j \phi_j / \partial X^2 \Big|_{\alpha=0} = 144\, \varepsilon\, b^2 / (b^2 + d^2)^2, \tag{19}$$

$$K_Y = \partial^2 \sum_j \phi_j / \partial Y^2 \Big|_{\alpha=0} = 144\, \varepsilon\, b^2 / (b^2 + d^2)^2, \tag{20}$$

$$\text{and } K_Z = \partial^2 \sum_j \phi_j / \partial Z^2 \Big|_{\alpha=0} = 288\, \varepsilon\, d^2 / (b^2 + d^2)^2. \tag{21}$$

Here the summation is over all the substrate atoms (j = 1,4). Therefore, the force constants in the directions parallel and perpendicular to the surface can be written as

$$K_{\parallel}^{Cl} = 144\, \varepsilon\, b^2 / (b^2 + d^2)^2, \tag{22}$$

$$\text{and } K_{\perp}^{Cl} = 288\, \varepsilon\, d^2 / (b^2 + d^2)^2. \tag{23}$$

Similar procedures were applied to the threefold adsorption geometry (see Fig. 7). The $\sqrt{3}\times\sqrt{3}$ R30° Cl/Ni(111) system is an example of this. The force constant in the three orthogonal directions are

$$K_X = \partial^2 \sum_j \phi_j / \partial X^2 \Big|_{\alpha=0} = 108\, \varepsilon\, b^2 / (b^2 + d^2)^2, \tag{24}$$

$$K_Y = \partial^2 \sum_j \phi_j / \partial Y^2 \Big|_{\alpha=0} = 108\, \varepsilon\, b^2 / (b^2 + d^2)^2, \tag{25}$$

$$\text{and } K_Z = \partial^2 \sum_j \phi_j / \partial Z^2 \Big|_{\alpha=0} = 216\, \varepsilon\, d^2 / (b^2 + d^2)^2. \tag{26}$$

Thus, we obtain

$$K_{\parallel}^{Cl} = 108\, \varepsilon\, b^2 / (b^2 + d^2)^2, \tag{27}$$

$$\text{and } K_{\perp}^{Cl} = 216\, \varepsilon\, d^2 / (b^2 + d^2)^2. \tag{28}$$

From the above equations we can see that for both the fourfold and threefold adsorption geometries, force constants in a plane parallel to the surface are isotropic ($K_X = K_Y$) and the perpendicular force constant ($K_Z$) has a different form from the parallel one. We also notice that the force constants derived here are only dependent on the potential parameter $\varepsilon$ and the structural parameters b and d.

| | Structural parameter | | MSD ratio | |
|---|---|---|---|---|
| | b (Å) | d (Å) | Model prediction | This work |
| Cl/Cu(001) | 1.807 | 1.61 | 1.6 | 2.2 |
| Cl/Ni(111) | 1.437 | 1.84 | 3.3 | 4.9 |

Table II. Comparison of mean-square-displacement ratios (MSD ratio) between the parallel and the perpendicular directions derived from the model prediction with those obtained from this work by simulating the ARPEFS experimental data.

Within the harmonic approximation, the mean-square displacement (MSD) $< ( \mathbf{u} )^2 >$ is inversely proportional to the force constant K. Thus, the MSD ratio between the parallel and the perpendicular directions can be represented as

$$\frac{(< ( \mathbf{u}_{\parallel}^{Cl} )^2 >)}{(< ( \mathbf{u}_{\perp}^{Cl} )^2 >)} \propto \frac{K_{\perp}^{Cl}}{K_{\parallel}^{Cl}} = \frac{2\,d^2}{b^2}. \qquad (29)$$

Surprisingly, the MSD ratio is potential and adsorption-site independent. Instead of using Lennard-Jones potential, Eq. (29) can also be derived by using other potentials such as harmonic or coulombic potentials. Both the threefold and fourfold adsorption sites give the same simple form, depending only on the structural parameters b and d. Thus, Eq. (29) allows us to predict the vibrational anisotropy for the adsorbate atom from the structural information, linking the geometric structures and the dynamic phenomenon.

| $\frac{\langle (u_{\parallel}^{A})^2 \rangle}{\langle (u_{\perp}^{A})^2 \rangle}$ | c(2×2) O/Ni(100)[7,8] | c(2×2) S/Ni(100)[6,8,22] | p(2×2) S/Cu(001)[23] | p(1×1) Co/Cu(111)[3,a] |
|---|---|---|---|---|
| Prediction | $< 1$ | $> 1$ | $\approx 1$ | $< 1$ |
| Experiment | $< 1$ | $> 1$ | $\approx 1$ | $< 1$ |

a) as a case of d = 0.

Table III. The adsorbate mean-square-displacement ratios (MSD ratio) obtained from the model prediction and experiments, respectively. The references for the structural parameters b and d used in the model prediction, and the experimental results of vibrational anisotropy are listed.

Now we apply Eq. (29) to both the c(2×2)Cl/Cu(001) and $\sqrt{3}\times\sqrt{3}$ R30° Cl/Ni(111) systems. Since the structural parameters b and d for both systems are known from the previous ARPEFS studies, we can calculate the MSD ratio by using Eq. (29).

Table II shows the comparison of the MSD ratios derived from the model prediction with those obtained from this work by simulating the ARPEFS experimental data. From Table II, we can see that the model prediction and this work offer consistent results for both systems. The mean-square displacements in the parallel direction are larger than those in the perpendicular direction, and the $\sqrt{3}\times\sqrt{3}$ R30° Cl/Ni(111) has a larger anisotropy (larger MSD ratio) than the c(2×2)Cl/Cu(001) system. Although the absolute MSD ratios derived from the model prediction are smaller than those obtained from this work, this model gives good estimates of relative magnitudes of vibrational anisotropy from the structural information. More importantly, it provides a simple and straightforward physical picture for us to understand the vibrational anisotropy. Equation (29) shows that the larger d and the smaller b give the larger ratio of the MSD between the parallel and the perpendicular directions. When an adsorbate atom sits farther above the smoother surface (larger d and smaller b), it is understandable that the adsorbate atom can move more easily in the parallel direction than in the perpendicular direction. This may be the reason for a larger anisotropy (larger MSD ratio) in the $\sqrt{3}\times\sqrt{3}$ R30° Cl/Ni(111) system than in the c(2×2)Cl/Cu(001) system ( see Table II). Thus, whether or not the adsorbate atom has a larger parallel motion than the perpendicular one depends on the competition of the two factors d and b through the relation given in Eq. (29). In an extreme case (d = 0), the model always predicts the larger MSD in the perpendicular direction than that in the parallel direction, in agreement with the conventional view for the clean metal surfaces. We can imagine the case of d = 0 as either a clean metal surface or a full monolayer (100% coverage) adsorbate system. For both clean metal surfaces and full monolayer adsorbate systems, atoms in the topmost layer can move much easier in the perpendicular direction than the parallel direction because of the large lateral interaction between the adsorbate atoms and more degrees of freedom for the atomic motion in the perpendicular direction.

This is the case for the epitaxial (1×1)Co/Cu(111) system[3] (simulating a fcc densely packed clean metal surface), where the vibrational amplitude in the perpendicular direction was found to be larger than in those parallel. To further test the validity of this model, we also applied this model to other systems for which both structural and vibrational information are known. Table III lists the MSD ratios obtained from both the experiments and the model prediction (the MSD ratio larger than 1 means the larger parallel MSD than the perpendicular). Here we only give the directions of the adsorbate vibrational anisotropy because the absolute values of the MSD are unknown for the most adsorbate systems. From Table III, we can see that our model prediction is in excellent agreement with experiments, thus further showing the validity of this model.

## 4.5 Discussion and Conclusions

Both ARPEFS and SEXAFS are less direct for studying surface-atom vibrations than the techniques such as He-atom scattering and EELS. However, they can provide information about surface-atom vibrational anisotropy directly from experiments in a simple and straightforward way.

There are several sources of errors in both ARPEFS and SEXAFS. Errors using the modified ARPEFS Debye model may be negligible because we have shown that this model reasonably described the vibrational attenuation in the scattering process. However, the analysis methods themselves in both SEXAFS and ARPEFS may bring some errors. In ARPEFS, they might come from the simulation of experimental data because the oscillatory function $\chi(k)$ has lower sensitivity to the Debye related parameters than to the structural parameters, while in SEXAFS, errors might result from the back-Fourier transformation or the nonlinearity due to the low-quality data or nonseparable shells.

Unlike SEXAFS, which provides the difference between MSRD values at two different temperatures by using the theory-independent ratio method, ARPEFS gives the MSRD and MSD values for surface atoms by simulating experimental data. Because the ARPEFS Debye model treats the substrate atoms in the same layer equally, we can only obtain the averaged MSD values for the first-layer substrate atoms for both $\sqrt{3}\times\sqrt{3}$ R30° Cl/Ni(111) and c(2×2)Cl/Cu(001) systems. Since the first-layer substrate atoms in both adsorbate systems no longer have the same site symmetry orientation, treating them equally may cause errors in the MSD values for the adsorbate atoms due to the correlated motion between the adsorbate and substrate atoms. However, these errors might be small because the substrate atom has larger atomic mass than the adsorbate atom in both systems. Both ARPEFS and SEXAFS techniques are complementary to He-scattering and EELS for studying the surface-atom vibrational information. Since the goal of this study is to obtain information about surface-atom vibrational anisotropy and predict this anisotropy with a simple physical model, our main concern is the MSD ratios or the relative magnitudes of the MSD in the parallel to the perpendicular directions, but not the absolute MSD. Thus, even if there are small errors associated with the absolute MSD values, we can still get the accurate information about the vibrational anisotropy.

Although the model we proposed is based on the force-constant ideas with symmetry concept, it can successfully predict the adsorbate-atom vibrational anisotropy. We have tested the electronegative adsorbate systems such as S, O, or N on the simple transition-metal surfaces with small reconstruction and less than 50% monolayer coverage. The full lattice-dynamic calculations by Yang et al.[8] based on the phonon dispersion spectra offered more detailed information about surface-atom vibrations. However, our simple model prediction agrees with their study on the vibrational anisotropy and provides

a similar explanation for the opposite anisotropy between the O/Ni(001) and S/Ni(001) systems (see section 4.4).

In conclusion, this chapter presents a study of surface-atom vibrations for both the $\sqrt{3}\times\sqrt{3}$ R30° Cl/Ni(111) and c(2×2)Cl/Cu(001) systems using temperature-dependent ARPEFS. We found that the mean-square displacements in the direction parallel to the surface are larger than those perpendicular ones for both systems. However, the relative magnitude of the vibrational anisotropy in the parallel direction to the perpendicular direction for the $\sqrt{3}\times\sqrt{3}$ R30° Cl/Ni(111) is larger than that for the c(2×2)Cl/Cu(001). Also, we proposed a model for predicting the adsorbate-atom vibrational anisotropy. This model was successfully applied to the $\sqrt{3}\times\sqrt{3}$ R30° Cl/Ni(111), the c(2×2)Cl/Cu(001), and other available systems. It indeed offers a simple and straightforward physical picture for understanding different types of vibrational anisotropy. For example, the c(2×2) overlayers of S and O on Ni(100) have the opposite vibrational anisotropy for S and O atoms.

# References


1. G. Brusdeylins, R.B. Doak, and J.P. Toennis, *Phys. Rev. Lett.* **44**, 1417 (1980).
2. H. Ibach and D.A. Mills, Electron Energy Loss Spectroscopy (Academic Press, London, 1982).
3. P. Roubin, D. Chandesris, G. Rossi, J. Lecante, M.C. Desjonqueres, and G. Treglia, *Phys. Rev. Lett.* **56**, 1272 (1986).
4. M. Bader, A. Puschmann, C. Ocal, and J. Haase, *Phys. Rev. Lett.* **57**, 3273 (1986).
5. F. Sette, C.T. Chen, J.E. Rowe, and P.H. Citrin, *Phys. Rev. Lett.* **59**, 311 (1987).
6. F. Sette, T. Hashizume, F. Comin, A.A. MacDowell, and P.H. Citrin, *Phys. Rev. Lett.* **61**, 1384 (1988).
7. L. Wenzel, J. Stohr, D. Arvanitis, and K. Baberschke, *Phys. Rev. Lett.* **60**, 2327 (1988).
8. L. Yang, T.S. Rahman, and D.L. Mills, *Phys. Rev.* **B 42**, 2864 (1990).
9. L.Q. Wang, A.E. Schach von Wittenau, Z.G. Ji, L.S. Wang, Z.Q. Huang, and D.A. Shirley, *Phys. Rev.* **B**, July, 1991, in press.
10. L.Q. Wang, Z. Hussain, Z.Q. Huang, A.E. Schach von Wittenau, and D.A. Shirley, Submitted to *Phys. Rev.* **B**, April, 1991.
11. V.V. Schmit, *Bull. Acad. Sci. USSR Phys. Ser.* **25**, 988; **27**, 392 (1961).
12. G. Beni and P.M. Platzman, *Phys. Rev.* **B 13**, 5170 (1976).
13. A.A. Maradudin, E. W. Montroll, G.H. Weiss, and I.P. Ipatova, Theory of Lattice Dynamics in the Harmonic Approximation (Academic Press, New York, 1983).
14. E. Sevillano, H. Meuth, and J.J. Rehr, *Phys. Rev.* **B 20**, 4908 (1979).
15. W. Bohmer and P. Rabe, *J. Phys.* **C 12**, 2465 (1979); R.B. Greegor and F. W. Lytle, *Phys. Rev.* **B 20**, 4902 (1979); G.S. Knapp, H.K. Pan, and J.M. Tranquada,

ibid. **32**, 2006 (1985); V.A. Biebesheimer, E.C. Marques, D.R. Sandstrom, F.W. Lytle, and R.B. Greegor, *J. Chem. Phys.* **81**, 2599 (1984).

16. J.J. Barton, S.W. Robey, and D.A. Shirley, *Phys. Rev.* **B 34**, 778 (1986).
17. R.E. Allen and F.W. DE Wette, *Phys. Rev.* **188**, 1320 (1969).
18. R.M. Housley and F. Hess, *Phys. Rev.* **146**, 517 (1966).
19. Y. Morino, K. Kuchitsu, A. Takahashi, and K. Maeda, *J. Chem. Phys.* **21**, 1927 (1953).
20. J.J. Barton, C.C. Bahr, Z. Hussain, S.W. Robey, J.G. Tobin, L.E. Klebanoff, and D.A. Shirley, *Phys. Rev. Lett.* **51**, 272 (1983).
21. D. Chandesris and G. Rossi, *Phys. Rev. Lett.* **60**, 2097 (1988).
22. J.J Barton, C.C. Bahr, S.W. Robey, Z. Hussain, E. Umbach and D.A. Shirley, *Phys. Rev.* **B34**, 3807 (1986).
23. A.E. Schach von Wittenau, L.Q. wang, Z. Hussain, Z.Q. Huang, Z.G. Ji, and D.A. Shirley, in preparation.

# Figure Captions

FIG. 1. Schematic illustration of the equilibrium and instantaneous positions of the emitting atom (o) and the scattering atom (a).

FIG. 2. Definition of the vectors used in the scattering process. Vectors $\mathbf{a}_0$ and $\mathbf{R}$ represent the equilibrium position of the scattering atom (a) and the direction to the electron detector, respectively. The electric vector is labelled by $\hat{\boldsymbol{\varepsilon}}$.

FIG. 3. Illustration of the ratio method for evaluating the difference of the relative mean-square displacements between two temperature. (a) The $\chi$ curves calculated from a 5-atom (one emitting and four scattering atoms) linear chain using a single-scattering model. The solid curve is $\chi(k)$ at 110 K, and the dashed curve is $\chi(k)$ at 300 K. (b) Fourier transforms of the above two $\chi(k)$ curves. The four well-separated peaks corresponds to the four scattering atoms amplitudes at 110 and 300 K as a function of $k^2$ for the first peak.

FIG. 4. Application of the ratio method to the ARPEFS experimental data. (a) The [110] experimental $\chi(k)$ curves for the $\sqrt{3}\times\sqrt{3}$ R30° Cl/Ni(111) at two different temperatures. The solid curve is $\chi(k)$ at 120 K, and the dashed curve is $\chi(k)$ at 300 K. (b) Fourier transforms of the above two $\chi(k)$ curves. (c) Inverse Fourier transform of the strong peak at ~ 4.6 Å. (e) Logarithmic ratio of the amplitudes at 120 and 300 K as a function of $k^2$.

FIG. 5 Comparison of the single-pair scattering calculation to the full multiple-scattering calculation for the $\sqrt{3}\times\sqrt{3}$ R30° Cl/Ni(111) along the [110] emission direction at 120 K. The solid curve is the inverse Fourier transform of the peak at ~ 4.6 Å obtained from the full multiple scattering calculation

including the first and the second substrate layers, while the dashed curve is a $\chi(k)$ curve calculated with a single-pair scattering model.

FIG. 6. Top view of the c(2×2) adsorbate on the fcc (001) surface. The larger circles represent the first-layer substrate atoms. The bold vectors illustrate the substrate-atom in-plane vibrations. The substrate atom in position A has a larger vibrational amplitudes along the **Y** direction than that along the **X** direction, while the opposite for the substrate atom in position B.

FIG. 7. Small cluster models for describing the fourfold and threefold adsorption geometries. (a) A 5-atom (one adsorbate and four nearest-neighbor atoms) cluster for the fourfold adsorption geometry. (b) Top view of (a). (d) A 4-atom cluster for the threefold adsorption geometry. (d) Top view of (c).

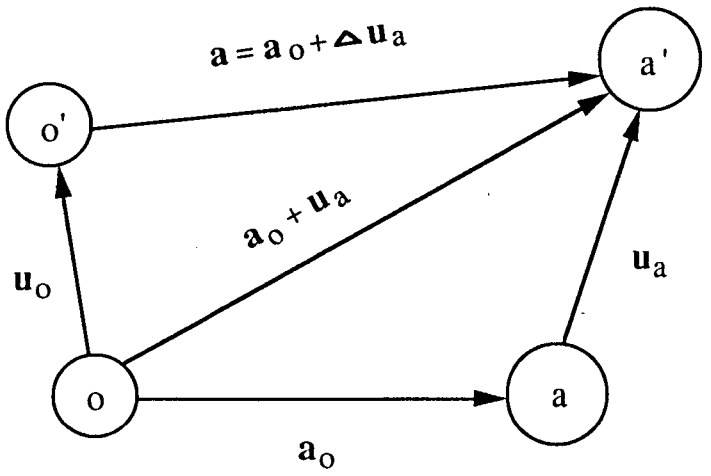


Figure 1

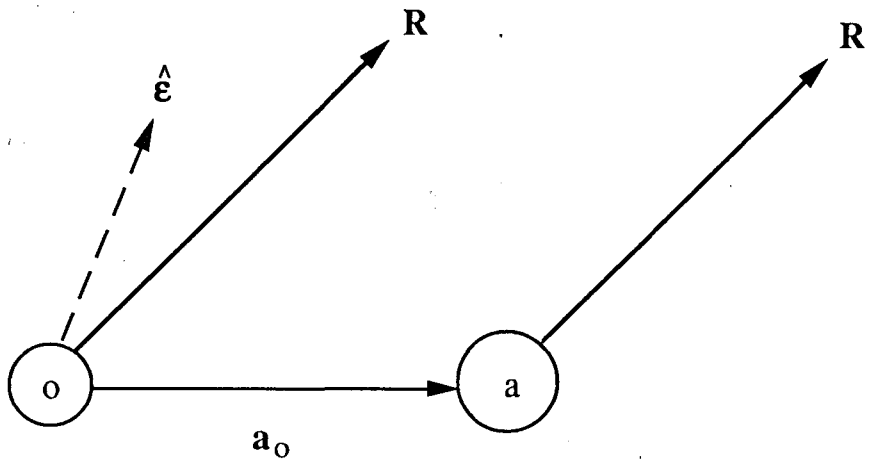


Figure 2

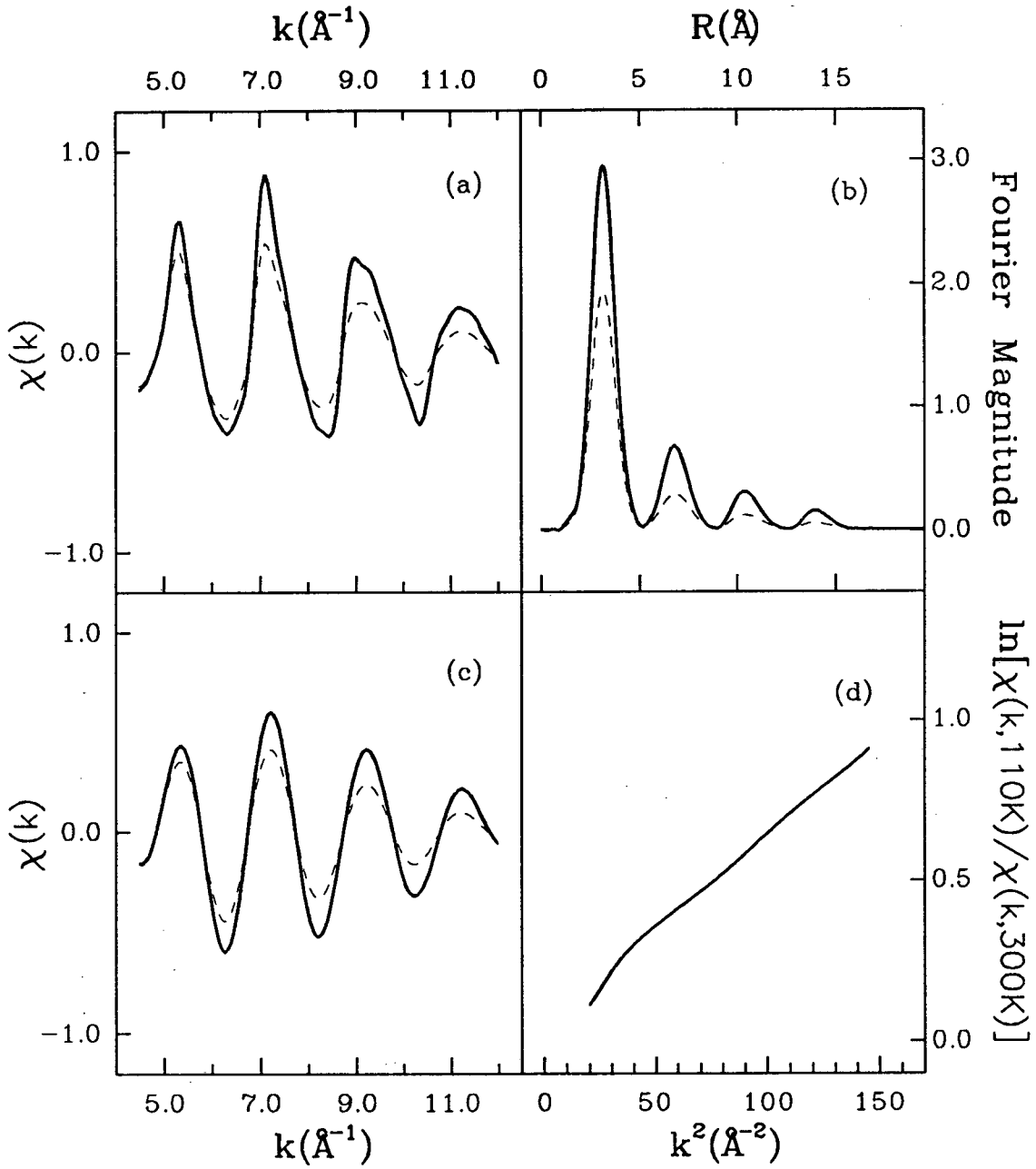
k(Å$^{-1}$)
R(Å)
5.0
7.0
9.0
11.0
0
5
10
15
1.0
0.0
−1.0
χ(k)
(a)
(b)
3.0
2.0
1.0
0.0
Fourier Magnitude
(c)
(d)
1.0
0.5
0.0
ln[χ(k,110K)/χ(k,300K)]
50
100
150
k$^2$(Å$^{-2}$)

Figure 3

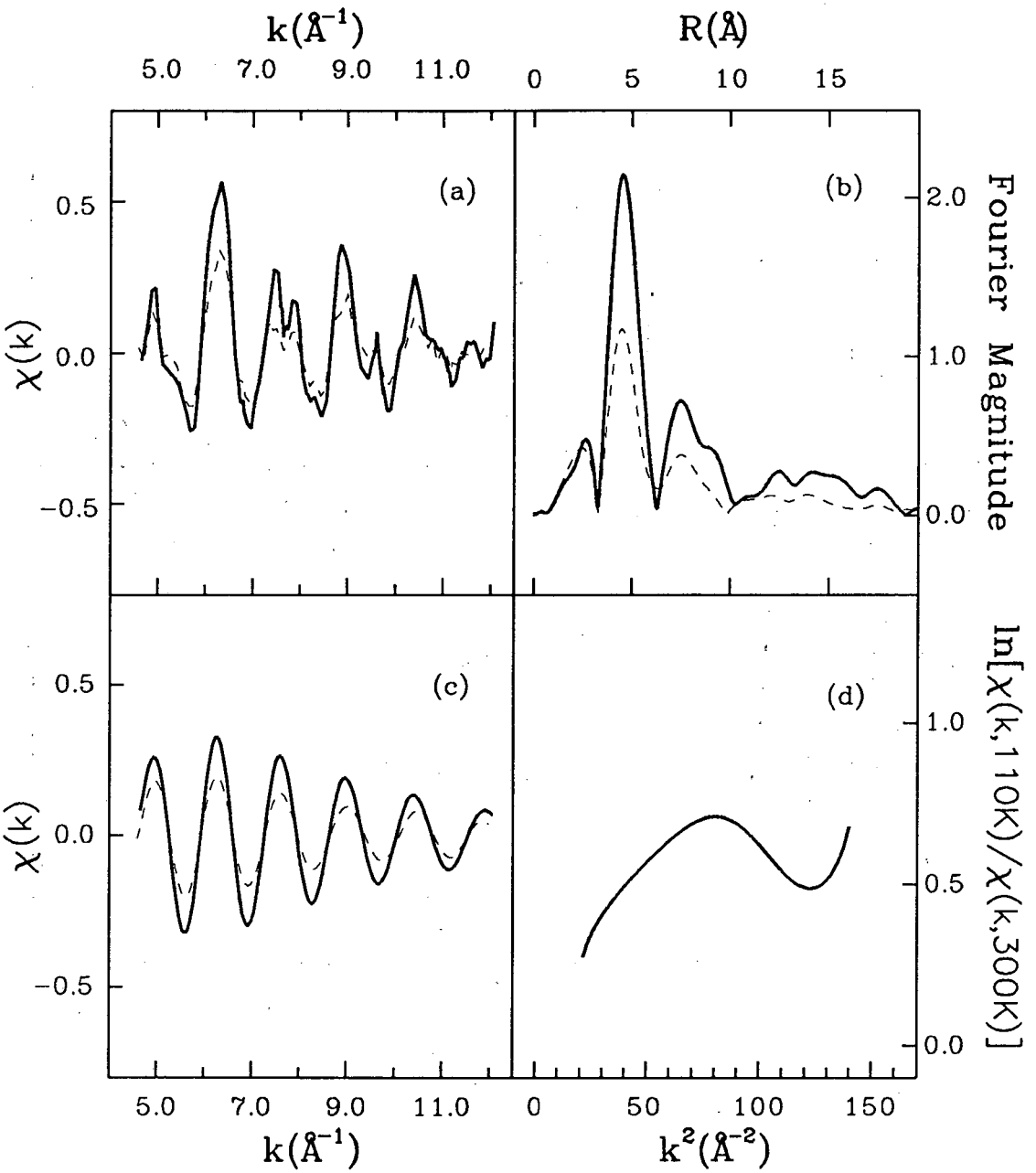
k(Å⁻¹)
5.0
7.0
9.0
11.0
R(Å)
0
5
10
15
(a)
(b)
(c)
(d)
χ(k)
0.5
0.0
−0.5
2.0
1.0
0.0
Fourier Magnitude
ln[χ(k,110K)/χ(k,300K)]
0
50
100
150
k²(Å⁻²)

Figure 4.

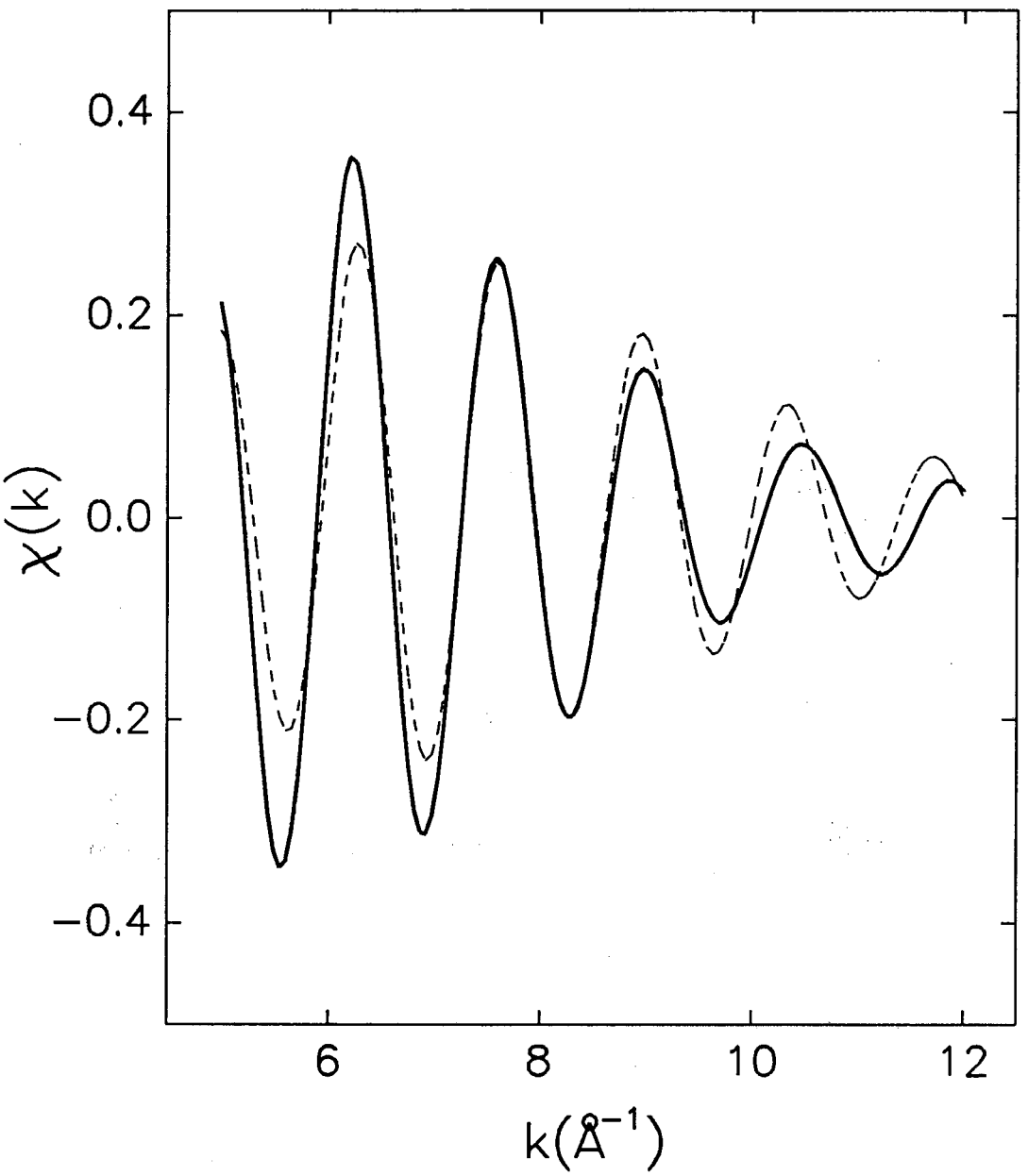


Figure 5

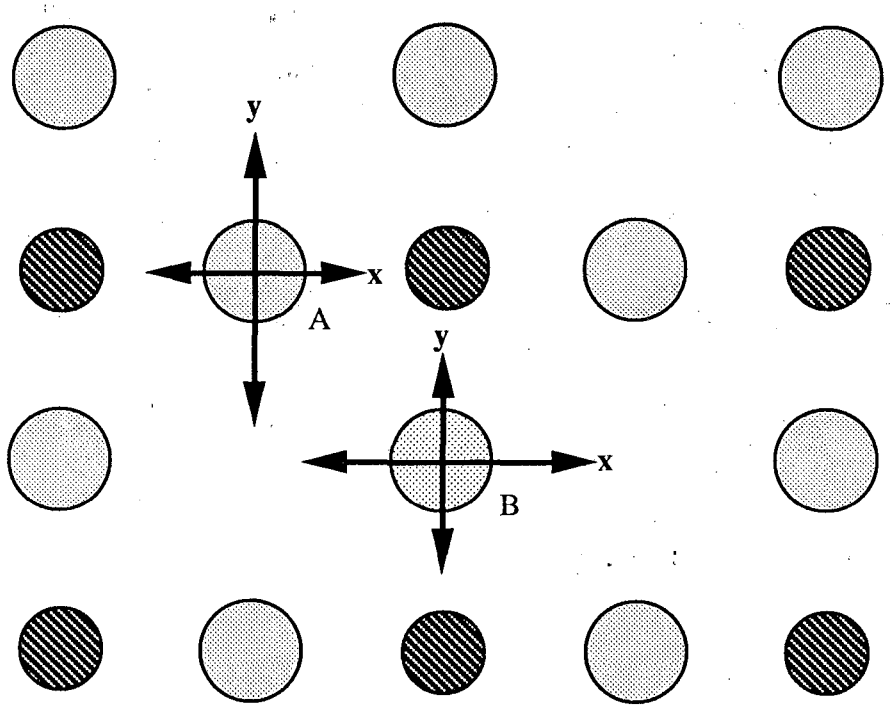


Figure 6

fourfold adsorption:

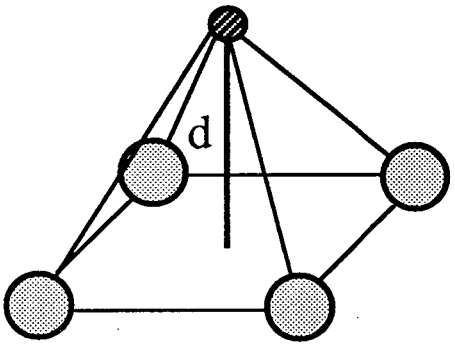


(a)

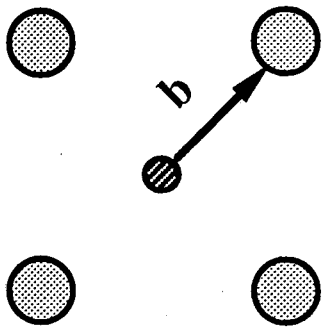


(b)

threefold adsorption:

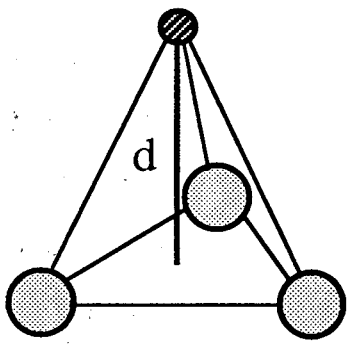


(c)

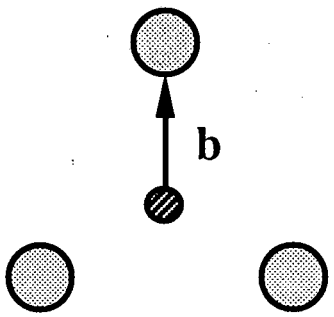


(d)

Figure 7

# Chapter 5

# Conclusions

A detailed study of the c(2×2)Cl/Cu(001) adsorption-geometry and substrate-surface relaxation using low-temperature ARPEFS was presented in chapter 2. Electrons were detected along two emission directions, [001] and [011], and at two temperatures, 110 K and 300 K. The Cl atoms were found to adsorb in the four-fold hollow site, 1.604 Å above the first copper layer, with a Cl-Cu bond length of 2.416 Å. The c(2×2)Cl-covered first copper layer showed no relaxation with respect to the bulk position. However, there is a 2% expansion of the separation between the first copper layer and the second atopped-site copper layer, and a small corrugation of the second copper layer where the atopped-site copper atoms are further away from the adsorbate Cl atom. The distances from the Cl atoms to the third and fourth copper layers were found to be 5.222 Å and 7.023 Å, respectively, indicating that atoms in the third and fourth copper layers remain in their bulk positions.

The major contribution of this chapter is the demonstration of the ability of low-temperature ARPEFS to determine both the accurate surface and the near-surface structure, including the deeper substrate layers. Cooling the lattice effectively extends the range of ARPEFS to the fourth copper layer, thereby firmly referencing atomic positions in the

surface and near surface layers to the bulk crystal lattice. This helps to understand the adsorbate-induced surface relaxation.

Another important aspect of this chapter is that we developed a method for estimating statistical errors or random errors in ARPEFS data analysis. Instead of quoting all errors as ca. ± 0.02 Å, we hope to have advanced a more quantitative way of estimating errors. The possible systematic errors involved in the data analysis were also discussed.

Chapter 3 presented a surface structural study of the $\sqrt{3}\times\sqrt{3}$ R30° Cl/Ni(111) system using low-temperature ARPEFS for further investigating adsorbate-induced substrate-surface relaxations. The experiments were performed along two emission directions, [111] and [110], and at two temperatures, 120 K and 300 K. The multiple-scattering spherical-wave analysis determined that the Cl atom adsorbs in the fcc three-fold hollow site, 1.837 Å above the first nickel layer, with a Cl-Ni bond length of 2.332 Å, and an approximate 5% contraction between the first and the second nickel layers.

A comparison of the results from chapters 2 and 3 reveals different kinds of adsorbate-induced substrate relaxations. An expansion of the topmost substrate interlayer spacing was found for the c(2×2)Cl/Cu(001) system, but a contraction for the $\sqrt{3}\times\sqrt{3}$ R30° Cl/Ni(111) system. However, the mechanism of contraction for the $\sqrt{3}\times\sqrt{3}$ R30° Cl/Ni(111) system is not clear. Thus, theoretical studies are desirable for a better understanding of the adsorbate-induced expansion or contraction.

Chapter 4 presented a study of the surface-atom vibrations for both the $\sqrt{3}\times\sqrt{3}$ R30° Cl/Ni(111) and c(2×2)Cl/Cu(001) systems using temperature-dependent ARPEFS. The adsorbate mean-square displacements in the parallel to the surface were found to be larger than in those perpendicular for both systems. However, the relative magnitude of the vibrational anisotropy in the parallel direction to the perpendicular direction for the $\sqrt{3}\times\sqrt{3}$ R30° Cl/Ni(111) is larger than that for the c(2×2)Cl/Cu(001). In chapter 4, we

also presented a model to predict the adsorbate-atom vibrational anisotropy from structures and to link the structural and dynamic information.

ARPEFS, LEED, and SEXAFS studies often give different structural results for the same adsorbate system. This difference is sometimes beyond the standard error of each technique. For example, studies on the p(2×2) S/Ni(111) system using several different techniques showed rather different results for the vertical distance of S to the first Ni layer S-Ni(1), ranging from 1.40 to 1.66 Å.[1-6] However, most ARPEFS studies agree better with LEED studies than with SEXAFS. The distances of adsorbate to the first substrate layer from SEXAFS studies on both p(2×2) S/Ni(111) and $\sqrt{3}\times\sqrt{3}$ R30° Cl/Ni(111) systems tend to be larger than the results obtained from LEED and ARPEFS studies. This suggests some sort of unknown systematic errors among these techniques. Thus, it is important to resolve those errors which cause the discrepancies among the three methods. The scattering phase shifts may be one of the possible errors. However, this error is negligible in EXAFS studies because EXAFS analyses can use experimental phase shifts. Since the exact phase shifts are unkown and there is no standard method to judge them, any calculations using theoretical phase shifts have unknown systematic errors. Therefore, further improvement on phase-shift calculations is needed to reduce systematic errors, which should resolve some discrepancies.

In chapters 2 and 3, we have shown the advantages of using low-temperature ARPEFS for studying the surface and the near-surface structures. Our experiments were performed at 110-120 K using liquid nitrogen cooling. However, with liquid helium cooling, temperatures can be as low as 10-20 K. At such temperatures, the low-temperature effect of ARPEFS is more prominent. Thus, future ARPEFS studies using liquid helium cooling are required for obtaining more accurate structural information for the deeper layers, further testing the depth sensitivity of ARPEFS. More importantly,

liquid helium cooling allows one to study physisorbed atomic or molecular adsorbate systems using low-temperature ARPEFS.

It would be ideal to take $\chi$ curves as a function of temperatures for temperature-dependent ARPEFS studies. However, it is impractical because of limited beam time and experimental difficulties. In chapter 4, a study of surface-atom vibrations was made using temperature-dependent ARPEFS at two different temperatures, 300K and ~ 110K. In the future, it would be interesting to perform experiments at temperatures higher than the room temperature or at the liquid helium temperature for further studying the temperature effect on surface-atom vibrations. More interestingly, for some adsorbate systems, one may observe phase transitions during temperature changing. It is challenging to study the phase transitions of such adsorbate systems. As we discussed in chapter 4, both ARPEFS and SEXAFS are less direct in studying surface-atom vibrations. The more detailed and quantitative surface-atom vibrational information can be obtained with combinations of other techniques such as He scattering[7] or EELS.[8]

Although an automatic routine for searching many parameters at a time speeded up our data analyses, a large amount of calculations using different initial guesses and bounds had to be taken to avoid local minima. For the systems with many variables, it is still a long process to obtain the optimum parameters. In comparison with SEXAFS, ARPEFS data analysis indeed takes much longer time. However, because of its depth and directional sensitivities, ARPEFS can provide some new structural information which SEXAFS can't. For example, ARPEFS can obtain the accurate structural information including the fourth substrate layer in a study of c(2×2)Cl/Cu(001) (Ref. 9) and distinguish two different kinds of three-fold adsorption sites for the $\sqrt{3}\times\sqrt{3}$ R30° Cl/Ni(111) (Ref. 10).

In general, ARPEFS is more precise in analyzing detailed structures such as small relaxations or reconstructions on and near surfaces than SEXAFS, and simpler than LEED in theoretical modelling, but more complicated in experimental details. In this thesis, we use the advantages of ARPEFS to obtain the accurate structural and near-structural information including deeper layers. A scientific approach using multiple techniques is required to understand more complicated systems.

# References


1. A.E. Schach von Wittenau, L.Q. Wang, Z.G. Ji, Z.Q. Huang, T. Shulman and D.A. Shirley ( in preparation).
2. T. Yokoyama, M. Funabashi, Y. Kitajima, T. Ohta and H. Kuroda, *Physica* **B 158**, 643 (1989)
3. Y.K. Wu and K.A.R. Mitchell, *Can. J. Chem.* **67**, 1975 (1989).
4. T. Fauster, H. Durr, and D. Hartwig, *Surf. Sci.* **178**, 657 (1986).
5. D. R. Warburton, P.L. Wincott, G. Thornton, F.M. Quinn, and D. Norman, *Surf. Sci.* **211/212**, 71 (1989).
6. J.E. Demuth, D.W. Jepsen, and P.M. Marcus, *Phys. Rev. Lett* **32**, 1182 (1974).
7. G. Brusdeylins, R.B. Doak, and J.P. Toennis, *Phys. Rev. Lett.* **44**, 1417 (1980).
8. H. Ibach and D.A. Mills, Electron Energy Loss Spectroscopy (Academic Press, London, 1982).
9. L.Q. Wang, A.E. Schach von Wittenau, Z.G. Ji, L.S. Wang, Z.Q. Huang, and D.A. Shirley, *Phys. Rev.* **B**, July, 1991, in press.
10. L.Q. Wang, Z. Hussain, Z.Q. Huang, A.E. Schach von Wittenau, and D.A. Shirley, Submitted to *Phys. Rev.* **B**, April, 1991.

# Acknowledgements

I would like to take this opportunity to acknowledge those people who have helped me during my graduate study.

First I would like to thank my graduate advisor Prof. David A. Shirley for his support and encouragement. I have learned a lot from his profound knowledge and great scientific attitude. I also would like to thank my collaborators, Zhengqing Huang, Alexis Schach, and Zahid Hussain. Without their collaboration, the round-clock ARPEFS measurements using Synchrotron Radiation would not have been possible. I am also thankful to Lou Terminello for teaching me how to start scattering calculations. I am grateful to Dr. Michel van Hove for some invaluable discussions. Thanks also go to Joe Katz for solving many of our electronic problems.

I wish to thank the entire Shirley group for their help and friendship. In particular, my thanks go to Jane Medhurst, my officemate for almost five years. I have always had pleasant times together with her and enjoyed talking with her on diverse topics ranging from "error analysis" or "shape resonance" to "new English vocabulary". I have also had nice conversations with Zhengqing Huang and Baohua Niu. Teri Kanefield deserves special thanks for reading some of my manuscripts.

Many friends have made my stay at Berkeley very enjoyable and pleasant. In particular, I wish to thank Phil Heimann most for his friendship and many helps. My one-year roommate Luoping has been a good company.

Finally, my deepest thanks go to my husband and colleague, Lai-Sheng, for his constant love, support, and encouragement. Without you, Lai-Sheng, this thesis would

have been impossible. I also wish to thank my family, especially my parents for their love and support throughout all these years.

This work was supported by the Director, Office of Energy Research, Office of Basic Energy Sciences, Chemical Sciences Division of the U.S Department of Energy under the Contract No. DE-AC03-76SF00098.

LAWRENCE BERKELEY LABORATORY
UNIVERSITY OF CALIFORNIA
INFORMATION RESOURCES DEPARTMENT
BERKELEY, CALIFORNIA 94720